Fall 2014

Solid amine-boranes as high performance hypergolic hybrid rocket fuels

Mark A. Pfeil
Purdue University

Recommended Citation

Pfeil, Mark A., "Solid amine-boranes as high performance hypergolic hybrid rocket fuels" (2014). *Open Access Dissertations*. 347.
https://docs.lib.purdue.edu/open_access_dissertations/347

Graduate School Form 30
(Updated 11/20/2014)

PURDUE UNIVERSITY
GRADUATE SCHOOL
Thesis/Dissertation Acceptance

This is to certify that the thesis/dissertation prepared

By Mark A Pfeil

Entitled
SOLID AMINE-BORANES AS HIGH PERFORMANCE HYPERGOLIC HYBRID ROCKET FUELS

For the degree of Doctor of Philosophy

Is approved by the final examining committee:

Stephen D Heister

Steven F Son

Sally P Bane

Timothee L Pourpoint

To the best of my knowledge and as understood by the student in the Thesis/Dissertation Agreement, Publication Delay, and Certification/Disclaimer (Graduate School Form 32), this thesis/dissertation adheres to the provisions of Purdue University's "Policy on Integrity in Research" and the use of copyrighted material.

Approved by Major Professor(s): Stephen D Heister

Approved by: Tom I-P Shih for Weinong Chen 12/08/2014

Head of the Department Graduate Program Date

SOLID AMINE-BORANES AS HIGH PERFORMANCE HYPERGOLIC HYBRID ROCKET FUELS

A Dissertation

Submitted to the Faculty

of

Purdue University

by

Mark A. Pfeil

In Partial Fulfillment of the

Requirements for the Degree

of

Doctor of Philosophy

December 2014

Purdue University

West Lafayette, Indiana

To my dear children.

ACKNOWLEDGEMENTS

I would first like to thank my advisors Professor Stephen Heister and Professor Steven Son. I am forever thankful for their willingness to take me on and spend time and effort to help me develop professionally. I very much enjoy the rocket/energetics field, and because of their efforts, I will be able to enjoy a long and fruitful career in this area. I am also appreciative for their friendship along the way.

I also want to thank all others who have spent time teaching me from other professors to fellow graduate students. Professor Timothée Pourpoint, Scott Meyer, Rob McGuire, Professor P. Veeraraghavan Ramachandran, and Bradley Templin were all very helpful in providing ideas and support for which I am very grateful. Brandon Terry deserves special thanks for all help performing tests and staying late into the night so I could perform research.

I would like to thank the Department of Defense for financial support through the Science Mathematics and Research Transformation (SMART) scholarship so that I could complete my studies. I am grateful for the mentorship of Darren Thompson and the support of the Propulsion and Energetics Functions within Aviation and Missile Research, Development, and Engineering Center in Huntsville, AL.

Finally, I would like to thank my family. My parents, for all the cheering and moral support. My dear wife, for the friendship, support, and companionship you have provided throughout this whole endeavor.

TABLE OF CONTENTS

Page

Page

LIST OF TABLES

Table Page

LIST OF FIGURES

Figure Page

Figure Page

Appendix Figure

Figure Page

ABSTRACT

Pfeil, Mark A. Ph.D., Purdue University, December 2014. Solid Amine-boranes as High Performance Hypergolic Hybrid Rocket Fuels and Their Combustion Behavior in a Hypergolic Hybrid Combustor. Major Professor: Stephen D. Heister/Steven F. Son.

Hypergolic hybrid rockets have the potential of providing systems that are simple, reliable, have high performance, and allow for energy management. Such a propulsion system can be applied to fields that need a single tactical motor with flexible mission requirements of either high speed to target or extended loitering. They also provide the possibility for alternative fast response dynamic altitude control systems if ignition delays are sufficiently short.

Amines are the traditional fuel of choice when selecting a hypergolic combination as these tend to react readily with both nitric acid and dinitrogen tertroxide based oxidizers. It has been found that the addition of a borane adduct to an amine fuel tends to reduce the ignition delay by up to an order of magnitude with white fuming nitric acid (WFNA). The borane addition has resulted in fuels with very short ignition delays between 2-10 ms – the fastest times for an amine based fuel reacting with nitric acid based oxidizers. The incorporation of these amine-boranes, specifically ethylenediamine bisborane (EDBB), into various fuel binders has also been found to result in ignition delays between 3-10 ms – the fastest times again for amine based fuels.

It was found that the addition of a borane to an amine increased theoretical performance of the amine resulting in high performance fuels. The amine-borane/fuel binder combinations also produced higher theoretical performance values than previously used hypergolic hybrid rockets. Some of the theoretical values are on par or higher than the current toxic liquid hypergolic fuels, making amine boranes an attractive replacement. The higher performing amine-borane/fuel binder combinations also have higher performance values than the traditional rocket fuels, excluding liquid hydrogen. Thus, amine-borane based fuels have the potential to influence various area in the rocket field.

An EDBB/ferrocene/epoxy fuel was tested in a hypergolic hybrid with pure nitric acid as the oxidizer. Hypergolic ignition occurred repeatably and with short combustor pressurization times of under 100 ms. The regression rate of the fuel exhibited never before observed high pressure dependence regression rates. The presence of a foam like layer on the fuel surface provides an adequate explanation for the observed combustion behavior with a calculated regression rate that depends on pressure raised to the 2nd power. Extrapolation of this theory indicates that amine-borane based fuels could produce high regression rate fuels.

CHAPTER 1. INTRODUCTION

1.1 Introduction

Ignition of rockets was one of the main problems faced by early rocket researchers in the United States which was resolved upon the discovery of hypergolic propellant combinations [1]. Hypergolic ignition involves a process of two chemicals that when they come in contact ignite spontaneously with no outside stimuli. Not only did the discovery of hypergolic propellants solve the ignition problems faced by early engineers, it also greatly simplified their rockets by removing complicated ignition systems. The resulting rockets were very reliable and had the extra benefit of inflight restartability. Other methods to ignite rockets have been developed since these early days including pyrotechnics, torch igniters, or some other complicated ignition system that generally requires resources available at the launch site. These methods have become quite reliable but are typically a single use method making it difficult to restart the motor in flight. They also tend to add extra hardware, weight, and complexity to the system, drawbacks that are not found in hypergolic systems. Hypergolic ignition is thus still the preferred method of operation.

Since the discovery of hypergolic propellants, they have been implemented in a wide range of applications from military use to satellite operation to launch vehicles. The most common hypergolic propellant combinations include liquids based on nitric acid and/or dinitrogen tetroxide (NTO) as the oxidizer and a form of hydrazine as the fuel. These propellants have been used in the Russain R-36 and the United States Titan II intercontinental ballistic missiles and various tactical missiles for military use due to their reliability, long term storability, and quick response necessary for military operation. Satellites and space vehicles that require fast response and accurate thrust maneuvering use these propellants due to their short ignition delays, high performance, and temperature stability. Launch vehicles have used them too: the United States Titan II, the Russian Proton and Tsyklon, and the Chinese Long March 1-4 launch vehicles. Despite the advantages of these nitric acid/NTO/hydrazine hypergols, there are efforts to replace them as they are toxic; especially hydrazine based fuels.

When developing a new hypergolic oxidizer/fuel combination, various parameters are important including performance, ignition delay, storability, temperature stability, toxicity, and reactivity. High performance is necessary for any rocket application. Low ignition delays, under 10 ms for liquid propellants, are required or hard starts will result that tend to lead to and what the industry calls rapid self-disassembly of the hardware. Many systems that use hypergols tend to be stored for a long time and undergo a wide range of temperature changes thus long term storability and temperature stability are required. Low toxicity and reactivity are desirable to reduce the impact on humans and the environment and reduce complexity of the system.

The requirements listed can become limiting factors to any new hypergolic combination. Thus, combinations that use the same fuels but hydrogen peroxide as the oxidizer are not usually considered despite their higher performance as hydrogen peroxide has a high freezing point, decomposes over time, and can detonate. Fluorine based combinations, usually resulting in the highest theoretical performance, are not used as fluorine is toxic, very corrosive, and difficult to handle.

Hypergolic hybrid rockets are a class hypergolic systems that typically use a liquid oxidizer and solid propellant. They provide the same advantages as liquid hypergolic propellants but use less hardware and are simpler, resulting in even more reliable rockets and increased system range. The solid fuel flow rate is typically limited by the surface area and heat feed back to the solid fuel making it difficult for the hypergolic propellants to mix intimately in large quantities and produce hard starts.

Table 1.1 provides a summary of hypergolic hybrid combinations tested in a combustor. Of those considered, toxicity, low melting points, and/or air sensitivity are common attributes making these systems unattractive to implement. For these reasons, there have been very limited flight tests using these materials [2, 3]. In Table 1, theoretical specific impulse (I_{sp}) (calculated using a chamber pressure of 68.05 atm perfectly expanded to atmospheric conditions) and density specific impulse (ρI_{sp}) of these systems is compared to the standard liquid hypergol combination of monomethylhydrazine (MMH) and dinitrogen tetroxide (NTO). Values for several of the materials are not provided as the heats of formation were not available. In general, the hybrid systems are inferior to NTO/MMH that has I_{sp} and ρI_{sp} values of 288.4 s and 344.2 sg/cm^3 respectively at an O/F of 2.2. Such limitations have historically made hypergolic hybrid rockets less attractive compared to their liquid counterparts, and new hypergolic hybrids without these drawbacks are needed.

Table 1.1 Hypergolic hybrid rocket oxidizer and fuel combinations that have been used in experimental rocket combustors.

Fuel Type	Oxidizer	Ignition Delay, ms	O/F	I_{sp}, s	ρI_{sp}, sg/cm^3	C*, m/s	Melting/ Softening Point, K	Comments	Heat of Formation Reference
Tagaform [2, 4]	WFNA	150	3.7	259.8	363.5	1487	346	Unknown Toxicity	[2]
Sagaform A [5]	RFNA	5	-	-	-	-	408	Unknown Toxicity	-
30% p-Toluidine / 70% p-Aminophenol [3, 4, 6]	WFNA	110-122	3.4	255.7	352.3	1466	317	Toxic	[7]
Metatoluene Diamine/Nylon [6, 8, 9]	RFNA/96% Hydrogen Peroxide	-	-	-	-	-	371	Toxic	-
Lithium Aluminum Hydride/Polyethylene [10]	90% Hydrogen Peroxide	-	0.9	304.9	332.9	1760	378-423	Unstable in Air/Toxic	[7, 11]
Manganese Dioxide/Sodium Borohydride/Polyethylene [12, 13]	90% Hydrogen Peroxide	0.2-No Ignition	5.4	268.6	359.3	1567	378-453	Unstable in Air/Toxic	[7, 11]
Difurfurylidene Cyclohexanone/Polyisoprene [14-16]	RFNA	45-255	-	-	-	-	418	Unknown Toxicity	-
Aniline Formaldehyde/Magnesium [17-20]	99% RFNA/1% Ammonium Vanadate	1134-4800	-	-	-	-	423	Toxic	-

1.2 Ignition Delay

The desired ignition delay limit for safe operation of a hypergolic hybrid motor is not clear as the ignition mechanisms controlling hybrid motors is different than liquids. Hard starts occur in hypergolic liquid propellant systems when too much oxidizer and fuel mix in a chamber before combustion is initiated resulting in over pressurizing. Overfilling the combustion chamber in a hybrid motor with excess oxidizer is possible; however, the amount of fuel is limited by the surface area of the fuel grain making it difficult produce excess amounts of uniformly mixed oxidizer and fuel. It is thus possible that ignition delays longer than 10 ms are acceptable for safe motor operation. If hybrids are to replace hypergolic systems that are used for dynamic altitude control, they will need to meet a 10 ms ignition delay criterion.

The ignition delay of the hypergolic hybrid motors which have been tested are provided in Table 1.1. Most of the combinations have ignition delays above 10 ms making them unfit for dynamic altitude control systems but potentially feasible for safe motor operation. Those that are under 10 ms include the manganese dioxide/sodium borohydride/polyethylene and Sagaform fuels. It is suspected that Sagaform uses lithium borohydride to achieve the low ignition delays as its predecessor, Tagaform, used this additive to reduce ignition delays to 2 ms [2, 21]. Thus, unstable, toxic metal hydrides are in part responsible for the low ignition delays. Those motors that have not used metal hydrides obtained ignition delays that are five or more times higher than the 10 ms threshold. This caused several of the motors to use a pyrotechnic igniter [18] or another source for ignition [8, 14].

Prior research has uncovered other solid additives that are hypergolic with hydrogen peroxide and nitric acid based oxidizers. With hydrogen peroxide, ignition delays between 1-10 ms [8, 22] have been observed, and with nitric acid and dinitrogen tetroxide based oxidizers, ignition delays vary between 1.5-150000 ms [4, 15, 16, 19, 23-34]. The incorporation of these additives into fuel binders tends to increase ignition delays to 0.2 ms to not hypergolic for hydrogen peroxide combinations [12, 22, 35] and to 2 ms to not hypergolic for nitric acid based oxidizer combinations [2, 4, 5, 16, 19, 26, 32-34, 36].

The most notable of the additives used for achieving hypergolic ignition with hydrogen peroxide or nitric based oxidizers are metal hydrides. In powder form, several metal hydrides when mixed with hydrogen peroxide or WFNA have achieved ignition delays between 1-10 ms [4, 8, 22, 25, 37]. Many of these substances contain borohydride resulting in ignition delays between 1-8 ms, suggesting that the borohydride is a promoter of hypergolic ignition.

While the ignition delays of metal hydrides are promising, a major drawback typical of many of the metal hydride additives is that they are not stable at atmospheric, especially humid, conditions. Such stability issues make them difficult to manufacture in large quantities or implement in hybrid rocket systems [38] and have led to poor performance, presumably due to fuel grain degradation over time [39]. Additionally, some metal hydrides are pyrophoric and toxic which further complicates fuel grain production and use. These limitations are likely why many of the fuels that incorporate metal hydrides have not been used more extensively.

A common trend for most motors listed in Table 1.1 is an amine based fuel component. When reacting with nitric acid base oxidizers, solid amine additives have achieved ignition delays between 27-4000 ms [23-25] while incorporation of these additives into fuel binders have resulted in ignition delays from 110 ms to not hypergolic [4, 26]. Notably, it is the combination of the amine based materials with a metal hydride in a solid fuel matrix reacted with WFNA or hydrogen peroxide that have achieved the shortest ignition delay times of 2-59 ms [2, 4, 8].

The chemistry responsible for hypergolic ignition of amine based materials is generally understood [40]. Amines have NR_3 groups where R can be hydrogen or some other chemical. These NR_3 groups have a lone pair of electrons that readily attract a H^+ from an acid resulting in a Lewis acid-base reaction. The products of this reaction are a salt, a strong oxidant, and heat generation. The addition of heat accelerates the reaction between the amine and the acid increasing the amount of heat released while the oxidizer reacts with the fuel generating more heat resulting in a runaway reaction and ignition.

The chemistry behind the hypergolic ignition behavior of metal hydride materials has not received much attention. Metal hydrides are a combination of a metal with a positive charge and a hydride group with a negative charge resulting in a material similar to a salt. It is thus possible that a strong acid, with a stronger positive charge, will remove the hydride from the metal and react resulting in heat production and hydrogen generation. The generated hydrogen will then tend to rapidly react with the oxidizer resulting in even more heat generation, faster reactions, and subsequent ignition.

1.3 Regression Rate

Utilization of hypergolic hybrids, or oxidizer and fuel combinations that heterogeneously react exothermically at room temperature, have resulted in hybrid rockets with high fuel regression rates [2, 4, 8-10, 12, 17, 41-43]. Metal hydrides or amine based materials combusting with hydrogen peroxide, WFNA, RFNA, or fluorine are the most notable hypergolic combinations that have produced high regression rates. Metal hydrides based systems have led to 60-400% increase in regression rates [10, 12, 41] compared to the traditional gaseous oxygen and hydroxyl-terminated polybutadiene (HTPB) system [44]. Amine based fuels have resulted in 40-650% [2, 4, 8, 9, 17] increase. These results are displayed in Figure 1.1. Several of these hypergolic combinations have higher regression rates than even paraffin, a fuel that has been cited many times as having high regression rates.

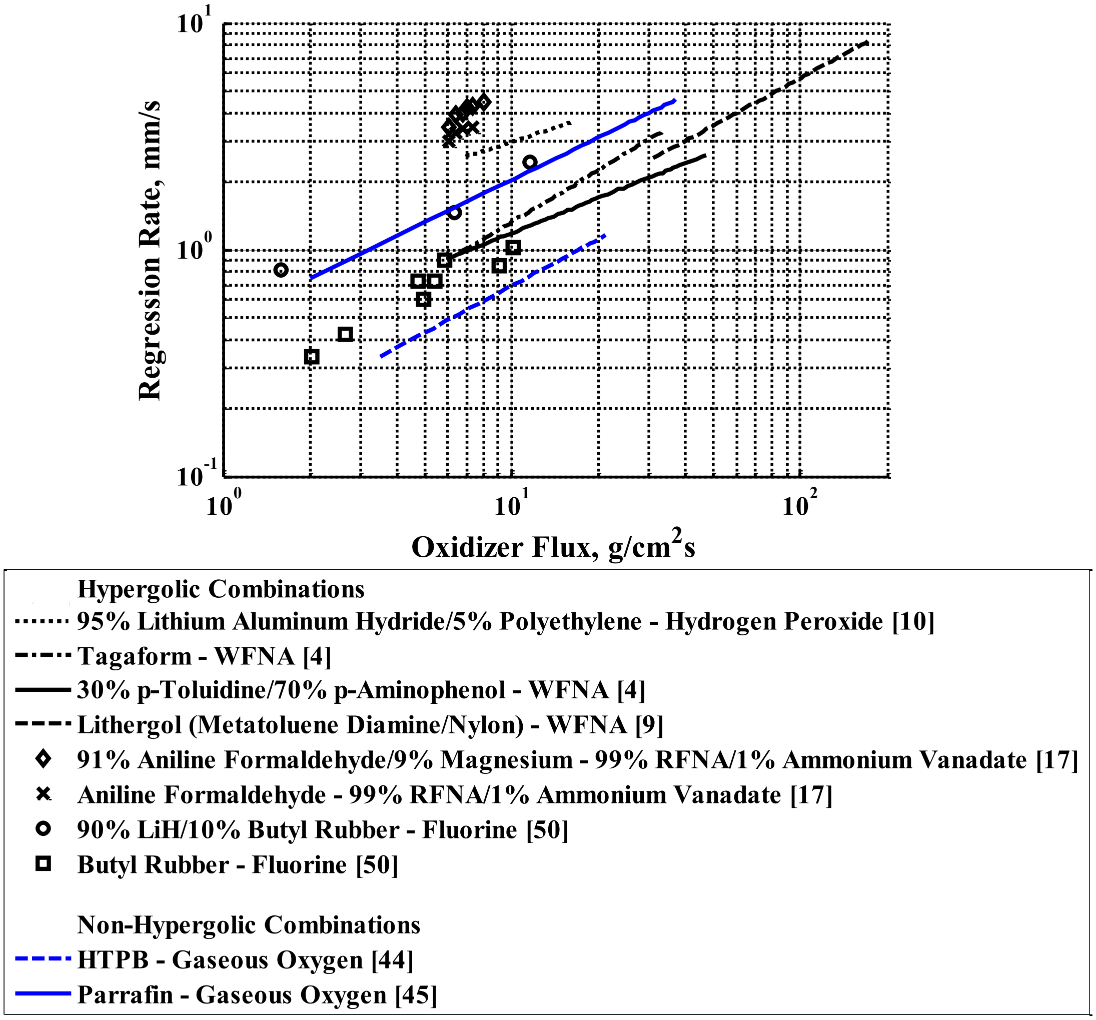

Figure 1.1 Regression rates of hypergolic oxidizer/fuel combinations compared to HTPB/gaseous oxygen and paraffin/gaseous oxygen.

One theory suggests that the higher regression rates are caused by heterogeneous reactions occurring during combustion between the solid fuel and oxidizer [14]. This theory is plausible as regression rates of 0-440% higher than gaseous oxygen/HTPB [44] were obtained by flowing liquid oxidizer over solid fuel resulting in heterogeneous reactions in the absence of combustion [46, 47], regression rates similar to those obtained during combustion. If correct, identifying oxidizer/fuel combinations with fast heterogeneous reaction kinetics could then yield high regression rates.

While studies are lacking in the literature that link high regression rates with heterogeneous reactions, studies do exist that indicate that heterogeneous reactions can occur in hybrid motors. These separate studies were conducted to explore the shift from classical diffusion limited regression rates to kinetically limited, pressure dependent, rates; a behavior common in hypergolic hybrid combinations [9, 14, 42, 46, 48]. Such behavior was first noted by Smoot et al. [42, 49, 50] and attributed to the appearance of heterogeneous reactions at the fuel surface between the fluorine oxidizer and fuel, a hypergolic combination. Since then, researchers have developed three hypotheses to explain these findings: heterogeneous reactions at the surface [14, 42, 48-52], gas phase kinetics [53], 54, 55], or the combination of the two [56]. While there is some theoretical evidence that pressure dependence is caused in part by heterogeneous reactions at the surface, direct and detailed physical observations and measurements of this phenomena are absent in the literature. Definitive experimental evidence for gas phase kinetics is also lacking.

1.4 Motivation

While ignition delays for several hypergolic hybrid motors and solid fuels are acceptable, they tend to use toxic and/or air unstable fuels, presenting a significant drawback to implementation of hypergolic hybrid rocket systems. It is thus important to identify solid additives and binder systems that can achieve short ignition delays while reducing toxicity and achieving long term storability at atmospheric conditions. Once identified, it is important to characterize the combustion behavior of these additive/binder systems in a hybrid combustor in order to validate fast ignition in a motor configuration and to identify mechanisms controlling combustion behavior.

1.4.1 Amine-boranes

A class of materials that have the potential to achieve the desired characteristics of a hypergolic hybrid fuel are amine-boranes. They are amine based chemicals that are typically hydrogen dense and are somewhat similar to many of the metal hydrides in that they have a borane (BH_3), whereas the metal hydrides have a tetrahydroborate (BH_4). The high hydrogen content would suggest that amine-boranes could be a high performance fuel due to the low molecular weight of hydrogen and hydrogen combustion products. The hydrogen content could also promote better combustion due to its high diffusive and kinetic properties. This may be why Weismiller et al. observed an increase in C* efficiency of a hybrid rocket motor when adding ammonia borane to paraffin reacting with gaseous oxygen [57]. Other experimental work indicates that small quantities of amine-boranes can notably influence combustion behavior [57-61].

Amine-boranes, for which data is available, tend to be hypergolic with short ignition delays of 4-80 ms for powder samples [26, 27] and 64-1264 ms for powders cast in fuel binders when reacted with RFNA/WFNA [26]. It appears that the borane adduct tends to lower the ignition delay compared to their amine counterparts. Liquid ammonia is not hypergolic with WFNA [62], and the ignition delay of trimethylamine is not reported. Their counterparts ammonia borane and trimethylamine-borane, both air stable and not toxic, have ignition delays of 80 [27] and 8 [26] ms respectively. These would indicate that other amine-borane adducts could achieve fast ignition delays; however, these are only a few examples and further research needs to be done in this area.

Despite the positive results obtained when using several amine-boranes as hypergolic additives and combustion modifiers, relatively little work has been done to fully investigate amine-boranes. It is unknown if amine-boranes will always provide low ignition delays, or if the materials already investigated happened to be anomalies. Their combustion behavior in a hypergolic hybrid rocket environment is an area that has received no attention making it difficult to determine how useful they could be as an actual rocket propellant. It is our intent to study more thoroughly these materials, investigating their hypergolic ignition behavior and the mechanisms controlling combustion.

1.4.2 Objectives

The purpose of my research is to provide insight into the hypergolic ignition and combustion behavior of solid amine-boranes as a hybrid rocket fuel. Particular emphasis will be made using EDBB as a hypergolic hybrid rocket fuel additive. This will be accomplished through the following objectives:

- Validate theory that the addition of the borane adduct to an amine will result in shorter ignition delays
- Evaluate the performance potential of the amine-boranes in a hybrid rocket system
- Identify a binder system compatible with amine-boranes that will allow for short ignition delay hypergolic hybrid fuels

- Characterize the ignition behavior of hypergolic hybrid fuel in a rocket combustor
- Characterize the combustion mechanisms controlling the combustion behavior of the hypergolic fuel in a hybrid rocket combustor

The chapters that follow will discuss the methods used and the results obtained to achieve these objectives. Specifically, the amine-boranes used in this experiment and the fuel binder system will be discussed in CHAPTER 2. CHAPTER 3 will discuss the experimental methods used to achieve these objectives. In CHAPTER 4, the results of the small scale experiments investigating hyerpgolic ignition behavior, theoretical performance, and general combustion behavior at atmospheric conditions will be presented. CHAPTER 5 will present the results obtained from the hypergolic hybrid combustor including ignition and general combustion behavior. CHAPTER 6 will provide an in-depth analysis of the combustion behavior providing analytical methods to explain the observed combustion behavior. CHAPTER 7 will provide some concluding thoughts and suggestions for future work.

CHAPTER 2. FUELS

2.1 Amine-boranes and Amines

The amine-boranes used in these experiments were produced by the group of Professor Ramachandran in the Purdue Chemistry department. The amines were purchased from commercial sources and were purified by distillation if liquid or recrystallization if solid before use. The purification process was also performed by Professor Ramachandran's group. All of the amine-boranes were in solid form while amine materials were either liquid or solid. A list of these materials is provided in Table 2.1, and images of the amine-boranes are provided in Figure 2.1.

Table 2.1 A list of amine-boranes and amines used in these experiments and some related properties.

Fuel	Hydrogen wt.%	Boron wt.%	Molecular Formula	Phase	Toxicity	Air Stability	Label No.
EDBB	16.1	24.6	$C_2H_{14}B_2N_2$	Powder	Irritant	Stable[1]	1
Ethylenediamine	13.4	-	$C_2H_8N_2$	Liquid	Toxic	Not Stable	2
Cyclohexylamine-borane	14.3	9.6	$C_6H_{16}BN$	Powder	-	-	3
Cyclohexylamine	13.3	-	$C_6H_{13}N$	Liquid	Toxic	Not Stable	4
N,N-Dimethylpiperazine-bisborane	14.2	15.2	$C_6H_{20}B_2N_2$	Powder	-	-	5
Dimethylpiperazine	12.4	-	$C_6H_{14}N_2$	Liquid	Harmful	Stable	6
N-Methylpiperazine-bisborane	14.2	16.9	$C_5H_{18}B_2N_2$	Powder	-	-	7
N-Methylpiperazine	12.1	-	$C_5H_{12}N_2$	Liquid	Toxic	Hygroscopic	8
Tetramethylethylenediamine-bisborane	15.4	15.0	$C_6H_{22}B_2N_2$	Powder	-	-	9
Tetramethylethylenediamine	13.9	-	$C_6H_{16}N_2$	Liquid	Toxic	Sensitive	10
Trimethylamine-borane	16.6	14.8	$C_3H_{12}BN$	Powder	Irritant	Stable	11
Trimethylamine[2]	15.3	-	C_3H_9N	Gas	Toxic	Sensitive	12
Piperazine-bisborane	14.2	19.0	$C_4H_{16}B_2N_2$	Powder	-	-	13
Piperazine	11.7	-	$C_4H_{10}N_2$	Powder	Harmful	Hygroscopic	14
2,6-Dimethylpiperidine-borane	14.3	8.5	$C_7H_{18}BN$	Powder	-	-	15
2,6-Dimethylpiperidine		-	$C_7H_{15}N$	Liquid	Irritant	Stable	
n-Propylamine-borane	16.6	14.8	$C_3H_{12}BN$	Powder	-	-	16
Propylamine		-	C_3H_9N	Liquid	Toxic	Sensitive	
Piperidine-borane	14.3	10.9	$C_5H_{14}BN$	Powder	-	-	17
Piperidine		-	$C_5H_{11}N$	Liquid	Toxic	Stable	
Ammonia Borane	19.6	35.0	H_6BN	Powder	Irritant	Stable[1]	18
Ammonia[2]	17.8	-	H_3N	Gas	Toxic	Stable	19

[1] Based on our observations of the materials synthesized. [2] Not used in these experiments but listed as a reference.

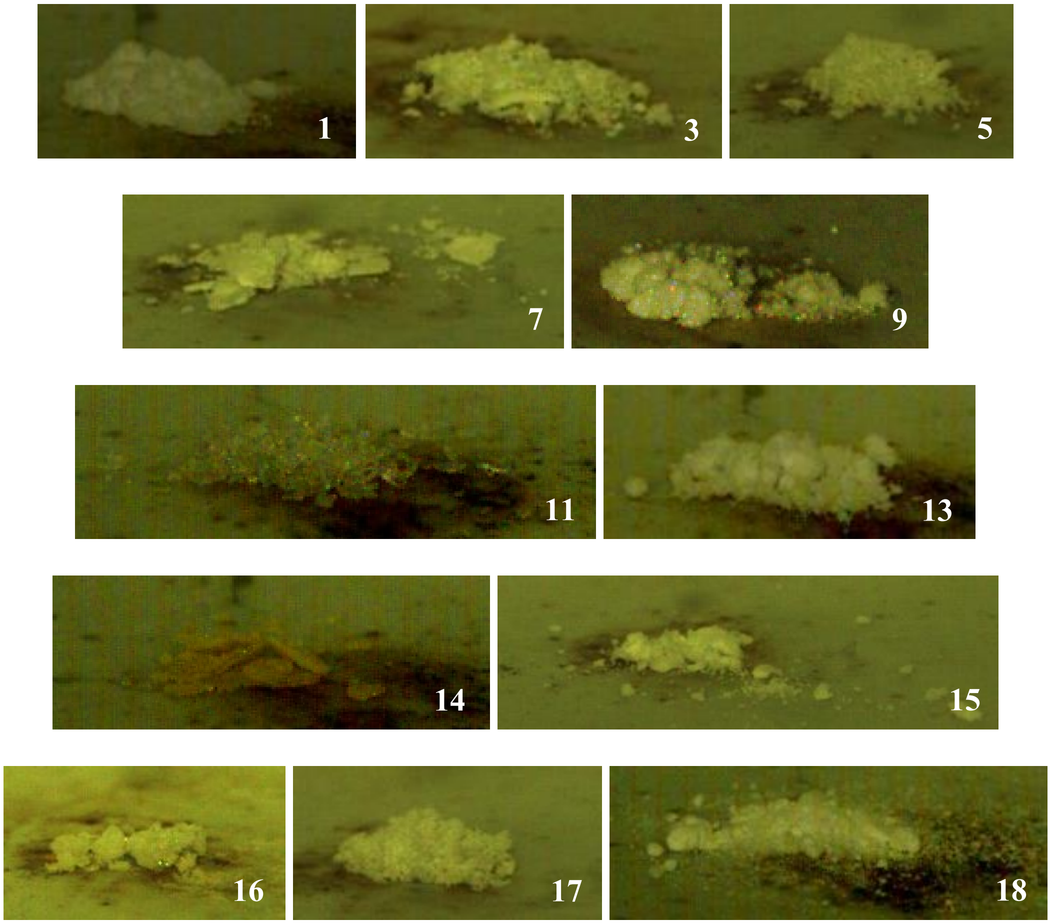

Figure 2.1 Images of the powders used in these experiments corresponding to Table 2.1.

Two procedures were utilized for the preparation of EDBB powder as discussed by Ramachandrand et al. [63]. The former involved the nucleophilic displacement of dimethyl sulfide from commercial borane-methyl sulfide (BMS) in solvent. The amine-borane produced by this protocol was coarse powder and will hereafter be referred to as EDBB A powder. The latter procedure involved the nucleophilic displacement of ammonia from a tetrahydrofuran (THF) solution of ammonia borane synthesized according to the procedure described by Ramachandran and Gagare [64]. The EDBB prepared by this protocol appeared more crystalline and fine and will hereafter be referred to as EDBB B powder.

The latter procedure was applied for large-scale production of EDBB due to the air- and moisture-stability of ammonia borane compared to the extreme care necessary in handling BMS, as well as the low human olfactory threshold of stenchy dimethyl sulfide. This powder was stored at atmospheric conditions for over 2 years before use in these experiments demonstrating long term stability of EDBB.

The other amine-boranes used in this study were prepared using a similar method as that used to produce EDBB or as described elsewhere [65, 66].

2.1.1 Toxicity and Air Sensitivity

The toxicity and air sensitivity can greatly influence the implementation of a material, and it is suspected that these factors are a reason why hypergolic hybrids have not been used frequently, as discussed in CHAPTER 1. The toxicity and air stability of the materials used in these experiments is provided in Table 2.1 and comes from material safety data sheets (MSDS) provided by the Sigma-Aldrich website [67]. Trimethylamine was not used in these experiments but is listed for a reference.

Many of the amine materials are either classified as harmful or toxic. Most of them are not air stable either. While many of the amine-boranes have not been classified, those for which the toxicity and stability is known provide interesting trends. These materials tend to indicate that the addition of the borane adduct to the amine tends to make the material not toxic and only an irritant. Furthermore, the air stability of amines improve when a borane is added resulting in air stable chemicals. However, dimethylamine (not used in this study), classified as harmful, becomes toxic when converted to dimethylamine-borane, indicating that the trends observed above might not always hold true.

2.2 Powder Characterization

The equipment to measure particle size distributions requires the index of refraction of the powder. Therefore, the index of refraction of EDBB was first obtained following the procedures outlined by Saveyn et al.[68] and Malvern Instruments Ltd. [69] and using a Fisher Scientific (model #334620) refractometer, see Figure 2.2, with anhydrous methanol as the solvent. In short, measurements are made of a pure solvent and then of mixtures of the solvent and the material being investigated. The index of refraction varies linearly with the concentration of material in the solvent until the solution is saturated. This linear trend can then be extrapolated to the pure substance of the material being investigated in order to determine its index of refraction. This method was applied to EDBB B powder/methanol mixtures giving the results provided in Figure 2.3. The extrapolation of this data to 100 wt.% EDBB yields an index of refraction of 1.868.

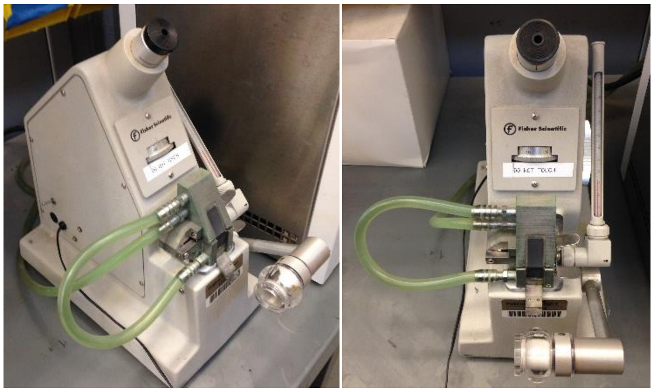

Figure 2.2 A Fisher Scientific (model #334620) refractometer used to measure the index of refraction.

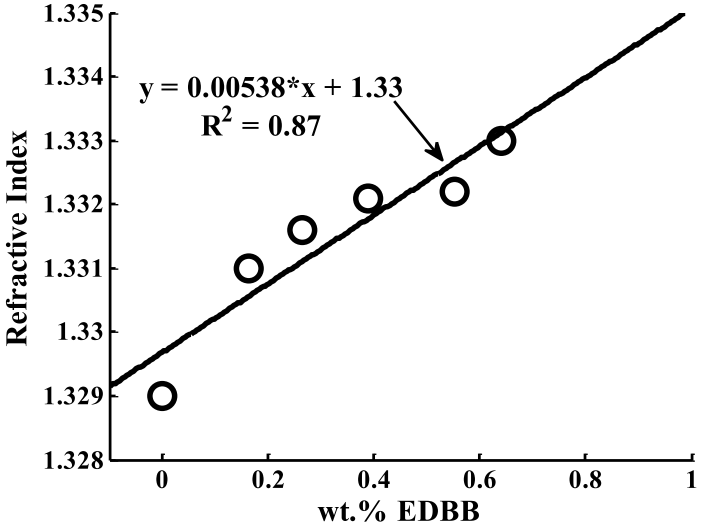

Figure 2.3 Refractive index of EDBB/methanol mixtures as a function of EDBB B concentration.

Particle size distributions of the two EDBB A and B powders were measured based on a volume % basis using a Malvern Mastersizer Hydro 2000 μP with hexanes as the dispersant. Both A and B powders exhibit a relatively single modal distribution, see Figure 2.4. The majority of the particles for the EDBB A powder are between 100-2000 μm with the highest volume % around 475 μm. The size of particles for the EDBB B powder is generally smaller falling between 10-500 μm with the highest concentration around 40 μm. Both powders show a small percentage of particle sizes below these ranges; the EDBB B powder having some nano sized particles.

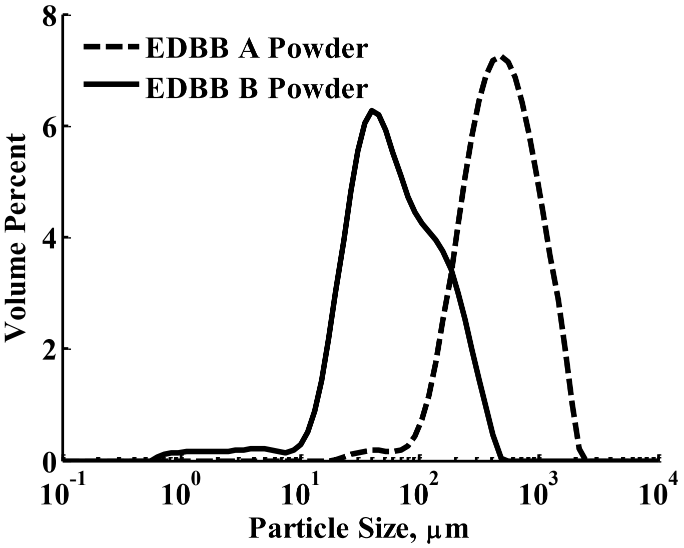

Figure 2.4 EDBB particle size volume distribution for both EDBB A and B powders.

A Hirox KH-8700 optical microscope, see Figure 2.5, was used to take high resolution images of both EDBB powders. Images of the EDBB powders indicate relatively clear, crystalline particles, as indicated in Figure 2.6. The angled facets and protruding surfaces of the EDBB A particles provide a clear indication of the crystalline structure of these particles. Crystalline structures are also apparent in the EDBB B powder. The EDBB A particles generally appear to be somewhat rectangular or elongated in one direction while the EDBB B particles are irregular. These images also provide general sizing of the particles indicating that the EDBB A powder size is on the order of 100 μm while the EDBB B powder is an order of magnitude smaller; sizes that confirm the results made by laser diffraction measurements.

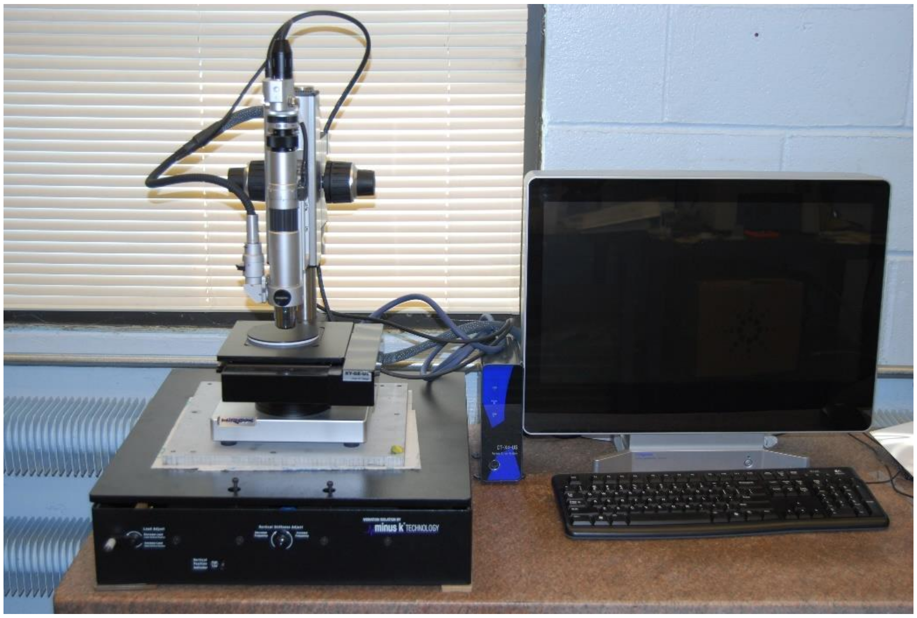

Figure 2.5 A Hirox KH-8700 optical microscope used to make optical measurements of the powders.

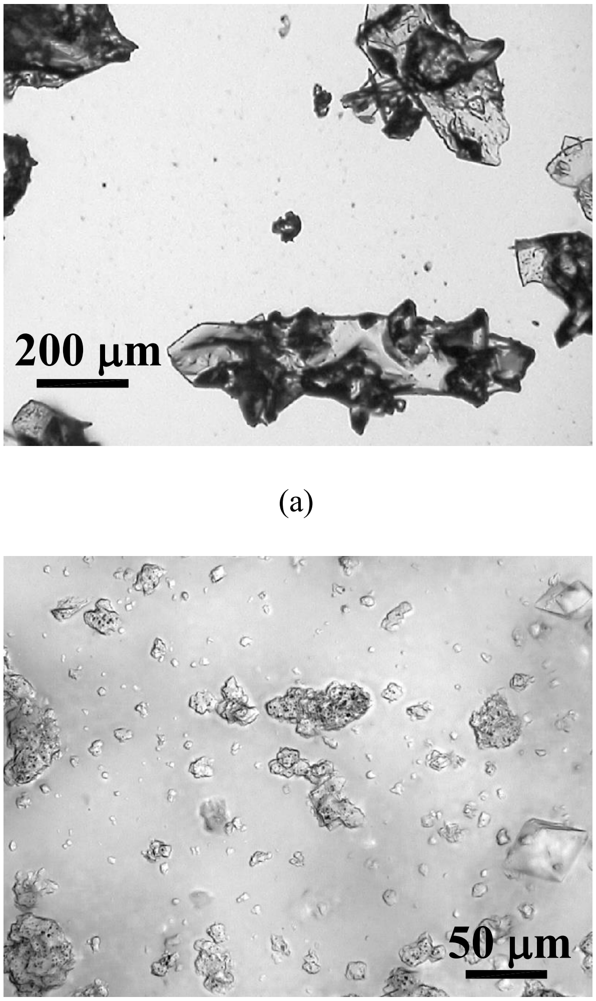

(a)

(b)

Figure 2.6 Optical microscopy images of (a) EDBB A and (b) EDBB B powders.

Electrostatic discharge (ESD) sensitivity experiments were performed with 0.003-0.004 g of confined EDBB B powder in air, per the standard MIL-STD-1751 [70]. The standard threshold of 250 mJ was discharged onto the prepared sample. A reaction or “Go” condition was characterized by any visible or audible reaction.

The standard method for testing ESD sensitivity resulted in no reactions for 10 separate experiments for EDBB B powder. As very little oxidizer, air in this case, was in the confined space, it was not likely that the EDBB powder would react; therefore, seven of the experiments were repeated with unconfined powder in the conductive cup allowing air to surround the sample. All of the unconfined experiments resulted in a reaction consisting of a green flash followed by smoke generation. This suggests that EDBB powder is susceptible to electrical energy discharge; however, reaction leading to ignition will not occur unless an adequate oxidizing environment is available. It is thus suggested that EDBB powder be handled appropriately to reduce accidental ignition.

2.3 Fuel Matrices

The EDBB powder was incorporated into solid fuel matrices for further characterization. The fuel matrices consisted of pressed pellets and mixtures of EDBB and binder cured into a pellet. The binders used were HTPB, R-45, Sylgard 184, dicyclopentadiene (DCPD), paraffin, Permatex High-Temperature RTV Silicone, and Envirotex-Lite epoxy. All binders that required combining several chemicals were well mixed by hand before introducing any amine-borane.

The HTPB typically consisted of 86.4 wt.% R-45, 5.9 wt.% dioctyl adipate, and 7.7 wt.% isophorone diisocyanate. Other R-45 curatives were implemented including 9.5 wt% Isonate™ 143L (with 90.5 wt.% R-45), 11.9 wt.% Desmodur® N 3200 (with 88.1 wt.% R-45), and 11.5 wt.% Desmodur E 744 (with 88.5 wt.% R-45). The ratios were calculated such that all of the OH bonds in the binder would be properly cross-linked providing for a complete cure of the binder system. These binders were cured at 333.2 K for 120 hours.

The DCPD consisted of 99.74 wt.% dicyclopentadiene, 0.19 wt.% triphenylphosphine, and 0.08 wt.% Grubbs 1st generation catalyst. To mix DCPD, specific steps were used to produce consistent binder properties. As the monomer of DCPD is solid at room temperature, it was first placed at 333.2 K for several minutes to cause it to melt. The amount of monomer was then measured out and triphenylphosphine was added and mixed until dissolved. The Grubbs catalyst was placed in a 1 dram vile and dissolved in toluene. This solution was added to the monomer/triphenylphosphine solution (the 1 dram vile being rinsed out with toluene to ensure all of the Grubbs catalyst was transferred) and then stirred vigorously by hand (for at least one minute) until the mixture turned amber in color. At this point, fuel additives could be introduced into the DCPD uncured binder. These binders were cured at 333.2 K for 24 hours.

Both Sylgard 184 and Envirotex-Lite epoxy required equal volume quantities for resin and hardeners and were thus prepared accordingly. Sylgard required curing at 333.2 K for 48 hours; however, Enirotex-Lite epoxy cured at room temperature in 24 hours. Permatex High-Temperature RTV Silicone came premixed from the vendor and began curing on contact with air at room temperature, becoming fully cured in 24 hours.

The pressed pellets consisted of EDBB mixed with various quantities of fuel binders. The uncured binder and EDBB were first hand mixed to wet the EDBB to protect from accidental ignition during mixing. Mixtures were then placed on a Resodyn LabRam acoustic mixer, see Figure 2.7, and mixed at 50-80% power for 10 minutes. If the amount of EDBB compared to fuel binder was high enough that all of the EDBB could not be wetted by hand mixing, the mixture was put under argon before mixing on the Resodyn mixer. Pressed pellets were produced by applying up to 109.2 MPa on the mixture in a 10 mm diameter stainless steel die, Figure 2.8, using a Carver press, Figure 2.9. The powder was pressed for 10 minutes and then removed producing cylindrical fuel pellets from 1-5 mm long. The pellets were either left to cure at atmospheric conditions or elevated temperatures depending on the binder type.

Figure 2.7 A Resodyn LabRam acoustic mixer used to mix powders and binders.

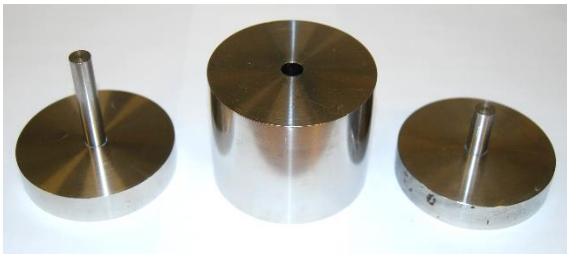

Figure 2.8 A 10 mm diameter die used for pressing fuel pellets.

Figure 2.9 The Carver press used to press fuel mixtures.

Powder EDBB cast into fuel binders followed similar procedures as the pressed pellets up to mixing on the Resodyn. After being mixed, the material was put under vacuum to remove any entrained gas. The material was then transferred to 12 mm diameter cylindrical molds or left in a flat, open container. These materials were allowed to cure either at atmospheric or elevated temperatures.

The combinations of EDBB B powder and binders are provided in Table 2.2. The casting method of these fuels depended on the viscosity of the resulting mixture: mixtures that had low enough viscosity to be poured, mixtures that had the appearance of play dough that could not be poured nor pressed but could be molded by hand, see Figure 2.10, and mixtures that were viscous enough or powder like that could be pressed, see Figure 2.11.

Table 2.2 Fuel binders used with EDBB as the hypergolic fuel additive.

Binder	% Binder	Casting Method	Notes
HTPB	70	Poured	Partially Cured/Small Voids
HTPB	60	Poured	Partially Cured/Small Voids
HTPB	50	Molded	Partially Cured/Small Voids
HTPB	42	Molded	Partially Cured/Few Large Voids Resulting in Fuel Sections with No Voids
HTPB	20	Pressed	Partially Cured/No Voids
R-45	18	Pressed	-
DCPD	40	Molded	Did Not Cure
Sylgard	20	Pressed	Did Not Cure
Sylgard	70	Poured	Did Not Cure
Paraffin	70	Pressed	Pressed by Hand/Solidified
Paraffin	50	Pressed	Pressed by Hand/Solidified
RTV	70	Molded	Cured
RTV	50	Molded	Cured
RTV	20	Pressed	Cured
Epoxy	70	Poured	Cured
Epoxy	50	Molded	Cured
Epoxy	40	Molded	Cured
Epoxy	30	Pressed	Cured
Epoxy	20	Pressed	Cured

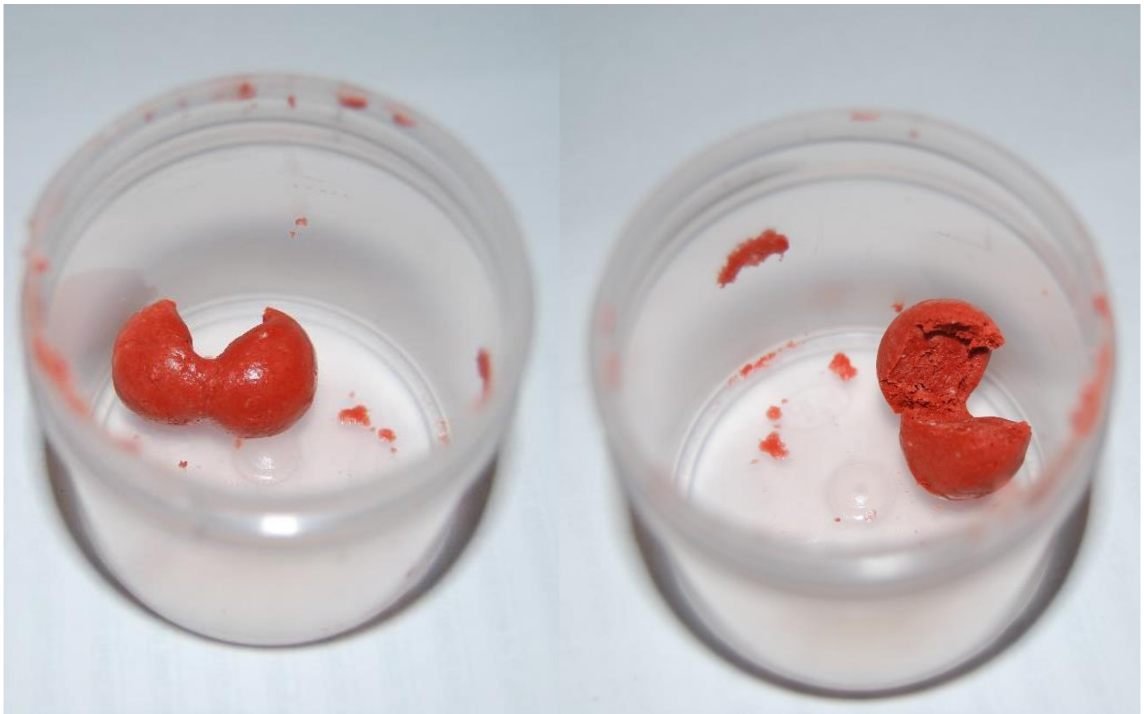

Figure 2.10 A mixture of 50% EDBB/50% RTV after being mixed on the Resodyn.

(a) (b)

Figure 2.11 A mixture of 80% EDBB/20% RTV after being mixed on the Resodyn (a) and then pressed in the carver press (b).

Samples of EDBB and HTPB composites resulted in gas generation during the curing process producing voids in the cured sample. Such behavior was observed with all four HTPB curatives used in this study. One particular ration of 42 wt.% HTPB/58 wt.% EDBB did produce several sections with no voids allowing for some experimentation. Cured fuel samples exhibited variations of structural characteristics over time from firm and flexible to soft and deformable composites. Once soft, no further changes in the composite were observed. This behavior led to the designation of partially cured. These characteristics suggest that EDBB is not compatible with the isocynate curatives used to crosslink the R-45 resin.

Both DCPD and Sylgard 184 did not cure when mixed with EDBB. The R-45 did not cure either, but it was not expected to cure. It was used as an additive in low concentrations with EDBB to form pressed pellets.

Paraffin, epoxy, and RTV were the best fuel binders that were able to either solidify or cure when mixed with EDBB. Paraffin was used briefly but not pursued as it has a low melting temperature and resulted in long ignition delays compared to other binders, see Section 4.1. The RTV binder received more use; however, it suffers from having filler (silicon oxide and iron oxide) already in the binder reducing its potential performance. Epoxy was used the most as it was the binder that had the highest potential theoretical performance that also consistently cured with the EDBB additive.

2.4 Rocket Combustor Fuel Grain

The fuel grain composition selected for use in the hybrid rocket combustor consisted of 80 wt.% EDBB, 1 wt.% ferrocene, and 19 wt.% Envirotex-Lite epoxy. The epoxy binder was used due to its compatibility with EDBB, processability, and higher performance than other binders that had similar qualities. Eighty wt.% of EDBB was selected as this produced reasonably short ignition delays, see Section 4.1.3, while allowing for as much EDBB as possible in the fuel grain. The objective was to study EDBB as a hypergolic fuel; therefore, as little binder as necessary to produce a structurally sound fuel grain was implemented. One wt.% ferrocene was added to the mixture mainly to provide a more bimodal particle size distribution while no detracting from the hypergolicity of the fuel; ferrocene itself is hypergolic. The bimodal particle distribution enabled better mixing and processing of the material, whereas EDBB by itself could be difficult to mix at such a high concentration due to its small particle size.

Mixing of the grain consisted of first mixing the epoxy resin and hardener at equal volume ratios (54.2 wt.% resin to 45.8 wt.% hardener) and then mixed for two minutes by hand. The epoxy, ferrocene, and EDBB were combined and mixed by hand to wet the particles. The mixture was placed under argon and then mixed on the Resodyn LabRam for two 10 minute intervals at 65% power, producing the mixture shown in Figure 2.12. The mixture was then placed in a cylindrical die, see Figure 2.13, and pressed on the Carver press at 88.6 MPa for two five minute intervals. Only enough material was pressed each time to produce around 80 mm long segments. A resulting fuel, shown in Figure 2.14, typically had an outer diameter of 37.6 mm and an inner diameter of 12.7 mm. The fuel grains were then allowed to cure at room temperature for 48 hours.

Figure 2.12 A mixture of 80 wt.% EDBB/1 wt.% ferrocene/19 wt.% epoxy after being mixed on the Resodyn LabRam mixer for a total of 20 minutes.

Figure 2.13 The cylindrical die used to press EDBB/ferrocene/epoxy fuel grains.

Figure 2.14 A EDBB/ferrocene/epoxy cylindrical fuel grain that has been pressed. Striations on side of fuel grain due to pushing grain out of pressing die.

The 80 mm long fuel segments were epoxied into phenolic tube liners for total fuel grain lengths of 152 mm or 304.8 mm long. The resulting overall fuel grain properties are presented in Table 2.3. The average theoretical mass density (TMD) were all above 94 % indicating that the fuel grains had little to no voids.

Table 2.3 Fuel grain properties that were used in the hybrid rocket combustor.

Mass, g	Avg. Inner Diameter, mm	Avg. Outer Diameter, mm	Avg. Length, mm	Avg. Density, g/cm^3	Avg. % TMD
128.233	12.7	37.6	158.3	0.826	95.0
127.910	12.7	37.6	158.4	0.821	94.4
256.264	12.7	37.6	314.8	0.828	95.3
256.288	12.6	37.5	318.5	0.820	94.3
255.513	12.7	37.5	316.4	0.824	94.8
127.368	12.6	37.6	151.7	0.854	98.3
255.087	12.7	37.5	310.2	0.841	96.7

It was determined after the first combustor experiment that the amount of surface area available on the fuel grain port was too low, causing low fuel flow rates. Thus, the subsequent fuel grains were sawed with a 2.54 mm diameter rod saw to produce 8 slots with a depth of 2.54 mm from the initial fuel port surface, see Figure 2.15. Production of the slots occurred before the fuel grains were epoxied into the phenolic cartridges.

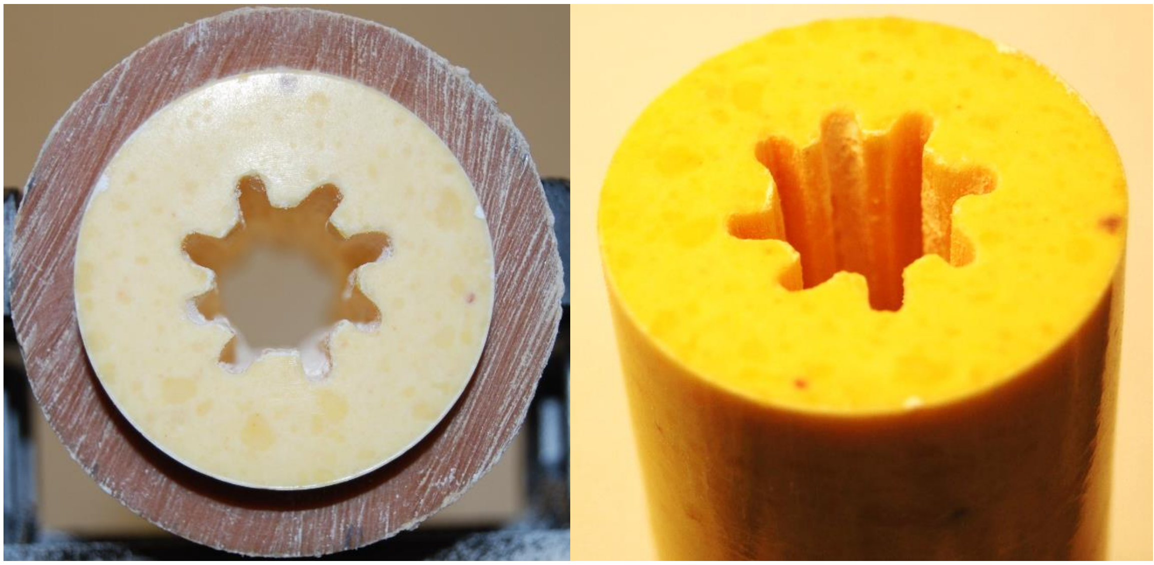

Figure 2.15 Eight slots that were cut into the fuel grains after curing using a 2.54 mm diameter rod saw.

CHAPTER 3. EXPERIMENTAL METHODS

3.1 Hypergolic Droplet Ignition Experiment

The ignition behavior and ignition delay time of both powder and solid fuel samples were studied using a droplet ignition apparatus, see Figure 3.1. A droplet of 99% WFNA, purchased from Sigma Aldrich, was dropped from a syringe at a height of 127 mm onto either a pile of loose powder or cylindrical sections of the solid fuel matrices. The subsequent ignition delay was measured as the interval between initial droplet contact with the fuel surface to first visible light emission. The droplets of WFNA in this experiment had an average diameter of 2.91 ± 0.02 mm. The powders were either used as synthesized or sieved using 45 and 150 μm sieves to produce uniform particle distributions. Various fuel surfaces were used including pressed surfaces for pressed pellets, surfaces cut with a razor blade, and surfaces sanded with 100 grit sandpaper. The rectangular Teflon base on which the fuel sample was placed was cleaned between each experiment to prevent cross contamination. Ignition delays and images were recorded through the use of a high speed color Phantom v7.3 camera and a Nikon 28-105 mm lens. A 3x4 array of Cree XLamp XP-G Star LED lights were used for illumination.

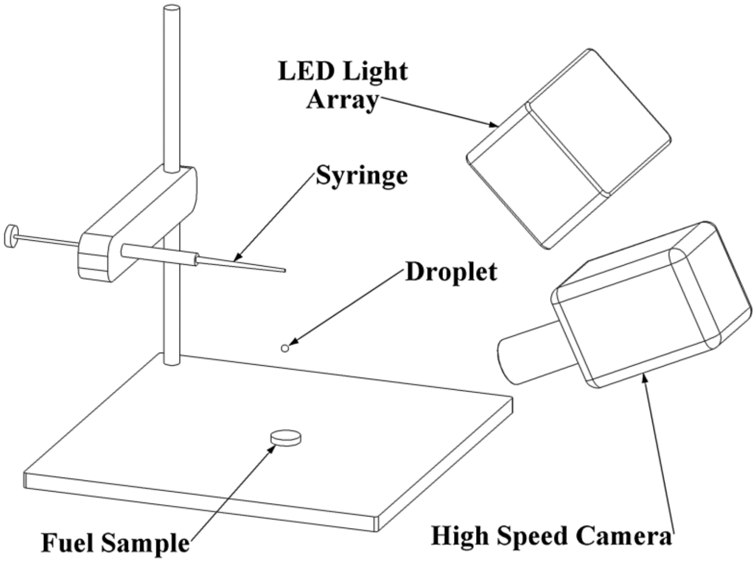

Figure 3.1 Droplet ignition experiment for measuring hypergolic ignition delay and observing ignition behavior.

3.2 Intrinsic Properties Experimental Methods

The amine-boranes densities were measured 10 times using an AccuPyc II 1340 Pycnometer using helium gas pressurized to 0.17 MPa following the ASTM standard B923 [71].

The heat of combustion of the amine-borane powders were measured using a Parr 1281 bomb calorimeter, see Figure 3.2. Prior to burning in the bomb calorimeter, fuel pellets of about 0.3 g were made by pressing powder in a cylindrical die with a diameter of 10 mm. Pellets were pressed at 110.3 MPa for 10 minutes using a Carver press. Three pellets of each material were then combusted in a pure oxygen environment in the bomb calorimeter.

Figure 3.2 A Parr 1281 bomb calorimeter to measure the heat of combustion.

Condensed phase products were observed in the sample holder after bomb calorimeter operation. The heat from these condensed phase products is not fully measured by the bomb calorimeter because they do not come into contact with the wall, yielding a lower limit for the heat of combustion measurements. Because of this, several of the amine-boranes were also combusted in a loose powder form contained in a sectioned Kimtech Science kimwipe, which resulted in a reduced amount of condensed phase products in the sample holder, and thus improved accuracy. The heat of combustion of the kimwipes were measured separately and removed from the combined heat of combustion of the powder and kimwipe to determine the value for the loose powder.

The heats of formation of the amine-boranes were determined using the heat of combustion values measured and assuming complete reaction after the following manner,

$$C_aH_bB_cN_dO_{e(solid)} + \left(a + \tfrac{1}{4}b + \tfrac{5}{4}c - \tfrac{1}{2}e\right) O_{2(gas)} \rightarrow$$

$$aCO_{2(gas)} + \tfrac{1}{2}(b + c)H_2O_{(liquid)} + \tfrac{1}{2}dN_{2(gas)} + cHBO_{2(solid)} \quad (3.1)$$

coupled with,

$$\Delta H_{combustion} = H_{reactants} - H_{products} + \Delta nRT \quad (3.2)$$

where $\Delta H_{combustion}$ is the heat of combustion, $H_{reactants}$ is the heats of formation of the reactants, $H_{products}$ is the heats of formation of the products, Δn is change of moles of gas from reactants to products, R is the ideal gas constant, and T is the temperature in the bomb calorimeter. This method does not account for the energy not measured by the bomb calorimeter from the condensed phase HBO_2 products. Equations 3.1 and 3.2 were thus modified to account for this unmeasured heat resulting in the following equations,

$$C_aH_bB_cN_dO_{e(solid)} + \left(a + \tfrac{1}{4}b + \tfrac{3}{4}c - \tfrac{1}{2}e\right) O_{2(gas)} \rightarrow$$

$$aCO_{2(gas)} + \tfrac{1}{2}bH_2O_{(liquid)} + \tfrac{1}{2}dN_{2(gas)} + \tfrac{1}{2}cB_2O_{3(liquid)} \quad (3.3)$$

and,

$$\Delta H_{combustion} = H_{reactants} - H_{products} + \Delta nRT + n\int_T^{T_{B_2O_3}} C_P dT \quad (3.4)$$

where n is the number of moles of B_2O_3 in the products, $T_{B_2O_3}$ is the temperature the B_2O_3 products achieved in the bomb calorimeter, and C_P is the heat capacity. Liquid phase B_2O_3 products were assumed in this calculation as that is what equilibrium calculations in both Cheetah 6.0 [72] and NASA CEA [73] predict will be present in the condensed phase at the elevated combustion temperatures. The C_P value for B_2O_3 as a function of temperature was obtained from the NIST Chemistry WebBook [7]. The upper limit for $T_{B_2O_3}$ could theoretically achieve 2100 K before transitioning to gaseous products at the bomb calorimeter pressure of 2.76 MPa according; thus, this temperature was used in the calculations.

The two sets of Eqns. 3.1 and 3.2 and Eqns. 3.3 and 3.4 provide limits for determining the heat of formation. While it is difficult to determine what quantity of boron products remain in the sample holder when burning a pressed pellet, assuming all the products remain in the sample holder and using Eqns. 3.3 and 3.4 can provide an upper limit of what the heat of formation could be. Equations 3.1 and 3.2 can be used to determine the lower limit of the heat of formation under the assumption that all of the boron products leave the sample holder and their heat is transferred to the bomb calorimeter wall. The method using a kimwipe to burn loose powder mentioned earlier can be used with Eqns. 3.1 and 3.2 resulting in some rise of the lower limit of the heat of formation.

3.3 Opposed Burner Experiment

Fuel pellets were combusted with oxygen at ambient pressure in an opposed flow burner apparatus designed after a Penn State experiment [74], see Figure 3.3, to observe combustion behavior. The fuel pellet holder was 12 mm in diameter and was placed 10 mm below the exit plane of a flow conditioning nozzle. Gaseous oxygen was regulated by an Omega FMA-A2317 flow meter and subsequently passed through the flow conditioning nozzle to impinge on the fuel surface. An Omega LD620-25 linear variable displacement transducer (LVDT) was placed underneath the fuel pellet to record its displacement and thus regression rate. A 30 gauge tungsten wire was placed over the fuel pellet while a spring was placed underneath to keep the surface in plane with the sample holder during combustion. The regression rate was determined following the method detailed by Zaseck *et al.* [75].

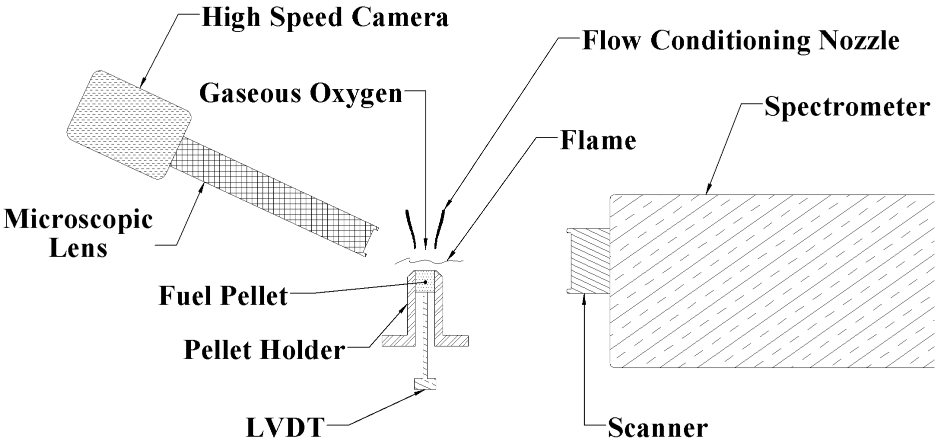

Figure 3.3 Gaseous oxygen opposed burner with spectrometer and high speed surface imaging setup.

Both visual and infrared (IR) data were obtained during the combustion of fuel pellets in the opposed burner. General combustion behavior was observed using a standard speed Cannon XL2 3CCD video camcorder. High speed colored surface imaging was made through the use of a Phantom v7.3 paired with an Infinity Photo-Optical Company K2 Long Distance Microscope lens. Spectral IR data of the flame region above the fuel pellet was obtained through the use of a Spectraline ES100 IR Spectrometer. The spectrometer operated at 1320 Hz and was programmed to scan back and forth across the flame zone providing apparent emittance and intensity as a function of wavelength. Data is post processed to determine temperature by fitting grey body profiles to intensity profiles following the same procedures outlined by Terry *et al.* [75] and further expanded upon by Terry [77].

3.4 Hybrid Rocket Combustor Experiment

The hybrid rocket combustor used in these experiments consisted of a nitrogen pressurization system, liquid oxidizer tank and feed system, and a modular stainless steel combustion chamber. The assembled hardware is shown in Figure 3.4 while a plumbing and instrumentation diagram of the flow path of this system is provided in Appendix B. A 5000 psi supply of nitrogen gas was separated from the oxidizer feed system by the oxidizer pressurization valve PV-WFNA-01. Once open, the nitrogen was remotely regulated through the use of an ER3000SV-1 PID controller coupled to a Tescom Air Loaded Pressure Reducing Regulator, 26-2064T14A270. The regulator was made of 316 SS with a C_v of 0.06. A manual valve, MV-N2-02, was placed downstream of the regulator to isolate the system from the regulator when the system was placed under vacuum for oxidizer loading. A check valve was located downstream of the manual valve to ensure no nitric acid vapors traveled upstream to the regulator. A Swagelok pressure relief valve, SS-4R3A5, was set to 1500 psi and placed downstream of the check valve. A pneumatic vent valve, PV-WFNA-02, was placed upstream of the liquid oxidizer tank with the exhaust line running out of the building and up to the roof to ensure nitric acid vapors were vented out of the test cell. The oxidizer tank was a Swagelok 304 SS one gallon simple cylinder with a max pressure of 1800 psi. The main oxidizer valve, PV-WFNA-04, was placed downstream of the oxidizer tank, and a cavitating venturi was placed between the main valve and the oxidizer injector in order to regulate the oxidizer flow rate. The oxidizer fill valve, MV-WFNA-02, was placed between the oxidizer tank and main valve.

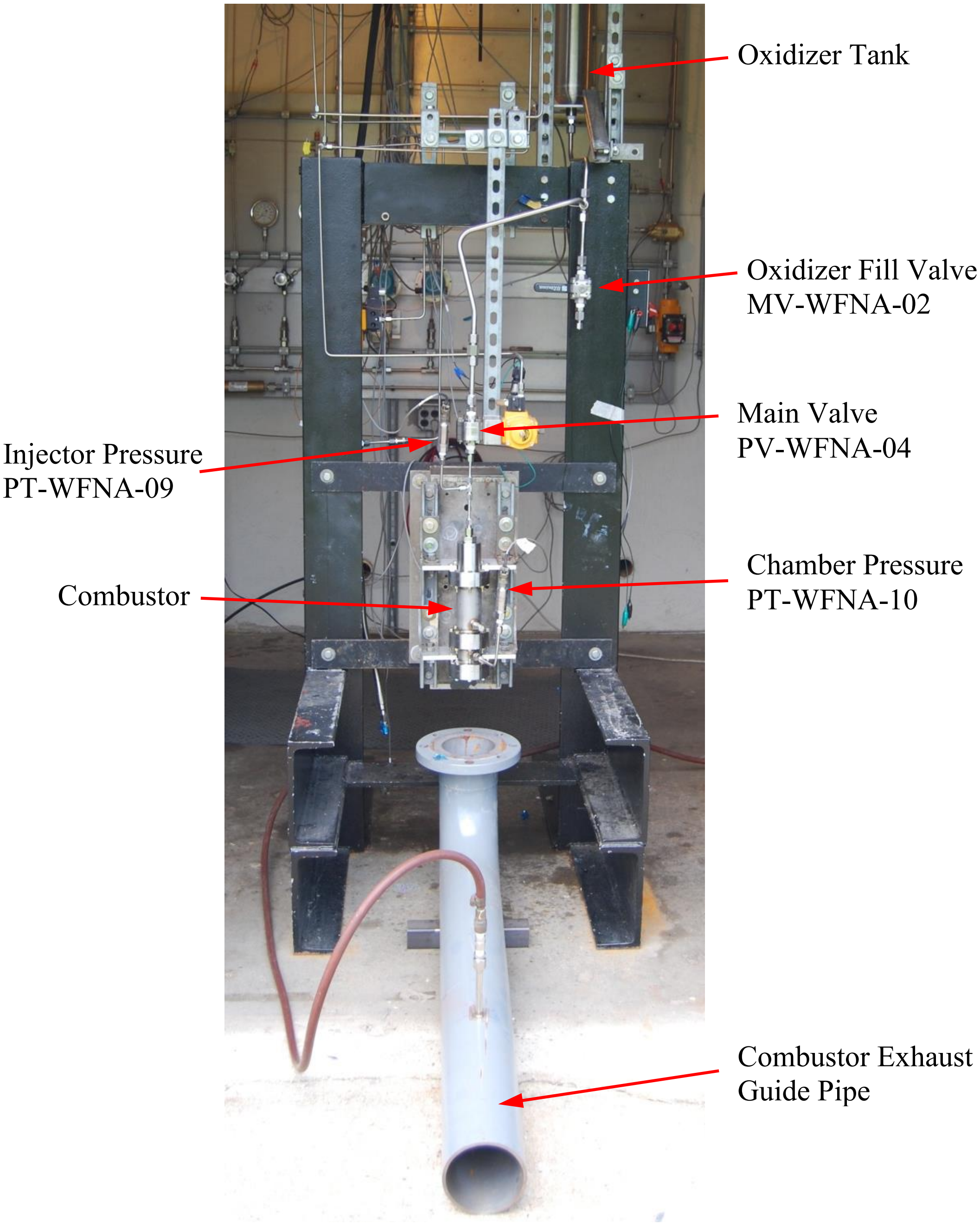

Figure 3.4 Hybrid rocket combustor plumbing and hardware.

Pressure and temperature measurements were made throughout the system to provide information on the operating conditions. A McDaniel Model SS (10,000 psi) pressure gauge was placed upstream of the oxidizer pressurization valve PV-WFNA-01 to provide a nitrogen supply pressure reading upon opening the nitrogen system main valve MV-N2-01. Another pressure gauge, McDaniel Model ES SS vacuum gauge, was placed between the vacuum generator and the vacuum system valve to measure the pressure during vacuum filling of the oxidizer. General Electric PMP 50E6 amplified pressure transducers were placed downstream of the oxidizer tank, upstream of the injector, and in the combustion chamber. A K type thermocouple was placed downstream of the oxidizer tank to make temperature measurements of the oxidizer for flow rate measurements.

The system was controlled and data was observed and recorded through a LabVIEW VI (virtual instrument) program interface coupled to a National Instruments DAQ (data acquisition) board. An image of the VI interface is provided in Appendix B. An automated routine was programed in the VI to operate the valves during combustor operation.

3.4.1 Combustor

The hybrid rocket combustor consisted of modular stainless steel sections of 3, 6, and 12 in long allowing for grain lengths of 3, 6, 9, or 12 in. A schematic of the combustor is provided in Figure 3.5. The oxidizer enters at the head end of the combustor through an injector providing a conical spray pattern. A phenolic liner provided a thermal barrier between the combustion chamber wall and the fuel grain. The fuel grain was recessed from the head end of the phenolic by ¼ in so that the face of the fuel grain was flush with the face of the oxidizer injector. High temperature RTV was placed on the head end face of the fuel grain to inhibit any reaction between the fuel and oxidizer upstream of the oxidizer injector orifice. A post combustion chamber was immediately downstream of the fuel grain and upstream of a graphite nozzle. The nozzle consisted of a converging section and a straight nozzle with no expansion section. The flanges were held together by eight ¼ 20 grade 8 bolts set to fail at a chamber pressure of 3028 psi while the nozzle retention plate used eight ¼ 20 grade 5 bolts set to fail at 2138 psi allowing for controlled depressurization in the case of an anomaly.

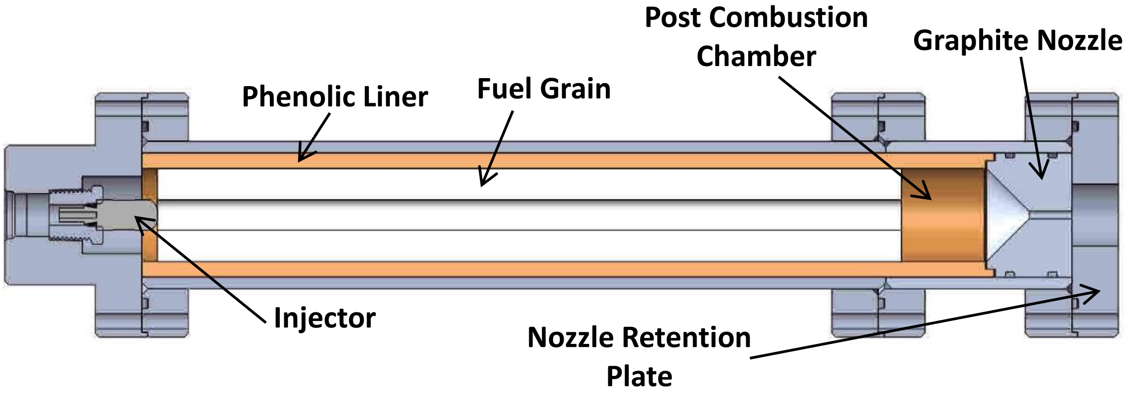

Figure 3.5 Hybrid rocket combustor schematic.

3.4.2 Oxidizer Injectors

The injectors used in the combustor tests are Spraying Systems Co. 1/8GG-316SS1, 1/8GG-316SS2, and 1/8GG-316SS3 full jet spray nozzles that will be hereafter identified as GG-1, GG-2, and GG-3 respectively. These injectors were tested with deionized water at pressure drops of 30-180 psi and their resulting spray patterns were visually observed. The spray angles from these tests were about 40°, 45°, and 70° for the pressure drops tested corresponding to GG-1, GG-2, and GG-3 respectively.

3.4.3 Hybrid Combustor Operation

The phenolic/fuel grain was inserted first and the bolts tightened according to specifications. To load oxidizer into the system, a vacuum generator system was attached to the nitrogen pressurization system upstream of the oxidizer tank. Nitrogen was flowed through a Vaccon JS-350 Venturi Vacuum Pump until the pressure in the oxidizer tank dropped to 2-4 psia at which point the MV-WFNA-1 valve was closed isolating the oxidizer system. The exhaust from the vacuum generator was also directed outside to ensure any nitric acid vapors exited the test cell. A tube was then inserted into a reservoir of nitric acid and valve MV-WFNA-2 was opened until the desired amount of oxidizer was suctioned into the oxidizer tank. The system pressure was then set by the ER3000 to the desired value for a specific flow rate at which point the system was ready for a live fire. Specific operating procedures are provided in Appendix C.

CHAPTER 4. SMALL SCALE EXPERIMENTAL RESULTS

4.1 Hypergolic Ignition

4.1.1 Powder Materials

In this work, various compounds were found to be hypergolic with WFNA, the results of which are tabulated in Table 4.1. These ignition delay times are similar to the ignition delays observed for other amine-boranes. The ignition delays of the three EDBB B, N,N-dimethylpiperazine borane, and ammonia borane powders are all very fast with ignition delays between 2-4 ms. These times are the fastest ever recorded for amine based fuels reacting with nitric acid based oxidizers. They are also some of the fastest ignition delays of any material ever used with times similar to the metal borohydrides yet without their air sensitivity and toxicity. The other amine-boranes all have relatively short ignition delays with the longest of 142.6 ms.

Table 4.1 Ignition delays of various amine-boranes and amines with WFNA as the oxidizer.

Fuel	Average Ignition Delay, ms	Standard Deviation	Particle Size, µm	No. of Tests
EDBB A	5.7	1.0	Dist.	7
EDBB B	2.9	0.3	Dist.	8
Ethylenediamine	166.7	111.3	-	3
Cyclohexylamine-borane	56.8	5.9	?	2
Cyclohexylamine-borane	78.7	20	45-150	
Cyclohexylamine	205.4	24.3	-	2
N,N-Dimethylpiperazine-bisborane	3.9	0.4	?	2
N,N-Dimethylpiperazine-bisborane	3.6	0.9	45-150	
Dimethylpiperazine	14.0	0.5	-	3
N-Methylpiperazine-bisborane	19.8	2.5	?	2
N-Methylpiperazine-bisborane	7.3	1.1	45-150	
N-Methylpiperazine	115.7	11.0	-	3
Tetramethylethylenediamin-bisborane	57.6	24.6	?	-
Tetramethylethylenediamine-bisborane	26.2	20.3	45-150	3
Tetramethylethylenediamine	16.2	0.3	-	3
Trimethylamine-borane	No Ignition	-	?	1
Trimethylamine	-	-	-	-
Piperazine-bisborane	15.4	-	?	1
Piperazine-bisborane	12.5	0.9	45-150	5
Piperazine	102.2	-	?	1
Piperazine	No Ignition	-	45-150	1
cis-2,6-dimethylpiperidine-borane	21.6	1.4	?	2
cis-2,6-dimethylpiperidine-borane	16.2	2.5	45-150	3
n-Propylamine-borane	64.2	62.8	?	2
n-Propylamine-borane	45.7	31.6	45-150	4
Piperidine-borane	107.4	20.1	?	2
Piperidine-borane	142.6	37.9	45-150	3
Ammonia Borane	2.1	0.4	?	3
Ammonia Borane	9.6	2.6	45-150	4
Ammonia Borane	8.6	1.6	<45	3
Ammonia	Not Hypergolic [62]	-	-	-

Sieving the material had a varied effect on ignition delay. Most often, the change in ignition delay is within the standard deviation of the measurement indicating no notable change due to sieving. This could be a result of the materials already having particle sizes near those tested before being sieved or that some other process other than surface area is the rate limiting step for these materials. However, a significant change was noted for ammonia borane. Three different ignition delay values are presented for the same material synthesized using the same procedures but resulting in values varying by an order of magnitude. This could be an indication of inconsistent particle morphology from batch to batch synthesis or possibly a difference in the concentration of the WFNA. We note that Gao and Shreeve did not report the concentration of WFNA used in their experiments [27], so this is an area that needs to be further investigated to elucidate what is the rate limiting ignition process for this material.

An example of a hypergolic ignition event between WFNA and EDBB B powder is depicted in Figure 4.1. A faint green light emission, indicative of ignition, is first observed 2.8 ms after the oxidizer droplet touches the EDBB powder. A light green flame envelops the powder and propagates outwards while an intense green flame is produced at the location of where the EDBB and WFNA first came in contact. The green flame is an indication of boron combustion and suggests that the borane groups on the EDBB molecule are the initial participants in the hypergolic reaction. As the reaction proceeds, yellow flames, characteristic of carbon combustion and soot formation, begin to appear near the edge of the green flame zone. The delayed appearance of the yellow luminosity may suggest that carbon does not directly participate in the ignition process, but may just indicate that soot is produced later. As the reaction continues, the green flame begins to fade while the yellow flame intensifies. The resulting flame ball continues to expand until it has expanded to occupy a volume nearly 40 times greater than its initial volume at which point the reaction ends.

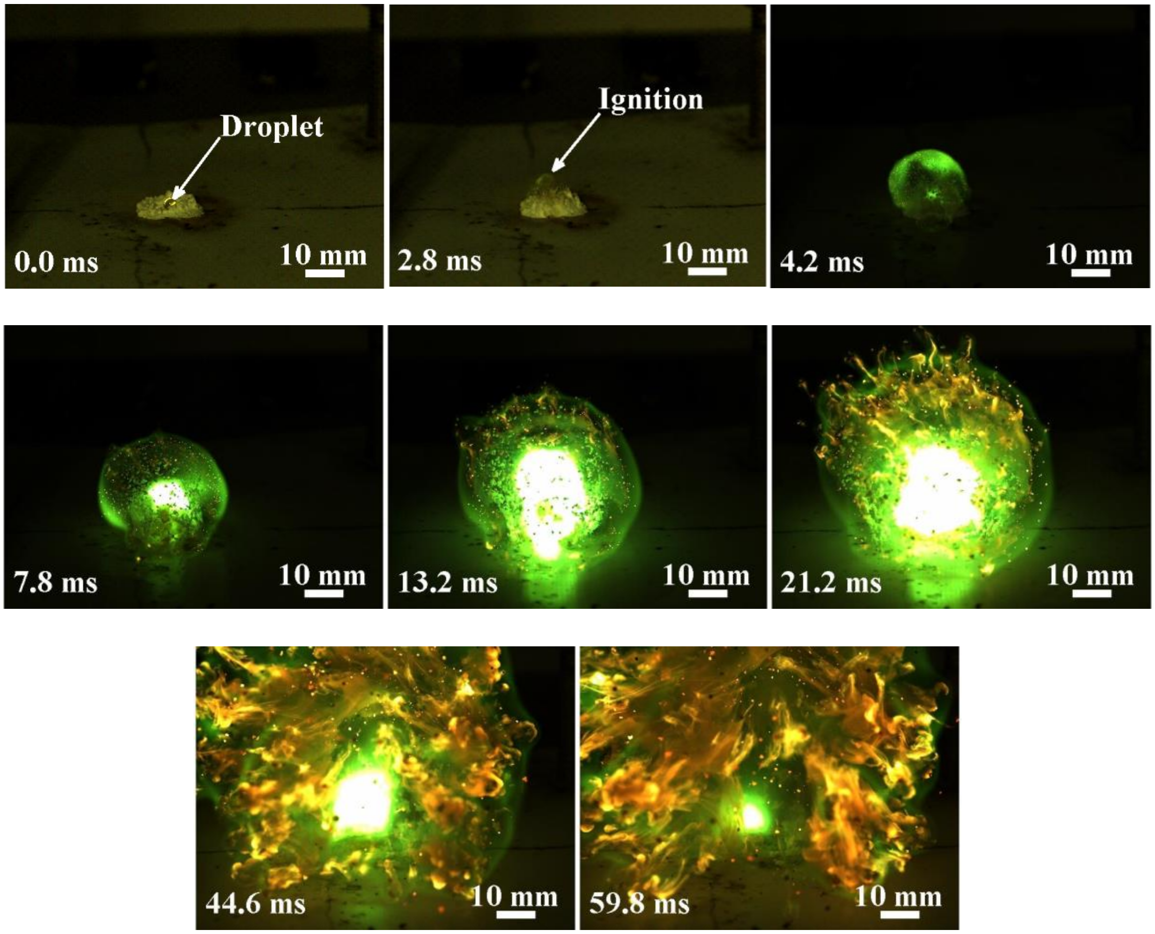

Figure 4.1 Hypergolic ignition of a droplet of WFNA with EDBB B powder.

The EDBB A powder exhibits similar ignition behavior to EDBB B but results in a longer ignition delay by a factor of two. This is a probably an effect of the EDBB B powder being an order of magnitude smaller than the EDBB A powder. Similar trends were observed by Bernard et al. that indicated smaller particle size resulted in shorter ignition delays [25].

Similar image sequences to that of EDBB B powder found in Figure 4.1 are provided in Figure 4.2 and Figure 4.3 that depict hypergolic ignition behavior of ammonia borane and N,N-dimethylpiperazine borane respectively. These two amine-boranes show similar ignition characteristics as the bright green flame dominates the early ignition process. Some yellow flames appear later in the ignition process of N,N-dimethylpiperazine borane, but green luminosity remains dominant. These trends further emphasize the importance of the borane group in the ignition process. Similar behavior is observed for all the other amine-boranes.

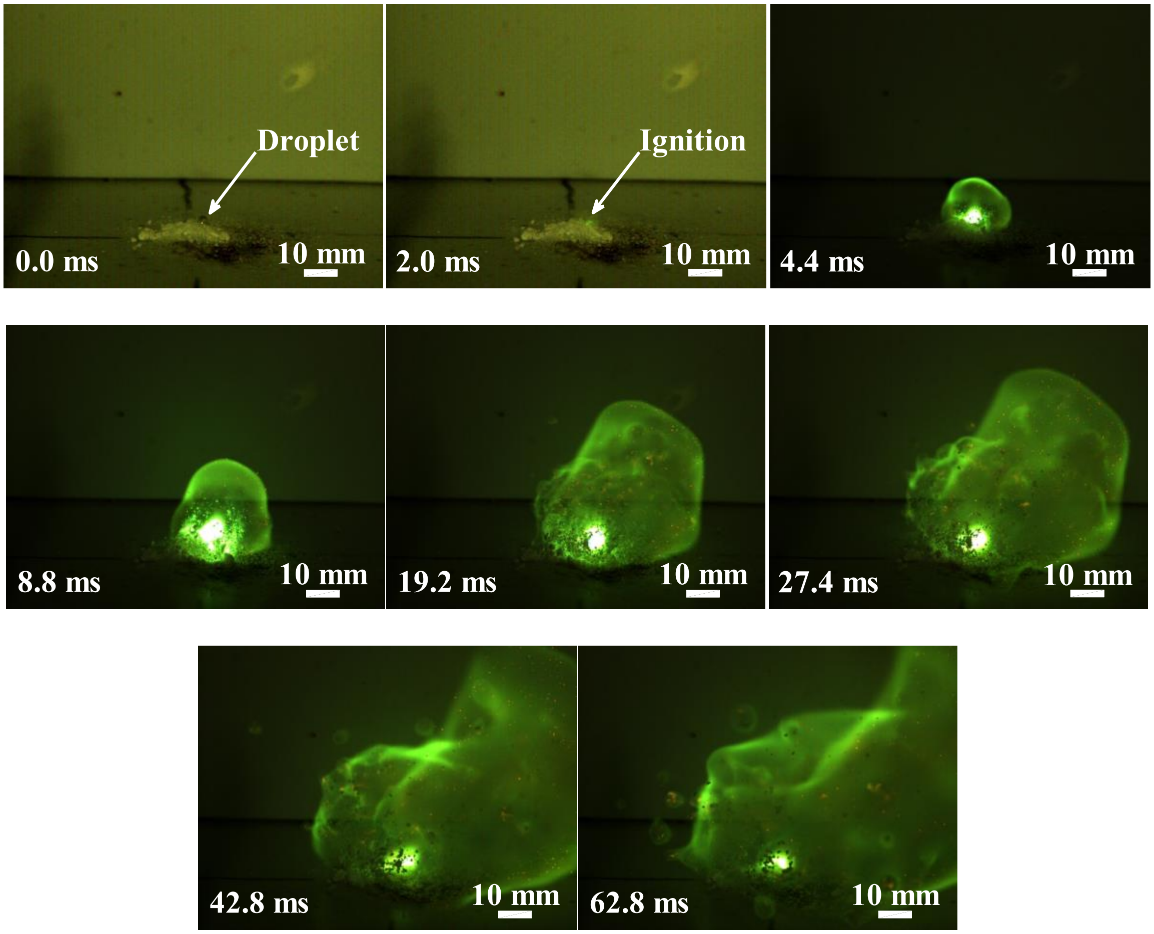

Figure 4.2 Hypergolic ignition of a droplet of WFNA with ammonia borane powder.

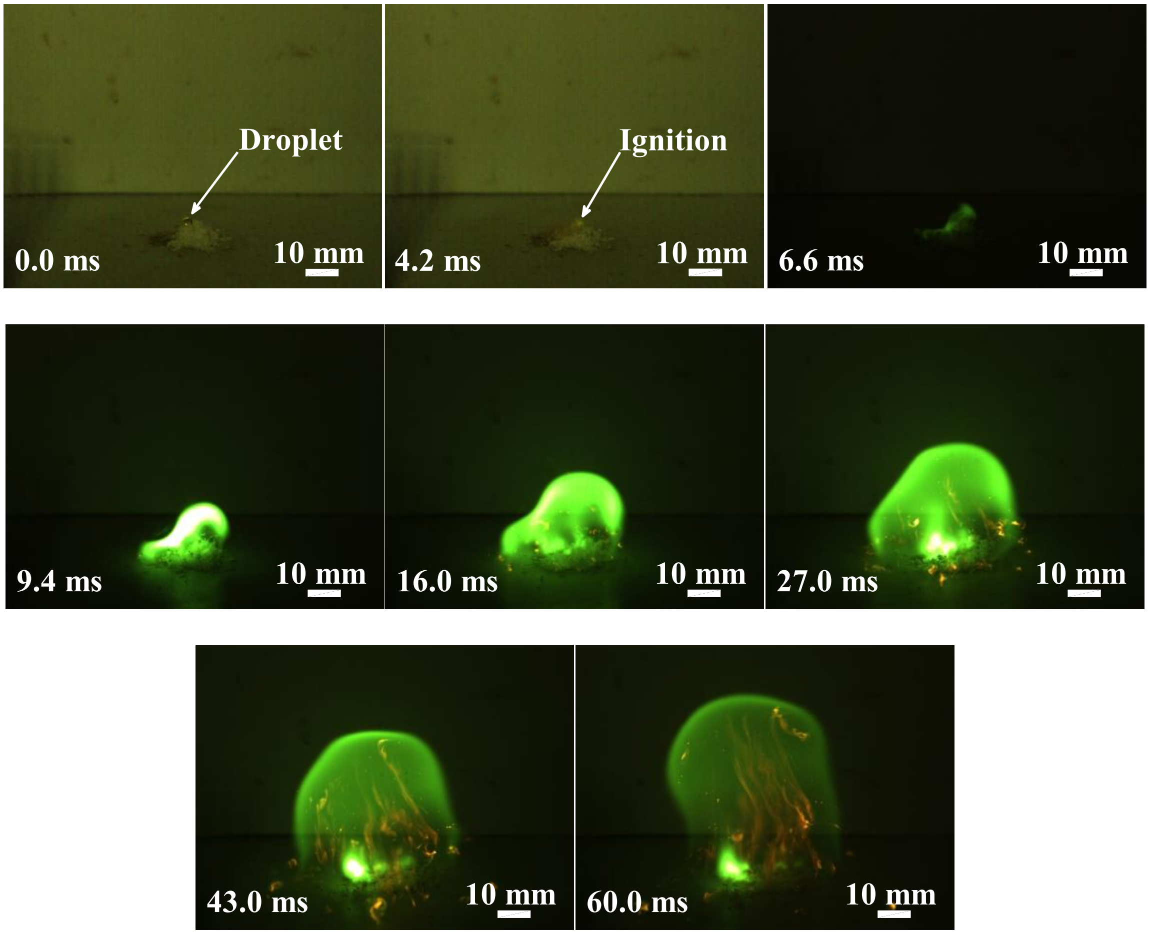

Figure 4.3 Hypergolic ignition of a droplet of WFNA with N,N-dimethylpiperazine borane powder.

The results in Table 4.1 indicate that the addition of the borane adduct to the amine results in making non hypergolic amines hypergolic or shorter ignition delays by a factor of 3.5-60 except for tetramethylethylenediamine. These trends are interesting but somewhat deceiving as most of the amines are liquids compared to solid amine-boranes. The phase differences probably has a significant influence on the ignition delay; however, how this effects the ignition delay is difficult to determine. Liquids require less energy to convert to gas phase and subsequent combustion but have low initial surface area. This surface area changes notably as the liquid oxidizer and liquid fuel interact and mix resulting in high surface area interactions that lead to more heat generation. On the other hand, solids require more energy to reach gas phase but have relatively high initial surface areas compared to liquids. The high surface area will lead to more heat generation initially compared to a liquid/liquid ignition until the physical time delay of mixing for liquid/liquid systems is overcome. The different dynamics controlling these systems make direct comparisons difficult; however, the magnitude of the reduction in ignition delay with the addition of a borane is notable.

Piperazine and piperazine borane are exceptions for which both materials are powders allowing for direct comparison. The addition of the borane adduct reduces the ignition delay of piperazine by a factor of 6.6 or causing a non-hypergolic fuel to become hypergolic if similar particle sizes are used. These trends further confirm the observation that the borane tends to promote hypergolic ignition with WFNA.

4.1.2 Amine-borane Ignition Mechanism

It is apparent that the addition of a borane to an amine tends to reduce the ignition delay. As this behavior has not been investigated in the past, there is no mechanism to describe this behavior. An initial conjecture of the mechanisms controlling the short ignition delays will thus be provided.

A borane molecule by itself is BH_3^+ with only six valence electrons. It thus acts as an acid and bonds with the amine that has two extra electrons, forming an amine-borane. When an amine-borane comes in contact with nitric acid, a strong acid, it will want to replace the borane and react with the amine. This initializes the traditional hypergolic reaction between the base amine and nitric acid. At the same time highly reactive pyrophoric borane gas is released to interact with a strong oxidizer. This provides two modes of heat release, the amine/nitric acid reaction and the borane/nitric acid oxidation, versus the one mode of heat release for a regular amine. The increased heat generation provides for an even faster amine-borane/nitric acid reaction producing large quantities of borane gas and heat resulting in borane ignition, resulting in a green flame as observed in the experiments in Section 4.1.1.

4.1.3 Fuel Pellets

Ethylenediamine-bisborane (EDBB) was incorporated into various fuel binders. Since all of the amine-boranes have the borane moiety, they should have similar incompatibilities with fuel binders as EDBB and were thus not studied with fuel binders.

The ignition delay times of EDBB combined with fuel binders are presented in Table 4.2. Two types of fuel sample surfaces were used including a surface cut using a razor blade and a sanded surface produce by using 100 grit sandpaper. There are various binder/amine-borane combinations that result in ignition delays under 10 ms. These ignition delays are the shortest ever recorded for amine based materials in a solid fuel matrix and are some of the shortest for any hypergolic hybrid oxidizer/fuel grain combination. The ignition delays of these air stable and low toxicity propellant combinations make hypergolic hybrids potentially feasible.

Table 4.2 Hypergolic ignition delay of EDBB B powder cast in or pressed with various fuel binders or additives with WFNA as the oxidizer.

% Binder or Additive	Surface	Ignition Delay, ms	Standard Deviation	Violent Reaction Delay, ms	Standard Deviation	No. of Tests
0%	Pressed	-	-	2.9	0.3	6
0%	Sanded	-	-	0	-	3
5% Ferrocene	Pressed	Inconsistent Ignition	-	3.1	0.4	3
10% Ferrocene	Pressed	8.2	2.5	2.8	0.2	3
15% Ferrocene	Pressed	39.1	9.3	3.1	0.3	3
42% HTPB	Cut	65.5	13.6	-	-	3
42% HTPB	Sanded	31.7	19.6	-	-	3
20% HTPB	Cut	10.1	2.0	-	-	3
18% R-45	Cut	15.8	2.8	-	-	2
18% R-45	Sanded	10.4	-	-	-	1
70% Epoxy	Sanded	88.0	36.6	-	-	3
50% Epoxy	Cut	9.4	3.2	-	-	3
50% Epoxy	Sanded	7.1	2.6	-	-	3
40% Epoxy	Cut	9.2	1.6	-	-	3
40% Epoxy	Sanded	3.3	0.5	-	-	3
30% Epoxy	Cut	22.8	1.4	-	-	2
30% Epoxy	Sanded	5.2	1.8	-	-	3
20% Epoxy	Cut	155.0	29.7	-	-	2
20% Epoxy	Sanded	9.4	3.0	-	-	4
50% RTV	Cut	12.5	1.2	-	-	3
50% RTV	Sanded	20.2	4.7	-	-	3
20% RTV	Cut	21.5	10.7	-	-	3
20% RTV	Sanded	6.9	0.4	-	-	3
70% Paraffin	Cut	111.1	8.9	-	-	3
70% Paraffin	Sanded	100.7	23.5	-	-	3
50% Paraffin	Cut	59.6	24.6	-	-	3
50% Paraffin	Sanded	53.0	6.7	-	-	3

The implemented binder had a measureable impact on the ignition delay. Paraffin and HTPB appear to be the least favorable binders for hypergolic ignition as they produced ignition delays all above 30 ms except for 80 wt.% EDBB/20 wt.% HTPB. Epoxy and RTV silicone binders resulted in similar ignition delays with epoxy generally having somewhat shorter delays. Comparing the same amount of binder in the fuel pellet provides the most unambiguous performance comparison. At 50 wt.% binder (42 wt.% for HTPB) and a cut surface, epoxy has an ignition delay of 9.4 ms, RTV is 12.5 ms, paraffin is 59.6 ms, and HTPB is 65.5 ms. The notable difference in ignition delays between the epoxy and RTV binders versus the paraffin is probably due to the lack of rigidity and structural integrity of paraffin allowing it coat to the surface of the amine-borane upon cutting or sanding and thus not exposing the amine-borane to the oxidizing environment. The HTPB based binder system could be producing a similar effect as it appears not to completely cure. The HTPB could also be partially reacting with some of the EDBB, reducing the amount of hypergolic material in the fuel pellet. Overall, RTV or epoxy based binders appear to be the best candidates for producing short ignition delay amine-borane/binder fuel matrices.

The surface type of the pellet (cut or sanded) made a notable impact on ignition delays decreasing the ignition delay by as much as a factor of 16.5 when going from a cut surface to a sanded surface except for the 50% EDBB/50% RTV pellet. Images of the surface, 2D and 3D, of both cut and sanded 80% EDBB/20% RTV fuel pellets are provided in Figure 4.4 and Figure 4.5 respectively. The 2D images indicate that much more EDBB crystals are exposed upon sanding the surface. The 3D images indicate that neither of the surfaces are flat but have surface features. The depth of these surface features are up to 72 μm for a cut and 124 μm for a sanded surface. It is therefore likely that sanding the surface tends to remove the binder exposing more EDBB crystals while increasing the magnitude of depth of the surface features. Both of these outcomes will result in effectively creating more surface area and thus more reaction and higher heat generation for a given area. It is also likely that reaction between the fuel and oxidizer can be partially confined in the deep surface features of the sanded pellet allowing for local pressurization. Higher pressures will lead to faster reaction kinetics. The combination of these results is likely the reason why sanded surfaces tend to ignite faster than cut surfaces.

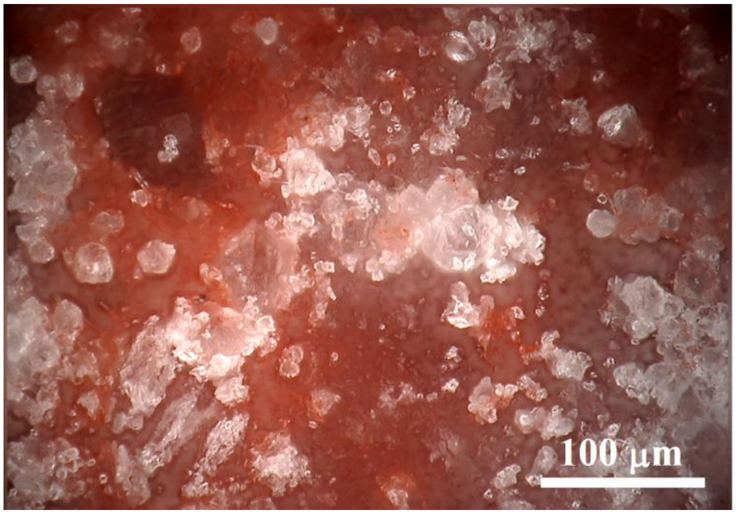

(a)

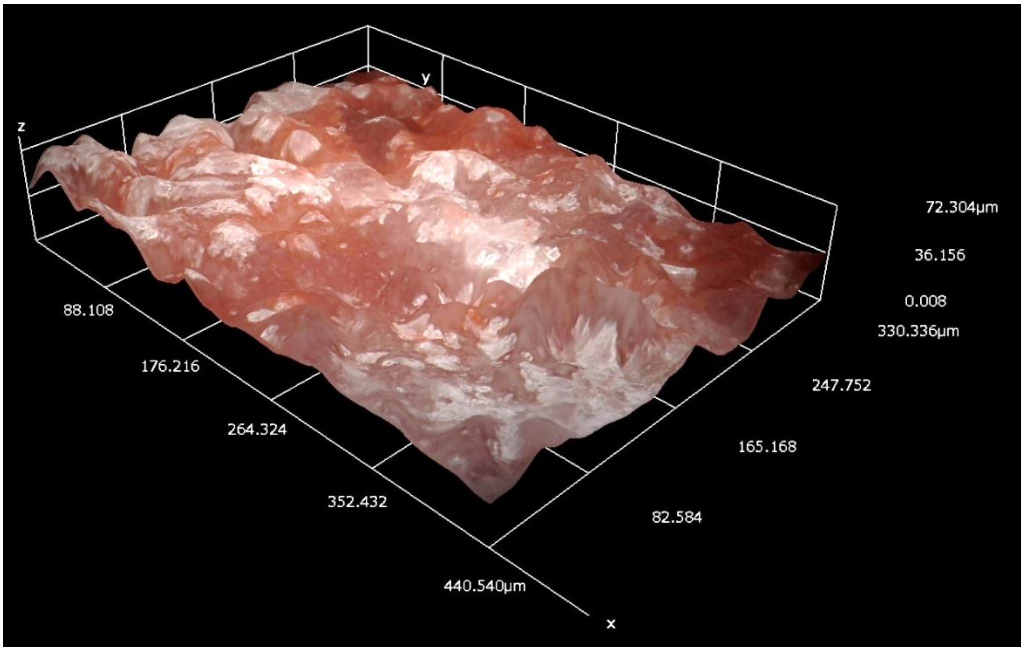

(b)

Figure 4.4 Hirox images of an 80% EDBB/20% RTV pellet with a cut surface in 2D (a) and 3D (b).

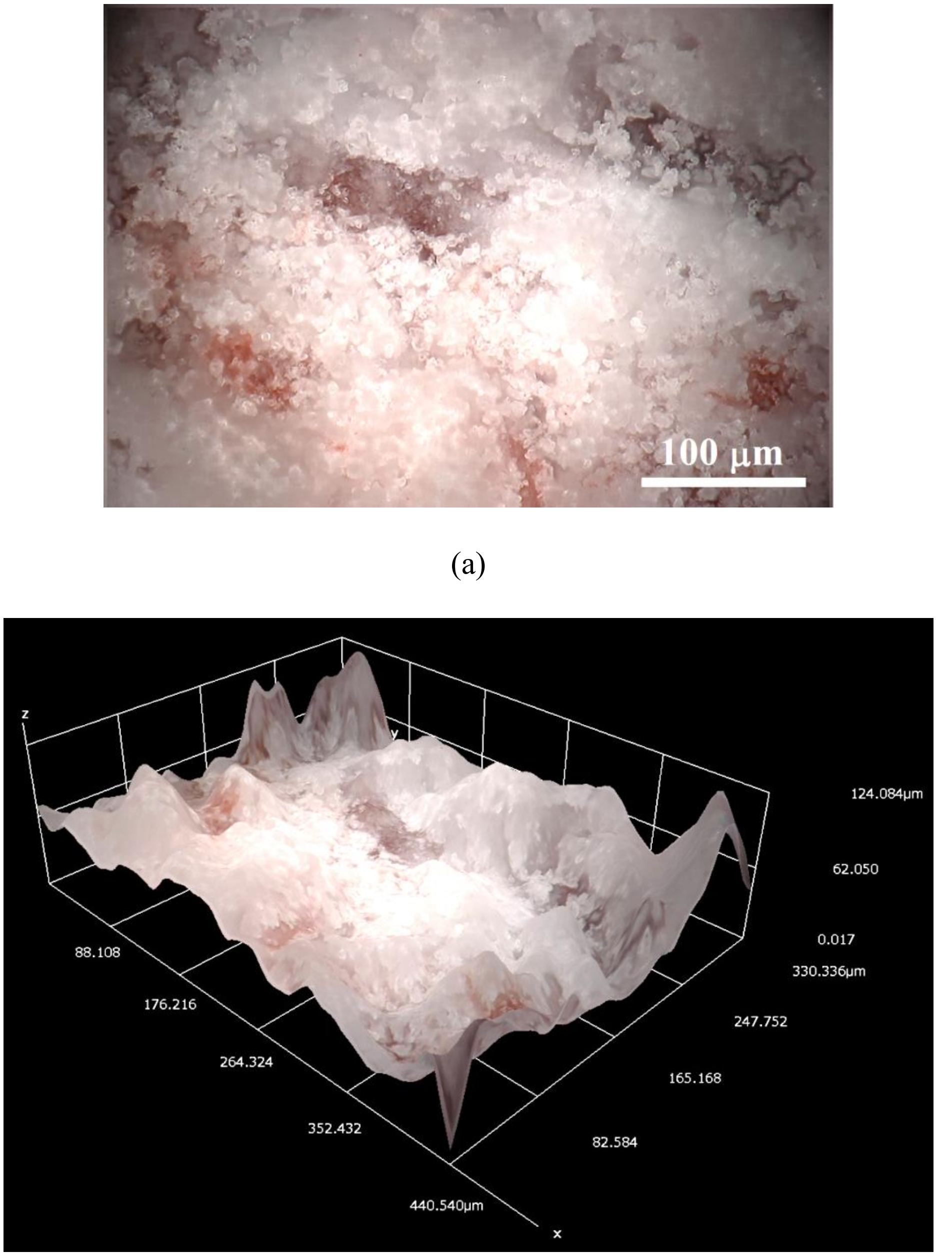

(a)

(b)

Figure 4.5 Hirox images of an 80% EDBB/20% RTV pellet with a sanded surface in 2D (a) and 3D (b).

Pressed EDBB B fuel pellets exhibit fast, violent reactions when exposed to a WFNA droplet. The droplet first impacts the fuel pellet and spreads out across the surface of the pellet, Figure 4.6. A reaction between the WFNA and EDBB pellet appears to commence upon contact resulting in bubbling of the oxidizer. Eventually, a point is reached when the reaction rate increases notably producing large quantities of gaseous products between the liquid oxidizer and solid fuel. This results in expulsion of the liquid WFNA from the pellet surface and quenching of the reaction (noted as a violent reaction in Table 4.2) beginning 2.9 ± 0.3 ms after the WFNA droplet encountered the fuel pellet. It is likely that this pressure rise is a result of ignition between the solid fuel and liquid oxidizer layers, as the violent reaction time is the same as the ignition delay time of the powder samples. The rapid depressurization caused by the expulsion of the oxidizer from the fuel surface would then cause the reaction to quench. Any subsequent ignition of the fuel pellet was caused by oxidizer falling back onto the fuel pellet. These ignition dynamics will probably result in short ignition delays in an actual rocket motor as oxidizer will be continuously coming in contact with the fuel surface.

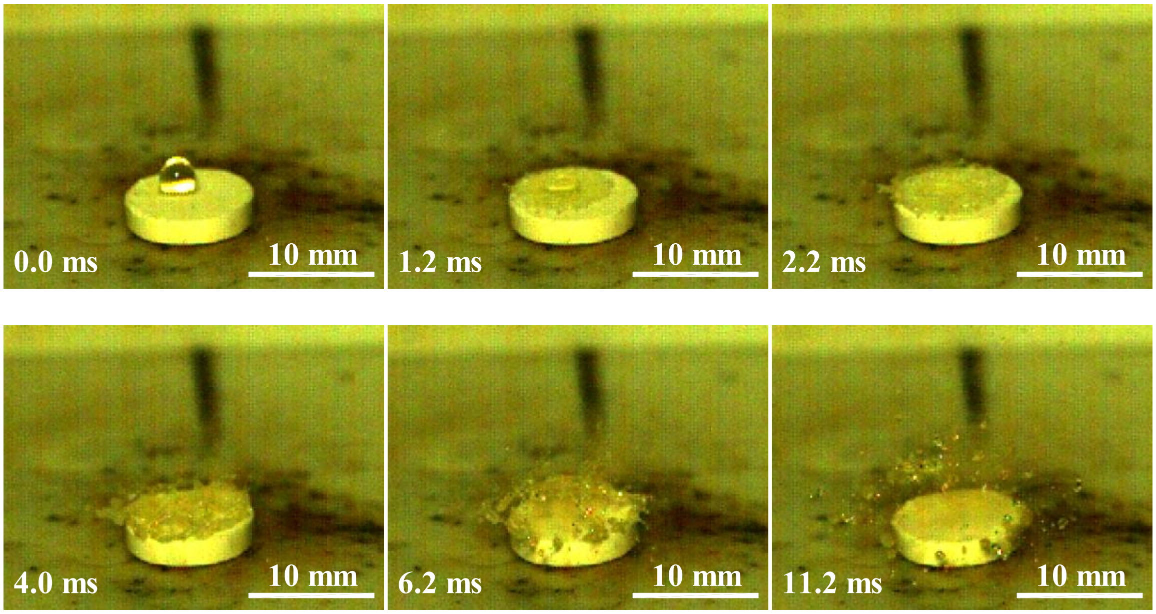

Figure 4.6 Heterogeneous reaction between WFNA and pressed EDBB fuel pellets resulting in shattering of the droplet an expulsion of the oxidizer from the fuel pellet.

Hypergolic ignition experiments were also performed with pressed EDBB pellets that were sanded to create a rough surface. These fuel pellets exhibit similar ignition behavior to that of the un-sanded pellets except the gas production leading to expulsion of the oxidizer from the fuel surface appears to occur almost immediately upon contact. Localized ignition events also occur in the gases surrounding the fuel pellet; presumably decomposed EDBB and possibly EDBB fuel particles are expelled from the fuel pellet that continue to react with the oxidizer. Again, more reaction leading to ignition occurs if any of the expelled oxidizer falls back onto the fuel pellet.

Pressed EDBB/ferrocene pellets exhibit similar behavior to the pressed EDBB pellets resulting in a violent reaction occurring 2.8-3.1 ms after contact with the oxidizer. The difference is that these pellets with ferrocene tend to ignite with ignition delays as fast as 8.2 ms and then continue to burn, whereas the 100% EDBB pellets do not ignite unless oxidizer happens to fall back on the pellet. A yellow flame, in conjunction with the typical green flame of EDBB, is also usually observed upon ignition suggesting that ferrocene is contributing to the ignition event; the ignition times and behavior would also support this conclusion.

The 58% EDBB/42% HTPB composite is hypergolic with WFNA. Upon contact, the WFNA droplet spreads over the fuel pellet surface and begins to react, see Figure 4.7. The reaction results in a reddish brown gas being produced between the liquid and fuel pellet that diffuses or bubbles through the liquid oxidizer and away from the fuel. Ignition is eventually achieved near the fuel pellet in the gas phase resulting in a bright green flame that remains until all of the WFNA has reacted. Once the WFNA is consumed, the fuel pellet continues to burn with the surrounding air until quenched. This behavior is similar for both cut and sanded surfaces but occurs on different time scales resulting in different ignition delays.

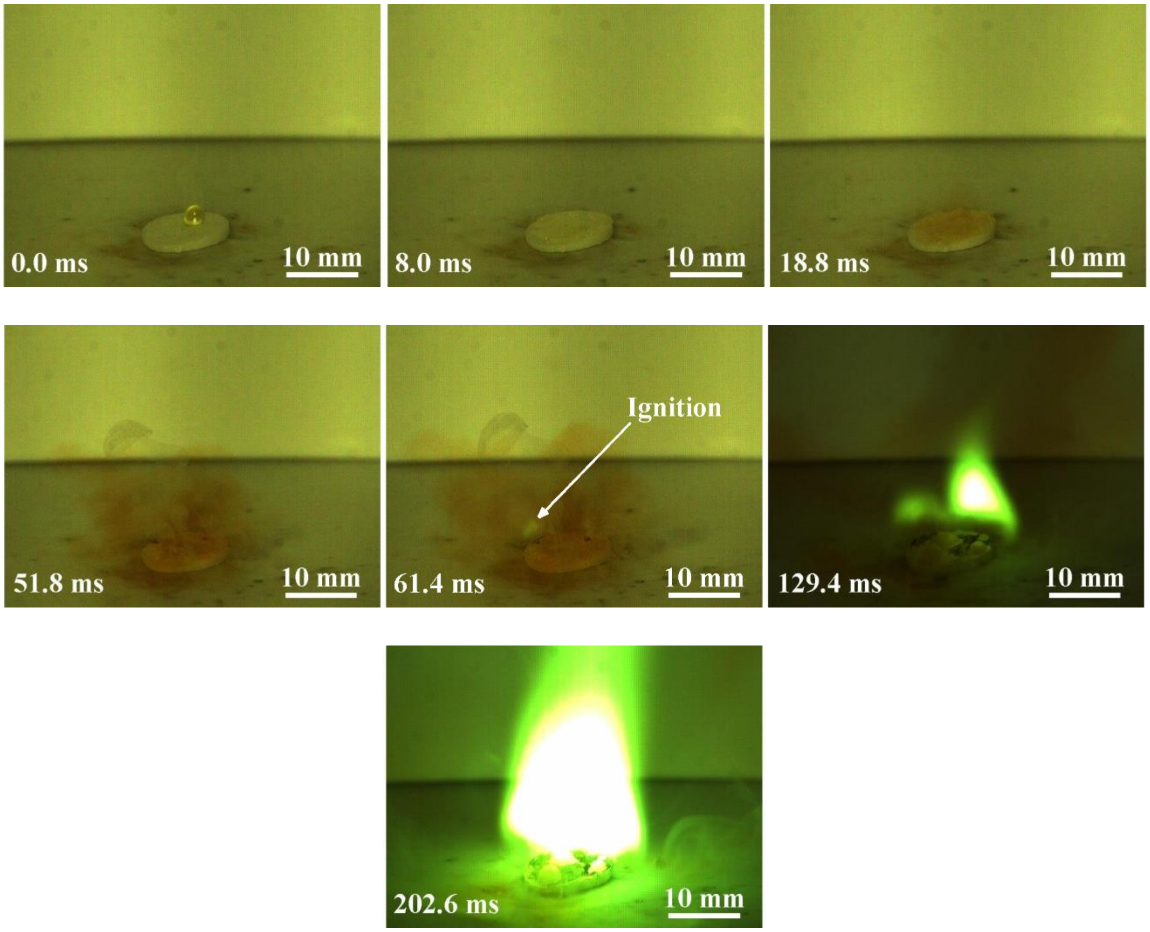

Figure 4.7 Hypergolic ignition and subsequent combustion of 58% EDBB/42% HTPB with WFNA.

Upon contact with the 80% EDBB/20% HTPB pressed pellets, the oxidizer tends to spread out across the surface of the pellet and gas generation occurs forcing the oxidizer to be expelled from the surface in a similar fashion to that of pressed 100% EDBB pellets. Ignition occurs during this expulsion process as green flame appears in the gas phase between the leaving liquid oxidizer and the fuel pellet. Such behavior further suggests that an event similar to ignition is occurring between the fuel and oxidizer for the 100% EDBB pellets. The green flame rapidly engulfs the entire fuel pellet that continues to burn with air once the WFNA is consumed.

The R-45 based fuel pellets exhibit similar ignition behavior to that of the 80% EDBB/20% HTPB pressed pellets.

Three different types of hypergolic ignition behaviors were noted for the remaining EDBB/binder combinations. The first behavior consisted of those fuel pellets/oxidizer droplets that have ignition delays under 10 ms. These tend to generate gas upon contact between the fuel and oxidizer. As the WFNA spreads out across the fuel pellet, surface gas generation begins to force the WFNA away from the fuel surface. Ignition generally occurs near the interface between the fuel pellet and oxidizer close to the edge of the pellet. The green flame then propagates towards the center of the fuel pellet between the oxidizer and fuel causing the oxidizer to continue to leave the fuel surface. Once ignited, the EDBB/binder pellets continue to burn with the surrounding air, see Figure 4.8.

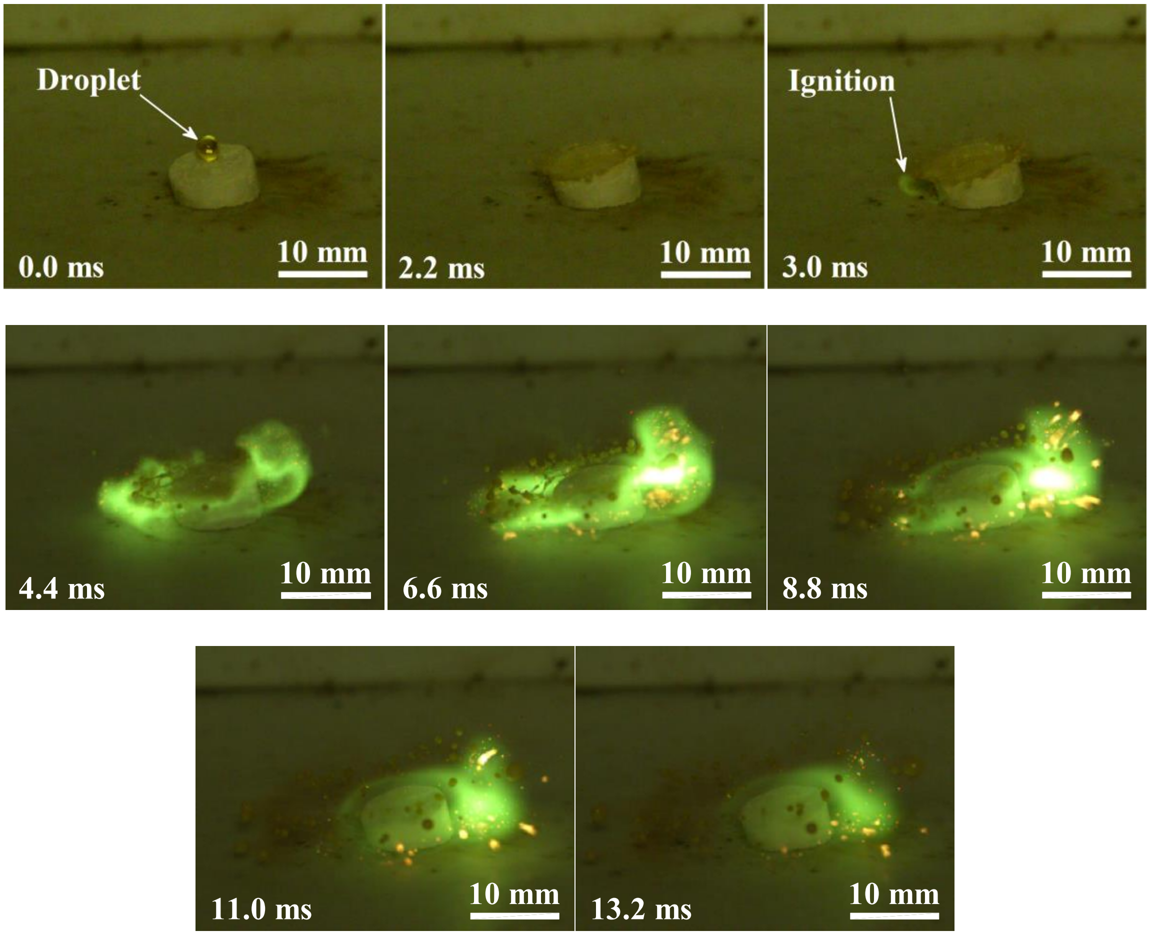

Figure 4.8. Hypergolic ignition of a 60% EDBB/40 epoxy pellet with a sanded surface and WFNA as the oxidizer.

A second ignition behavior was observed for EDBB/binder fuel pellets that had ignition delays longer than 10 ms. As the oxidizer contacts the surface, gas generation occurs resulting in some of the oxidizer being expelled from the surface. Most of the oxidizer remains on the surface and forms balls of oxidizer while reddish brown gas is produced. Ignition generally occurs near these balls of oxidizer in what appears to be the gas phase just as a green flame develops.

A third ignition behavior was observed for 50% EDBB/50% RTV pellets with a cut surface. As the oxidizer contacts the surface, it spreads out and gas generation occurs similar to other fuels. At this point the gas generation between the fuel and oxidizer causes the oxidizer to form a dome shape. As this dome bursts, reddish brown gas is expelled upwards and subsequent ignition occurs in this expelled gas resulting in a green flame that envelops the fuel pellet, see Figure 4.9.

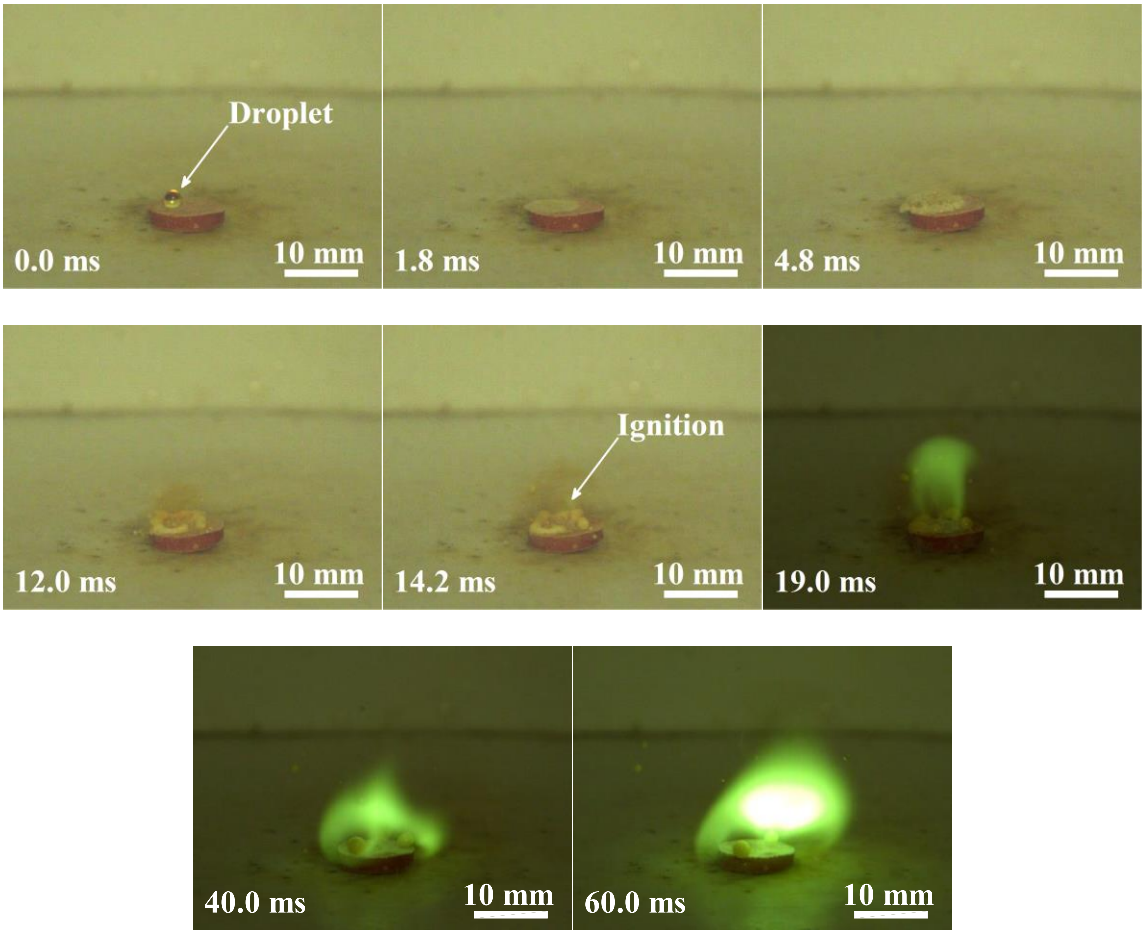

Figure 4.9 Hypergolic ignition of a 50% EDBB/50% RTV pellet with a cut surface and WFNA as the oxidizer

The ignition delay of the EDBB/binder fuel combinations is compared against other hypergolic combinations that have been tested in hybrid motors and that used nitric acid based oxidizers in Table 4.3. The current formulations have faster ignition delay times than all of the motor tested combinations except for Sagaform A. As mentioned in Section 1.2, it is suspected that Sagaform A is an air unstable fuel. Therefore, for air stable nitric acid based hypergolic propellant combinations, EDBB combinations have the shortest ignition delays and thus probably the fastest response times in a combustor system.

Table 4.3 Ignition delays of various hypergolic oxidizer/fuel combinations from this study compared against ignition delays of hypergolic combinations that have been used in hybrid motor tests.

Fuel Type	Oxidizer	Ignition Delay, ms
90% EDBB B Powder/10% Ferrocene	WFNA	8.2
80% EDBB B Powder/20% HTPB	WFNA	10.1
60% EDBB B Powder/40% Epoxy	WFNA	3.3
80% EDBB B Powder/20% RTV	WFNA	6.9
Tagaform [2, 4]	WFNA	150
Sagaform A [5]	IRFNA	5
p-Toluidine/p-Aminophenol [4]	WFNA	110
Metatoluene Diamine/Nylon	RFNA	-
Difurfurylidene Cyclohexanone [14, 16, 78]	RFNA	45, 60-70, 255
Aniline Formaldehyde [19]	99% RFNA/1% Ammonium Vanadate	4800
50% Aniline Formaldehyde/50% Magnesium [20]	RFNA	1134

4.2 Intrinsic Properties

Various measured intrinsic properties of the amine-boranes are presented in Table 4.4. Densities of the amine-boranes were measured 10 times each with an AccuPyc II 1340 Pycnometer using ASTM standard B923 [71] and typically ranged between 0.8-1.0 g/cm^3. The density of EDBB was found to be 0.8317 ± 0.0004 g/cm^3, a value very similar to the value reported by Groshens and Hollins of 0.82 g/cm^3 [79].

Two values of heat of combustion are presented in Table 4.4, one from pellet and one from powder sample measurement methods (discussed in Section 3.2). Both measurement methods were performed three times for each material investigated. The analysis of the measurements provide two values for the lower limit of the heat of formation, while the upper limit was found using the heat of combustion of the pellet measurement in conjunction with Eqns. 3.3 and 3.4. The measurements that used powder for the heat of combustion were only performed on materials that had a notable amount of boron in the amine-borane (over 20 wt.% boron) that could significantly influence the lower limit of the heat of formation.

Table 4.4 Measured intrinsic properties of various amine-boranes.

Fuel	Density, g/cm^3	Heat of Combustion, kJ/mol		Heat of Formation, kJ/mol		
				Lower Limit		Upper Limit
		Pellet	Powder	Pellet	Powder	Pellet
EDBB	0.8317 ± 0.0004	3651.9 ± 9.5	3747.8 ± 33.5	-445.6	-349.7	-145.9
Cyclohexylamine-borane	0.9270 ± 0.0006	4948.2 ± 6.7	-	-348.7	-	-198.9
N,N-Dimethylpiperazine-bisborane	0.9859 ± 0.0005	6165.1 ± 5.4	-	-360.2	-	-60.4
N-Methylpiperazine-bisborane	0.9824 ± 0.0008	5402.0 ± 18.9	-	-445.2	-	-145.5
cis-2,6-dimethylpiperidine-borane	0.9319 ± 0.0008	5460.3 ± 11.6	-	-514.7	-	-364.8
n-Propylamine-borane	0.8093 ± 0.0004	3236.5 ± 20.7	-	-310.7	-	-160.8
Piperidine-borane	0.9189 ± 0.0004	4356.5 ± 8.8	-	-262.3	-	-112.5
Ammonia Borane	0.7799 [80]	1296.2 ± 2.3	1322.6 ± 5.9	-216.7	-190.4	-66.9

The intrinsic properties presented in Table 4.4 have not been reported in the literature for these materials; however, several studies have been performed to theoretically predict densities and heats of formation of some of these materials allowing for comparison. The densities measured are relatively close to that predicted by McQuaid and Chen [81]. They calculated the density of piperidine-borane and N,N-dimethylpiperazine-bisborane to be 0.97 and 0.99 g/cm3 respectively. They also predicted the heats of formation of these materials to be -186.6 and 175.7 kJ/mol respectively. It is suspected that it was a typo to not include a negative sign for the 175.7 value in their report as this would be quite high. Assuming that typo, both of these predicted values fall within the range of measured heats of formation and are near the upper range. The heat of formation of ammonia borane has been theoretically calculated by several researchers giving values of -61.1 [82] and -73.3 kJ/mol [83]. These values are very close to the upper limit of that found for ammonia borane. The fact that the measured upper limit values for these three materials are closer to those calculated theoretically suggests that the actual heats of formation for these amine-boranes is perhaps closer to the upper limit of the data presented in Table 4.4.

4.3 Theoretical Performance

The theoretical performances of the amine-boranes compared against their base amines are presented in Table 4.5. Calculations were performed using Cheetah 6.0 [72]. The addition of the borane to the amine tends to maintain I_{sp} and ρI_{sp} values for the lower performance limit, while the upper performance limit indicates that complexation with borane improves I_{sp} and ρI_{sp} indicating that borane addition is beneficial for improving performance of the base amines.

Table 4.5 Theoretical performance for various amines and their corresponding amine-boranes. Theoretical I_{sp} and ρI_{sp} values calculated using IRFNA IIIA [84] as the oxidizer, 6.89 MPa chamber pressure, and perfectly expanded to atmospheric pressure. Values for MMH/IRFNA and MMH/NTO are provided as a reference.

Fuel	Lower Limit			Upper Limit			ΔH_f Ref.
	O/F	I_{sp}, s	ρI_{sp}, sg/cm3	O/F	I_{sp}, s	ρI_{sp}, sg/cm3	
EDBB	3.8	266.8	350.4	3.6	274.7	358.5	Measured
Ethylenediamine	-	-	-	3.2	264.9	350.2	[7]
Cyclohexylamine-borane	4.5	262.2	362.9	4.5	266.1	367.5	Measured
Cyclohexylamine	-	-	-	4.5	262.9	355.9	[7]
N,N-Dimethylpiperazine-bisborane	4.0	265.4	370.5	4.0	271.9	378.2	Measured
N,N-Dimethylpiperazine	-	-	-	4.0	265.4	378.6	[7]
N-Methylpiperazine-bisborane	4.0	262.9	366.7	3.9	270.3	374.8	Measured
N-Methylpiperazine	-	-	-	-	-	-	-
cis-2,6-dimethylpiperidine-borane	4.7	259.3	360.0	4.6	262.6	363.9	Measured
cis-2,6-dimethylpiperidine	-	-	-	4.5	263.5	350.9	[85]
n-Propylamine-borane	4.5	263.6	350.3	4.3	269.7	356.5	Measured
Propylamine	-	-	-	4.3	265.5	337.9	[7]
Piperidine-borane	4.5	263.8	363.5	4.3	268.3	368.1	Measured
Piperidine	-	-	-	4.3	264.0	355.7	[7]
Ammonia Borane	1.5-3.5	269.0-271.3	301.5-341.9	0.9-3.5	283.0-300.3	306.3-359.7	Measured
Ammonia	-	-	-	2.2	264.1	0.6	[7]
MMH	-	-	-	2.6	274.6	350.3	[72]
MMH/NTO	-	-	-	2.2	288.4	344.2	[72]

Interestingly, amine-boranes with a relatively high wt.% of boron tend to exhibit two peaks in I_{sp} performance compared to the typical one performance peak. This behavior is depicted in Figure 4.10 for both EDBB and ammonia borane and is the reason why ammonia borane has a range of performance values listed in Table 4.5. The first performance peak is a result of complete boron oxidization with the combination of very low molecular weight products (predominantly H_2), while the second peak is caused by the complete oxidation of boron and H_2. This behavior is not only possible with the neat amine-boranes but is also observed when mixed with a fuel binder as will be discussed in the following sections.

There are several advantages to using fuels with this unique double peak performance behavior. Such fuels can operate notably fuel rich while maintaining or increasing performance. This can be advantageous for systems that require lower combustion temperatures due to material constraints resulting in fuel rich operation while still achieving high performance. Fast response attitude control systems could benefit from the double peak as this would allow for high performance throughout the transient ignition, sustainment, and shutdown process. Currently such systems suffer a performance loss due to these transients in part to the O/F shift upon ignition and shutdown. The double peak performance behavior is also specifically advantageous for hybrid rocket systems that typically undergo O/F shifts during normal operation or throttling. Thus, motors could be designed such that reasonably high I_{sp} values are maintained throughout all operation phases. These advantages make the amine-borane performance profiles more desirable compared to typical fuels that tend to only exhibit one performance peak.

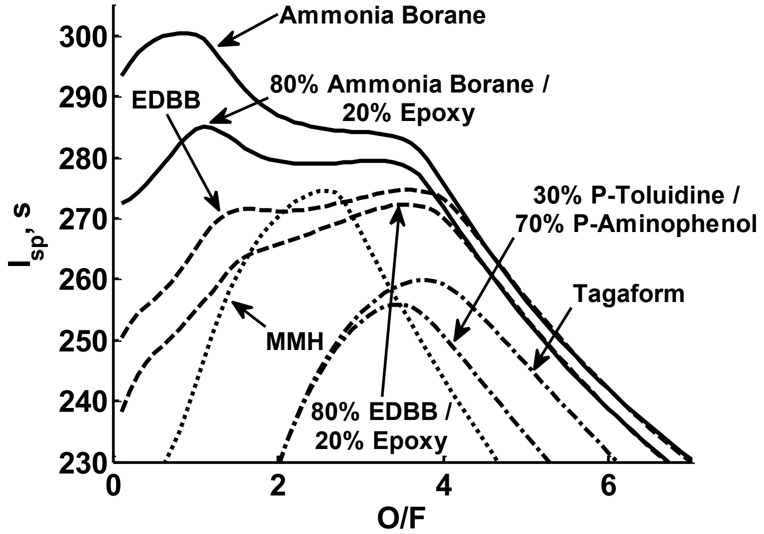

Figure 4.10 I_{sp} of various hypergolic fuels reacted with IRFNA IIIA versus O/F ratio.

Theoretical combustion product species in the combustion chamber and the exhaust of only EDBB are provided in Figure 4.11. Products are all in the gas phase for O/F values greater than 2.1. This is encouraging for internal flow in the motor as there should not be any two phase flow loses. Of particular interest are the exhaust products as condensed phase products will result in smoke in the exhaust; smoke is not preferred for military applications. Between and O/F of 3.8 to 4.8, the exhaust products of EDBB are all in gaseous phase providing an acceptable range of O/F values for min smoke applications; however, it is difficult to determine if condensed phase products will not be formed behind the rocket without performing flight tests.

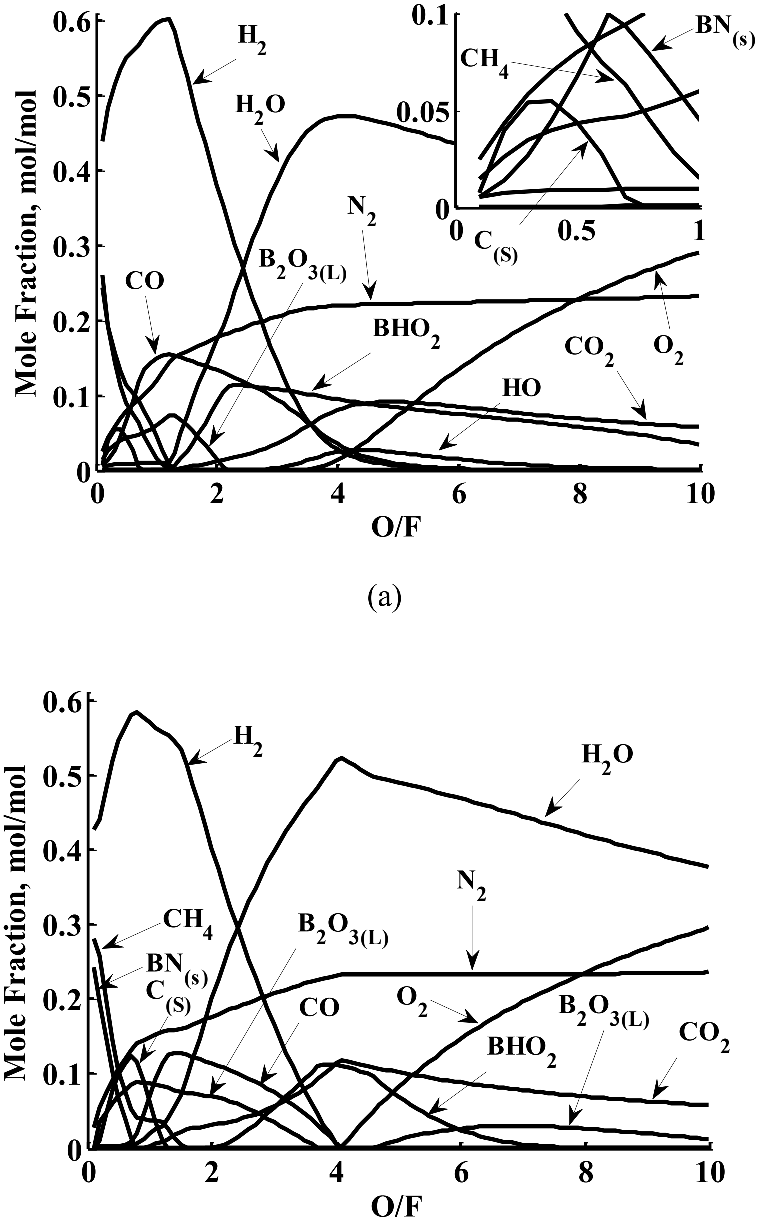

(a)

(b)

Figure 4.11 Theoretical product species vs. O/F ratio in (a) the combustion chamber and (b) the exhaust for EDBB and IRFNA IIIA combusted at a chamber pressure of 6.89 MPa, perfectly expanded to atmospheric conditions, and using shifting equilibrium.

4.4 Comparison with Other Fuels

4.4.1 Solid Hybrid Hypergolic Fuels

The theoretical performance values of the higher performing amine-boranes (using the upper limit of the ΔH_f) mixed with a feasible fuel binder are provided in Table 4.6 along with other hypergolic fuels. Compared to hypergolic hybrids using similar oxidizers, the amine-borane based fuels have notably higher theoretical I_{sp} values by 4-11%. Not only are higher performance values attainable by using the amine-borane based fuels, but a much wider range of O/F values can be implemented to obtain high performance, see Figure 4.10, providing the advantages discussed in Section 4.3. Theoretical ρI_{sp} values range from a 17% decrease to a 5% increase when compared to other hypergolic hybrdis, depending on the fuel and operating conditions selected. The ρI_{sp} values are typically less important than the I_{sp} values except where volume becomes a significant factor, such as for small motors or attitude control systems. Such volume constrained systems typically require a fast response system, something not feasible with previously tested hypergolic hybrids except for those using toxic and unstable additives. The amine-borane based fuels provide fast response times, producing ignition delays an order of magnitude faster than those hypergolic hybrids shown in Table 4.6. Thus, amine-borane based fuels have the opportunity to improve performance, lower ignition delay, and reduce toxicity of the available hypergolic hybrids fuels.

Table 4.6 Comparison of performance values of other hypergolic fuels versus solid amine-boranes/fuel binder. Theoretical I_{sp} and ρI_{sp} values calculated using IRFNA IIIA as the oxidizer, 6.89 MPa chamber pressure, and perfectly expanded to atmospheric pressure

Fuel	Ignition Delay with WFNA, ms	O/F	I_{sp}, s	ρI_{sp}, sg/cm^3	ΔH_f Ref.
80% EDBB / 20% Epoxy	9.4	3.6	272.3	362.9	Measured / [72]
80% N,N-Dimethylpiperazine-bisborane / 20% Epoxy	-	3.9	270.2	378.9	Measured / [72]
80% Ammonia Borane / 20% Epoxy	-	1.1-3.2	279.5-285.1	314.8-360.4	Measured / [72]
Tagaform	150 [2, 4]	3.8	259.9	373.0	[2]
30% p-Toluidine /70% p-Aminophenol	110-122 [3, 4]	3.5	255.9	361.5	[7]
MMH	-	2.6	274.6	350.3	[72]
Hydrazine	3.1 [37]	1.5	278.9	355.0	[72]
Dimethyl Hydrazine	4.5 [37]	3.1	272.4	348.0	[72]

4.4.2 Liquid Hypergolic Fuels

A comparison of the higher performing amine-boranes mixed in a fuel binder and the commonly used hypergolic liquid fuels is also provided in Table 4.6. Hypergolic ignition delays of the amine-borane/fuel binder are very similar to the current liquid hydrazine based fuels. These ignition delay times could decrease, possibly becoming shorter than liquid hypergols, during pulse operation of the motor as the fuel will be preheated from the previous firing, a condition not typical for liquid fuels. The theoretical I_{sp} values of the amine-borane/fuel binders range from slightly lower to a 3.8% increase over MMH values while ρI_{sp} values are all higher than MMH values except for the ammonia borane at low O/F ratios. And again, the wide range of high theoretical performance values associated with the amine-borane fuels provides another advantage over the standard liquid hypergols, see Figure 4.10, allowing for off stoichiometric operation. The combination of similar ignition delays, higher performance, wide range of high performance, and classification as irritants as opposed to toxins make these amine-boranes attractive as replacements for the current more toxic liquid hypergolic fuels.

4.4.3 Non-Hypergolic Fuels

Amine-boranes also have the potential to improve performance of non-hypergolic oxidizer/fuel combinations. A summary of the most prominent amine-borane based fuels reacted with liquid oxygen compared to typical hybrid and liquid fuels is provided in Table 4.7. Both I_{sp} and ρI_{sp} values increase notably anywhere from 2-6% and 1-11% respectively when amine-borane based fuels are used. An exception is liquid H_2 that has significantly higher I_{sp} value than all the other fuels. Applications that would entail the use of the other fuels listed in Table 4.7, excluding liquid H_2, could all benefit by switching to amine-borane based fuels.

Table 4.7 Comparison of theoretical performance values of standard rocket liquid fuels versus solid amine-boranes/fuel binder. Theoretical I_{sp} and ρI_{sp} values calculated using liquid oxygen as the oxidizer, 6.89 MPa chamber pressure, and perfectly expanded to atmospheric pressure.

Fuel	O/F	I_{sp}, s	ρI_{sp}, sg/cm^3	ΔH_f Ref.
80% EDBB / 20% Epoxy	1.8	309.2	319.7	Measured / [72]
80% N,N-Dimethylpiperazine-bisborane / 20% Epoxy	2.0	306.8	336.8	Measured / [72]
80% Ammonia Borane / 20% Epoxy	1.7	318.4	320.3	Measured / [72]
HTPB	2.3	299.7	317.0	[72]
Paraffin	2.9	300.5	303.2	[72]
RP-1	2.6	300.3	302.5	[73]
Liquid H_2	4.1	389.6	112.0	[72]

4.5 General Combustion Behavior – Opposed Burner

Several 58% EDBB/42% HTPB and 100% EDBB fuel pellets that were ignited hypergolically were permitted to continue to burn with the surrounding air once the WFNA was consumed so general combustion behavior could be observed. Pressed EDBB pellets combust with a mixed green and yellow flame that initially is mostly green and then transitions to mostly yellow, Figure 4.12. The pellet proceeds to burn from the surface that was initially ignited producing several distinct layers of solid material that have reacted to varying degrees. These layers include the pristine fuel, a foamy white layer, a solid grey foam like layer, and a charred black layer at the surface. Gas generation is observed in the foamy white layer as the material appears to boil. The gas generation causes this layer to expand notably, a result of the decomposition gases likely being low density hydrogen. A grey, rigid layer of material that continues to exhibit a foam like structure remains once the gas is depleted. This layer eventually blackens and chars forming a rigid, brittle, and porous surface. EDBB/HTPB pellets also expand notably upon combustion with air but individual reaction layers are not distinguishable as the pellet burns from all sides. A similar green and yellow flame is also characteristic of these pellets.

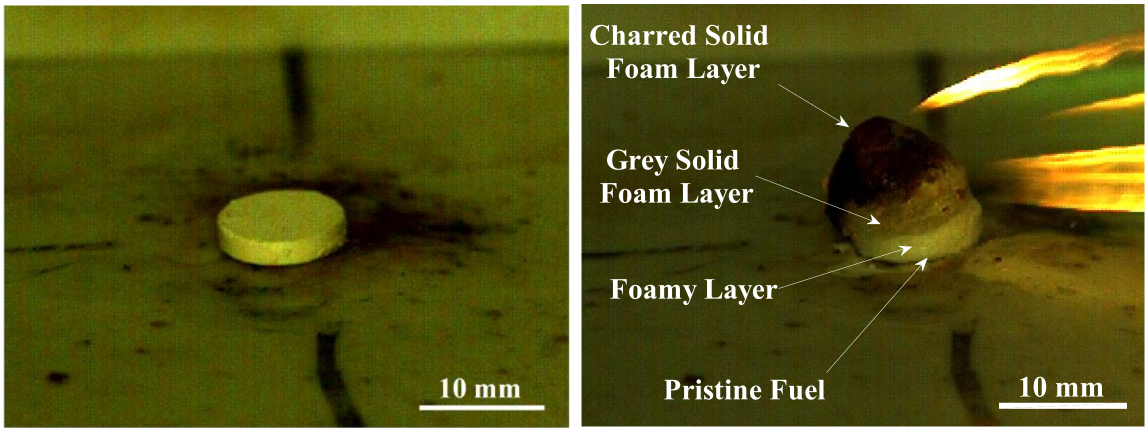

Figure 4.12 Combustion of a pressed EDBB pellet with the surrounding air.

The combustion behavior of pressed EDBB, 58% EDBB/42% HTPB, and neat HTPB pellets with gaseous oxygen were further investigated using an opposed burner. Pressed EDBB pellets initially exhibit a bright green flame upon ignition and continue to do so for several seconds into the experiment, Figure 4.13. As combustion continues, the green flame diminishes exposing a luminous fuel surface that protrudes 1-2 mm past the tungsten wire. Surface imaging of the pellet indicates the luminous surface is always present and becomes less luminous as the bright green flame diminishes, Figure 4.14 (a). The surface tends to be porous with surface voids on order of magnitude of 0.1 mm, the same as the surrounding fuel structure. Regression of the surface appears to be controlled by both gasification of the fuel and fragments breaking off and entering the convective flow around the pellet. Post combustion observation of the fuel pellet indicates several layers of reacted material near the surface similar to those observed for the pressed fuel pellets combusted with the surrounding air. This layered reaction probably results in the luminous surface becoming more prominent as combustion proceeds as a char layer is formed on the fuel surface that extends beyond the flame.

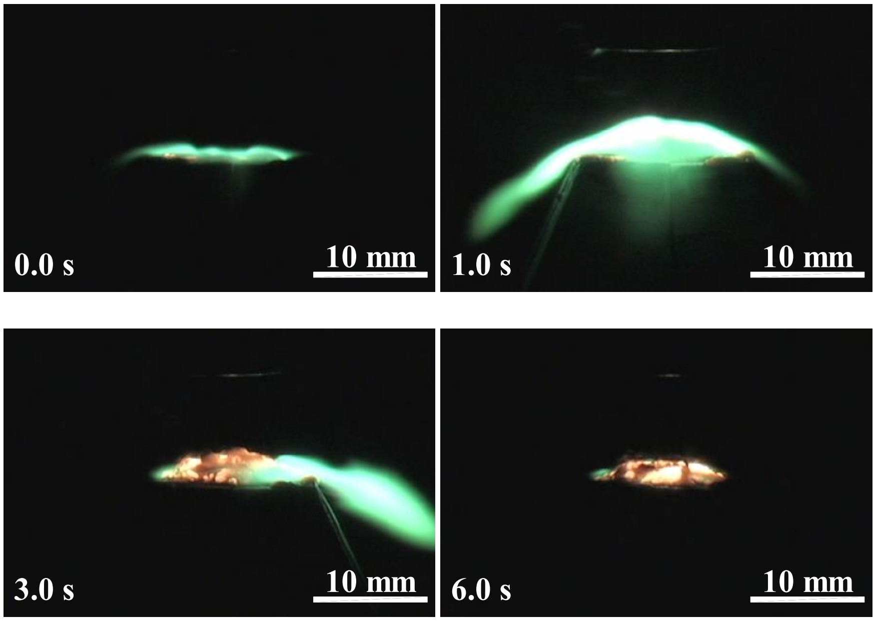

Figure 4.13 Images of a pressed EDBB fuel pellet burning with gaseous oxygen in an opposed burner.

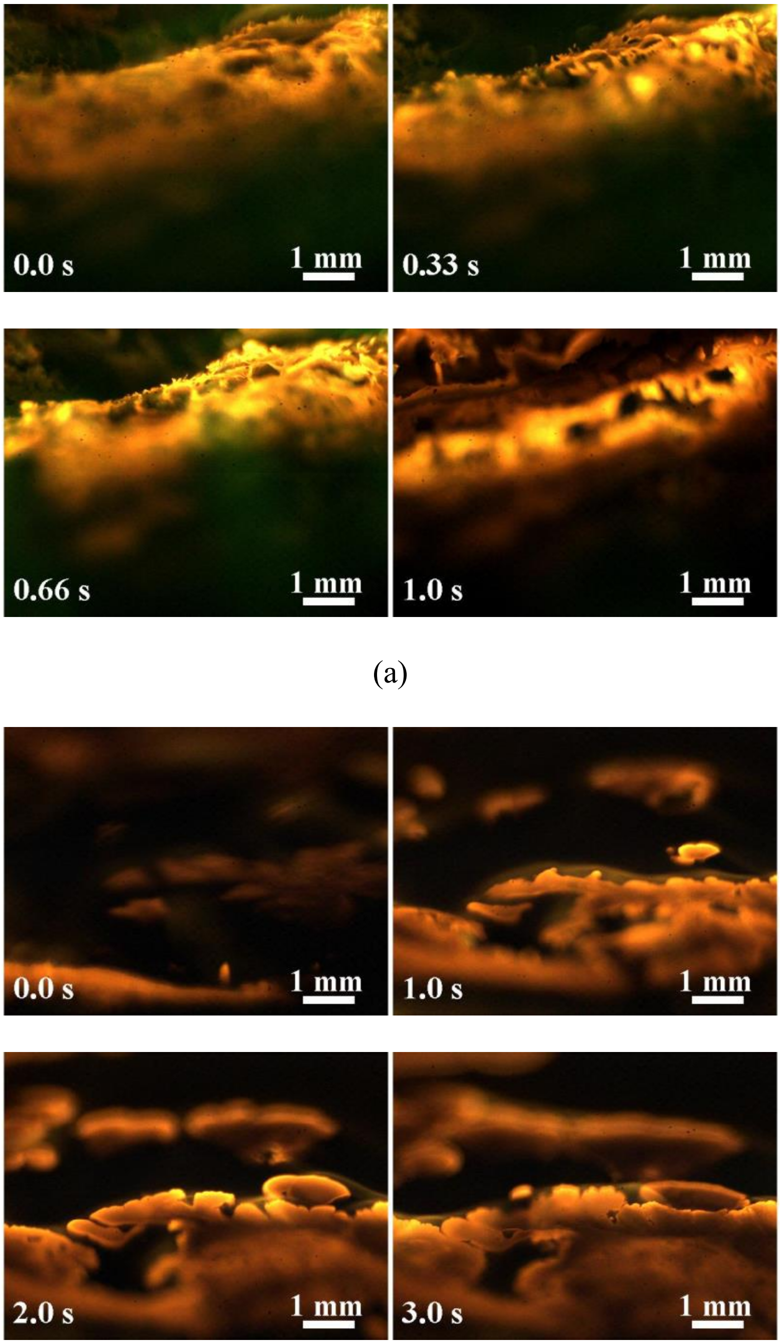
0.0 s
1 mm
0.33 s
1 mm
0.66 s
1 mm
1.0 s
1 mm
0.0 s
1 mm
1.0 s
1 mm
2.0 s
1 mm
3.0 s
1 mm

(a)

(b)

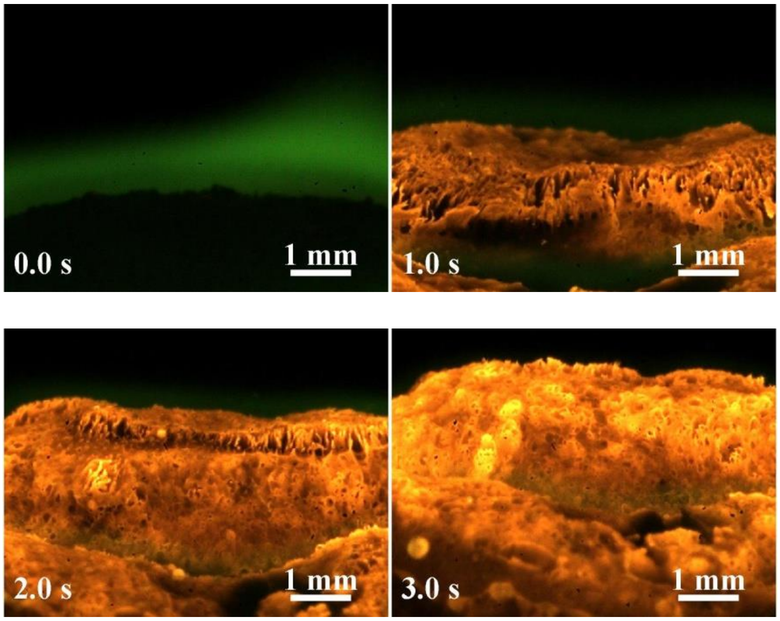

(c)

Figure 4.14 Surface images of (a) pressed EDBB, (b) HTPB, and (c) 58% EDBB/42% HTPB pellets burning with gaseous oxygen in an opposed flow burner.

HTPB pellets exhibit a bright yellow flame throughout the combustion process with the surface remaining relatively in plane with the tungsten wire. Surface imaging reveals a different surface, compared to the pressed EDBB pellets, with less pores and more continuous fuel segments, Figure 4.14 (b). The fuel appears to only regress through gasification as there are no observable fragments leaving the fuel surface. Post combustion analysis reveals a thin, charred layer at the surface of the fuel and pristine material beneath.

EDBB/HTPB pellets exhibit primarily a green flame with some occasional hues of yellow throughout the combustion process. The pellet surface expands dramatically during combustion resulting in a thick layer of char material up to 10 mm thick protruding past the tungsten wire. Post combustion observation of the fuel pellet also indicates layered combustion similar to the pressed EDBB pellets.

Surface imaging of EDBB/HTPB pellets provides images that show a dramatic change in the texture of the surface when EDBB and HTPB are combined when compared to the individual fuels, see Figure 4.14 (c). Initially the surface exhibits a highly porous surface with fiber like features that tend to fragment off and enter the convective flow but also exhibit gasification. As combustion continues, the fibrous surface becomes more coral or foam like with much smaller surface pores and surface features than the individual fuels.

The regression rates of the pellets combusting with oxygen were also measured. All regression rates were measured at the same gaseous oxidizer flow rate of 25 SLPM to provide a general idea of how regression rates compare, the results of which are tabulated in Table 4.8. Pressed EDBB pellets regressed faster than the other fuels with an average regression rate of 0.58 ± 0.09 mm/s. The regression rate of HTPB was nearly half that having an average regression rate of 0.28 ± 0.00 mm/s. The difference could be attributed to a difference in flame temperature, a lower amount of heat needed to raise the temperature and gasify the EDBB fuel, or possibly due to the configuration. The HTPB pellet diameters were 12 mm fitting snugly in the apparatus, whereas the EDBB pressed pellets were 10 mm in diameter providing a small gap between the pellet and the apparatus. It is possible some of the heat from the flame was able to pass through this gap, preheating the pristine fuel. However, it is unlikely that some preheating would cause such a dramatic change in regression rate, thus it is likely different flame temperatures or heat required to gasify the material was notably different.

Table 4.8 Average linear regression rates of various forms of EDBB fuel pellets obtained in a gaseous oxygen opposed burner.

Fuel Type	Oxidizer Flow Rate, SLPM	Linear Regression Rate, mm/s
HTPB	25	0.28 ± 0.00
Pressed EDBB B Powder	25	0.58 ± 0.09
58% EDBB B Powder /42% HTPB	25	0.21 ± 0.01

Mixing EDBB and HTPB resulted in a 25% decrease in the regression compared to HTPB when burned with oxygen. As noted previously, the thickness of the partially reacted foam like layers on the EDBB/HTPB pellet was about 10 mm thick. Such a layer probably inhibited the convective heat transfer to the surface of the fuel pellet, resulting in lower regression rates.

The spectral emissions of flames from both pressed EDBB and HTPB pellets were recorded using a high speed IR spectrometer. Measurements obtained throughout the flames resulted in similar temperatures and spectral profiles. Sample spectral measurements are shown in Figure 4.15 with corresponding apparent emissivities of 0.04 and 0.05 for EDBB and HTPB respectively. The main difference between the spectral emission profiles of these two fuels is the discrepancy at a wavelength of ~4.5 μm. At this point, HTPB exhibits a notable peak, corresponding to CO_2, a peak that is not observed for the EDBB pellets. This could be a result of HTPB having a notably higher mass fraction of carbon than EDBB. This general spectral emission behavior was observed throughout the flame.

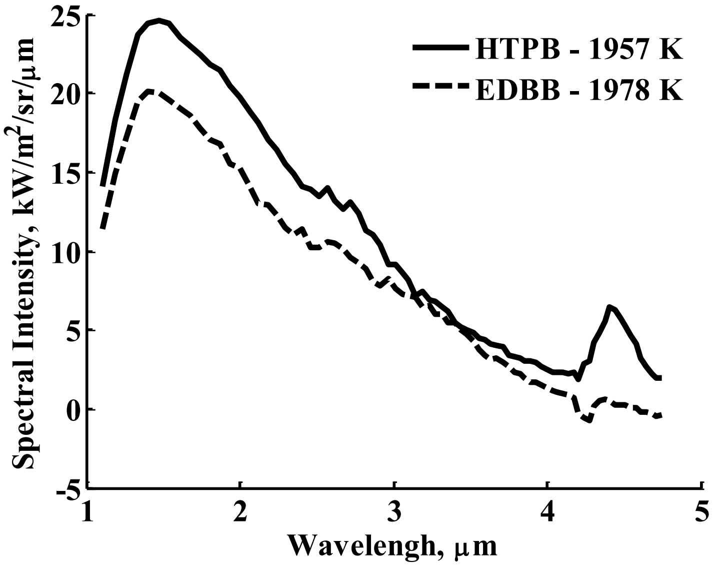

Figure 4.15 Spectral emission of both EDBB and HTPB at similar flame temperatures.

Flame temperatures were also measured with the IR spectrometer resulting in relatively similar average maximum temperatures of 1995 ± 15 K and 1984 ± 25 K for EDBB and HTPB respectively. This similar peak temperatures is significant as it indicates that convective heat transport to fuel surface is roughly the same for both fuel pellets, assuming the 1 mm thick layer on top of the EDBB pellet is not significantly influencing the heat transfer. Assuming this is the case and that radiation is negligible or the nearly the same, given the spectral emission similarities in Figure 4.15, the amount of energy required to heat and gasify EDBB, $h_{v,EDBB}$, can be roughly estimated, given the value is known for HTPB. Lengelle calculated $h_{v,HTPB}$ to be 745 cal/g for HTPB burning in a hybrid motor with a flux of 16 g/cm^2 [86]. Thus,

$$h_{v,EDBB} = \frac{\dot{r}_{HTPB}\rho_{HTPB}h_{v,HTPB}}{\dot{r}_{EDBB}\rho_{EDBB}}$$

where $\dot{r}$ is the regression rate and ρ is the fuel density. This gives a value of $h_{v,EDBB}$ = 400 cal/g, a value that will be useful when evaluating the hybrid combustor results. Given such a value, it is likely that a fuel containing a high amount of EDBB will regress notably faster than HTPB if no partially reacted foam layer forms as was observed for the EDBB/HTPB pellets.

CHAPTER 5. ROCKET COMBUSTOR RESULTS

The hybrid rocket combustor test series consisted of nine tests – seven that produced continuous combustion, one that quenched mid test, and one that did not ignite. The methods used to reduce the test data and the resulting combustion behaviors are presented in this following chapter.

5.1 Data Reduction

The average oxidizer to fuel ratio, O/F, for each test was determined by dividing the total amount of oxidizer, m_{ox}, used in the test by the amount of fuel consumed, m_{fu}. The volume of oxidizer was measured using a graduated beaker and converted to mass using the oxidizer density, ρ_{ox}, of 1.48 g/cm^3. A small amount of oxidizer would become trapped in the fill line and was accounted for in one the following ways: If the test was the first of the day, the volume of the unused oxidizer was measured and subtracted from the amount of oxidizer loaded to determine m_{ox}. If the test was a subsequent test during the day and the oxidizer fill line had not been drained prior to testing, the total amount of oxidizer introduced into the system was m_{ox} as the fill line was already full. The amount of fuel consumed was determined by measuring difference in mass of the fuel grain/phenolic/nozzle/rtv assembly before and after testing.

Fuel density, ρ_{fu}, was determined by measuring the mass and dimensions for each fuel grain before cutting notches into the grains and then using the following formula,

$$\rho_{fu} = \frac{4m_{fu}}{\pi\left(D_o^2 - D_p^2\right)L_g} \tag{5.1}$$

where D_o is the grain outer diameter, D_p is the fuel port diameter, and L_g is the grain length.

The burn time, t_b, was determined by taking the difference in times from when the chamber pressure, p_c, was greater than 10% of the max steady state combustor pressure, $p_{c,ss}$, at the beginning and end of the test. An example of this is provided in Figure 5.1.

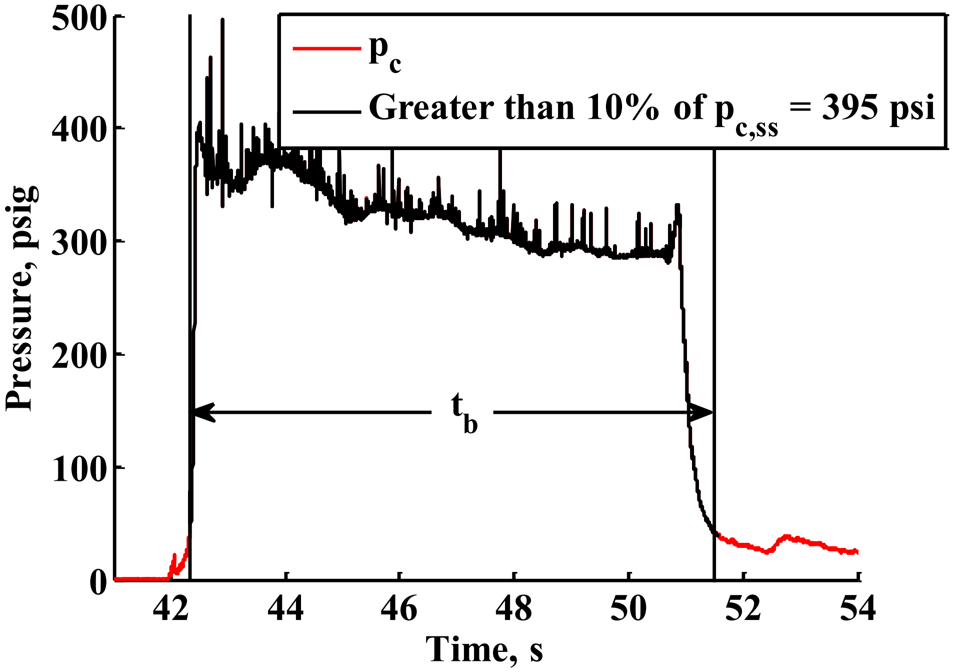

Figure 5.1 The chamber pressure of a rocket test indicating the recorded chamber pressure (red) and the section of chamber pressure used for analysis (black). This particular data is from test #6 that resulted in a t_b= 9.228 s.

For three tests, the p_c measurement port became plugged for all or part of the test. For such tests, p_c was determined by relating the pressure drop across the injector to the oxidizer flow rate, $\dot{m}_{ox}$, via,

$$p_c = p_{inj} - \frac{1}{2g\rho_{ox}}\left(\frac{\dot{m}_{ox}}{A_{inj}C_{d,inj}}\right)^2 \tag{5.2}$$

where p_{inj} is the upstream injector pressure, g is the gravitational constant, A_{inj} is the injector orifice cross sectional flow area, and $C_{d,inj}$ is the injector discharge coefficient. The $C_{d,inj}$ was determined from the latter portion of test #8; this test initially had a plugged p_c measurement that became unplugged as the test proceeded, see Figure 5.2. The $C_{d,inj}$ was found to be 1.084 for a pressure drop across the injector of 57 psi.

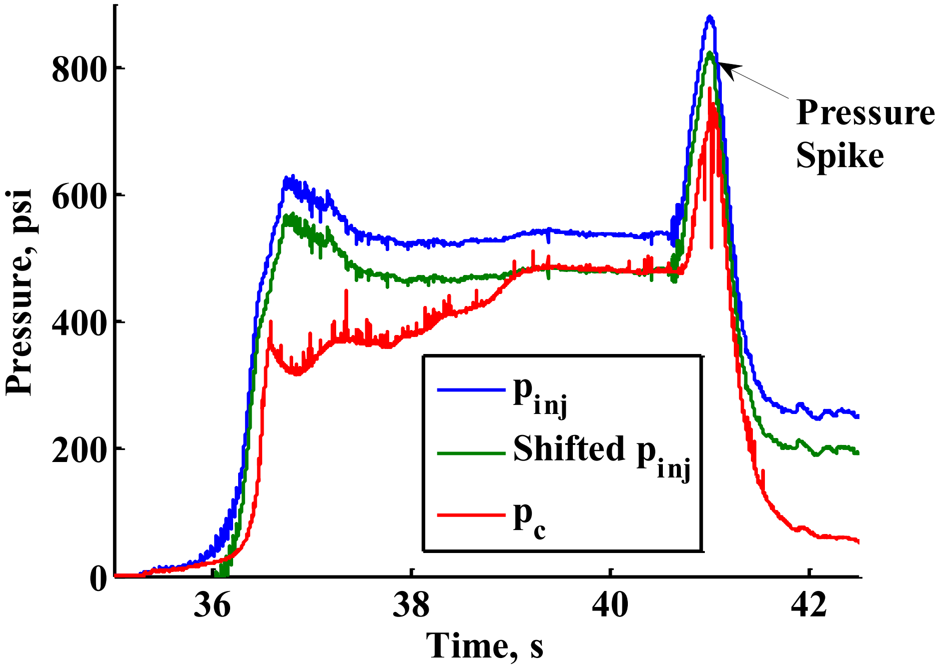

Figure 5.2 The pressure traces for a test in which the chamber pressure port became obstructed. In this test (#8), the port was obstructed for only part of the test.

Such a method introduces some error for p_c during the transient ignition and shutdown regions; however, the steady state combustion region is well represented as $\dot{m}_{ox}$ becomes nearly constant. Due to the purging of the system, the calculated p_c for such tests does not return to atmospheric pressure once the test is completed, as is the case for tests that do not have the p_c measurement port plugged. In order to determine the end of the burn time for these tests, 0.75 s was added after p_{inj} spiked, see Figure 5.3. A time of 0.75 s was chosen as this was the amount of time between when p_{inj} spiked to when p_c reached 10% of $p_{c,ss}$ for a test with similar operating parameters as several of the tests that had plugged p_c measurements. The pressure spike is caused by all the liquid oxidizer moving past the cavitating venturi causing nitrogen gas to be the flow rate determining media. Once all the oxidizer has passed the injector, the pressure spike drops off and the combustor pressure returns to atmospheric conditions.

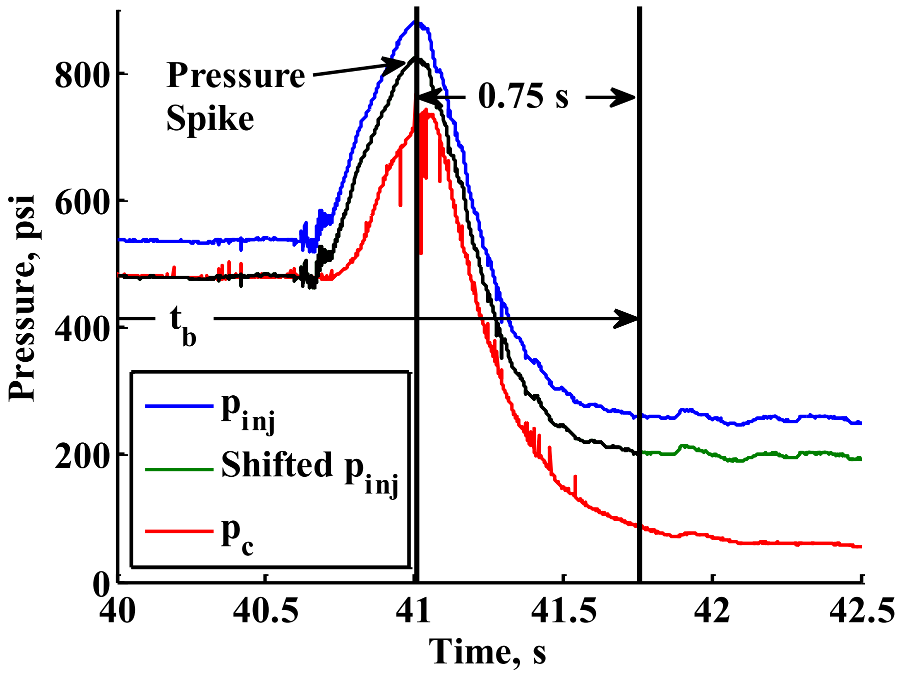

Figure 5.3 The 0.75 s added after p_{inj} spiked in order to determine p_c for the tests that had a plugged p_c port.

Total ignition time, t_{ign}, was determined as the difference in time from when p_{inj} deviates from atmospheric pressure to when p_c reached 90% of its initial steady state operating pressure, see Figure 5.4.

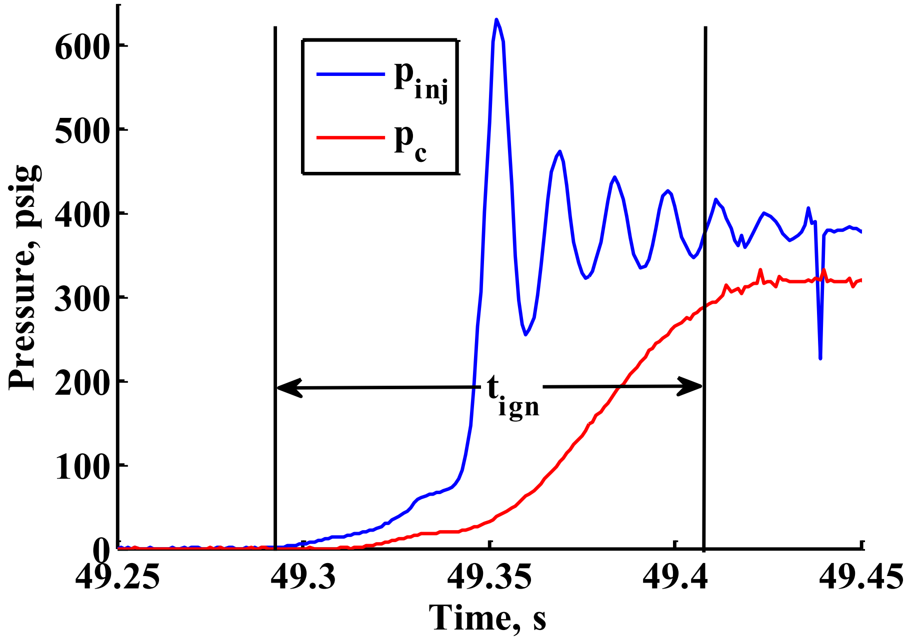

Figure 5.4 An example of p_{inj} and p_c during the hypergolic ignition transient from test #4. The resulting t_{ign}= 0.117 s.

The average chamber pressure, $p_{c,avg}$, is the average of the pressure trace presented in Figure 5.1 for the time interval corresponding to t_b.

The delivered characteristic velocity, C^*, was determined using the following equation,

$$C^* = \frac{gA_{th}}{(m_{ox}+m_{fu})}\int_0^{t_b} p_c\, dt \qquad (5.3)$$

where A_{th} is nozzle throat area. The pressure trace integrated over time is the same pressure trace used to calculate $p_{c,avg}$. The characteristic velocity efficiency, η_{C^*}, was determined using the following equation,

$$\eta_{C^*} = {C^*}/{C^*_{the}} \qquad (5.4)$$

where C^*_{the} is the theoretical characteristic velocity calculated using average O/F, $p_{c,avg}$, and Cheetah 6.0 [72].

The average fuel regression rate, $\bar{\dot{r}}$, was determined using a bulk mass fuel consumed method. The total volume of fuel, V_{fu}, consumed can be determined from ρ_{fu} and m_{fu}. Assuming a fuel regression normal to the surface (Figure 5.5 (a)), the web thickness, w, (or depth of fuel consumed) can be found based off V_{fu}, and the surface area of the fuel, A_s, can be determined as a function of w, see Figure 5.5 (b). Averaging A_s over w, $\bar{A}_s$, can allow for a bulk $\bar{\dot{r}}$ measurement based on,

$$\bar{\dot{r}} = \frac{m_{fu}}{t_b \rho_{fu} \bar{A}_s}. \tag{5.5}$$

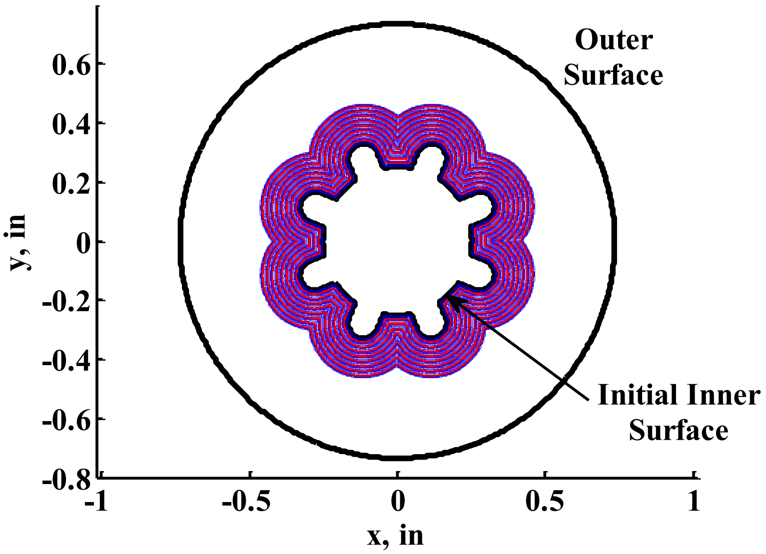

(a)

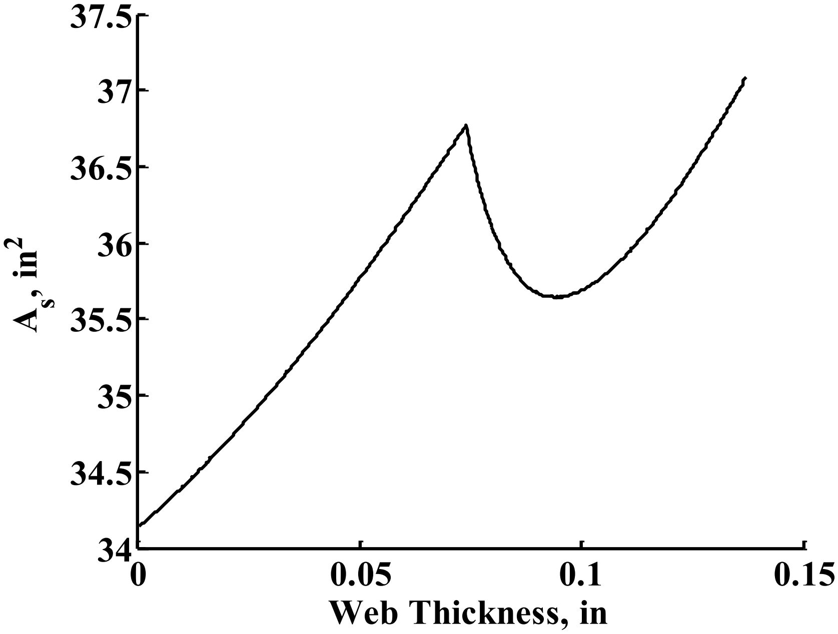

(b)

Figure 5.5 Fuel surface as a function of w based off of surface normal regression (a) and the corresponding A_s (b). The curves in these plots correspond to Test #9. The red and blue lines indicate 0.016 and 0.0016 in web thickness increments respectively.

A second method was used to determine $\bar{r}$, serving as a validation for the bulk mass method. This method used a geometrical approach by using m_{fu} combined with the initial and final grain surface areas after the following manner,

$$\bar{r} = \frac{2m_{fu}}{t_b \rho_{fu} L_g (Per_f + Per_0)} \tag{5.6}$$

where Per_f and Per_0 and the final and initial fuel port perimeters. Due to swelling at the surface of the fuel grain post test, determining Per_f is challenging, see Figure 5.6 (a). The perimeter of the char layer can appear to shrink when compared to Per_0, the red dashed lines in Figure 5.6; however, a thermally reacted layer can be seen farther into the fuel grain. Upon polishing of the section fuel grain with 600 grit sandpaper and water, the thermal reacted layer is removed leaving what appears to be pristine fuel at the surface, see Figure 5.6 (b). The perimeter length of the fuel port after being polished can then be evaluated using Matlab, and this value can be set to Per_f in order to determine $\bar{r}$.

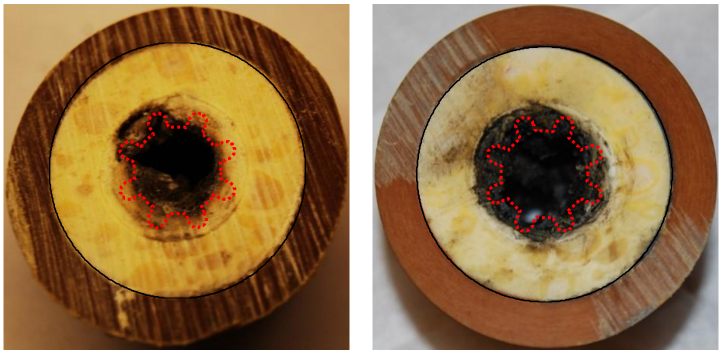

(a) (b)

Figure 5.6 A section of a fuel grain showing the swelling of the fuel grain (a) before and (b) after being polished. The red dashed line indicates Per_0.

The average oxidizer flux level, $\bar{G}_{ox}$, is determined by finding the average fuel port area, $\bar{A}_p$, over w (similar to the method used to determine $\bar{A}_s$) and using an average oxidizer flow rate, $\bar{\dot{m}}_{ox}$, from the test. The $\bar{\dot{m}}_{ox}$ is determined by taking the average of the oxidizer flow rate, $\dot{m}_{ox}$, for the same time interval corresponding to t_b.

The $\dot{m}_{ox}$ is controlled using a cavitating venturi and determined by,

$$\dot{m}_{ox} = A_{ven} C_{d,ven} \sqrt{2 g \rho_{ox} \left(p_{tank} - p_{vap}\right)} \tag{5.7}$$

where A_{ven} is the venturi cross sectional flow area, $C_{d,ven}$ is the venturi discharge coefficient, p_{tank} is the liquid oxidizer tank pressure, and p_{vap} is the oxidizer vapor moxbased off of Eqn. $pvap$ (5.7 from test #6 is provided in Figure 5.7.

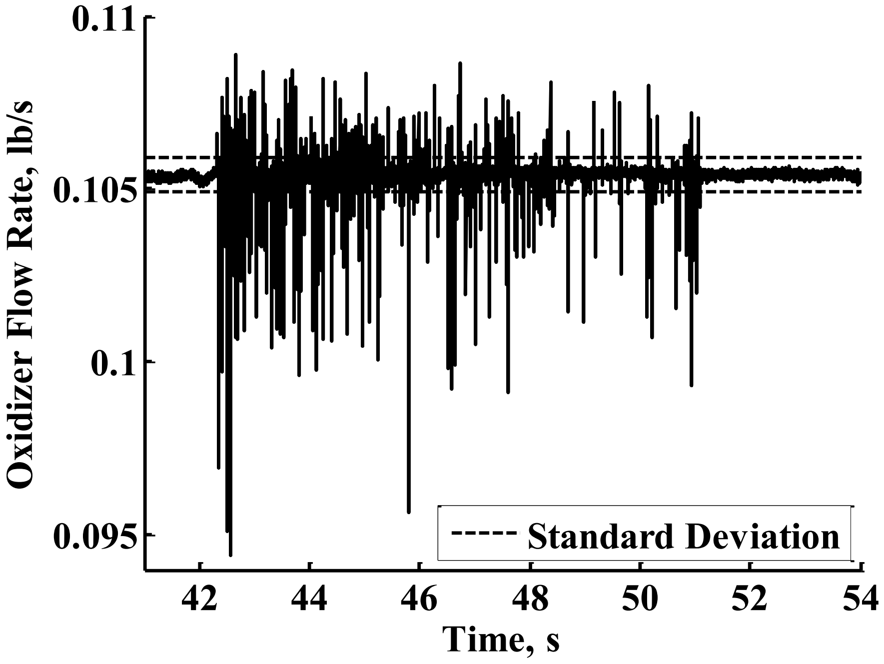

Figure 5.7 Oxidizer flow rate as a function of time during operation of the combustor from test #6.

The cavitating venturi results are provided in Table 5.1 along with t_b and oxidizer flow time – the amount of time it would take to expend all of the oxidizer based on the oxidizer flow rate. Although one second discrepancy between oxidizer flow time and t_b is possible due to transients captured in t_b and high $\dot{m}_{ox}$ at the end of the test when nitrogen gas encounters the cavitating venturi, large consistent discrepancies between oxidizer flow time and t_b is noted for tests 2, 3, and 7, indicating the same cavitating venturi used in these tests was not functioning properly.

$ptank$ and Eqn. $pvap$ (5.7.

Test I.D.	Venturi Diameter, in	Injector	$\dot{m}_{ox}$, lb/s	m_{ox}, lb	Oxidizer Flow Time, s	t_b, s
1	0.025	GG-1	-	0.1403	-	-
2	0.019	GG-1	0.0399	0.1403	3.516	5.498
3	0.019	GG-1	0.0399	0.2708	6.787	9.427
4	-	GG-1	-	0.1468	-	3.670
5	0.037	GG-3	0.1751	1.576	9.001	9.535
6	0.029	GG-2	0.1054	0.956	9.070	9.228
7	0.019	GG-1	0.0399	0.2708	6.787	10.46
8	0.015	GG-1	0.0397	0.2708	6.821	5.553
9	0.025	GG-2	0.1056	0.956	9.053	8.413

The venturi was subsequently calibrated with deionized water and found to have a proper value for $C_{d,ven}$. The pressure recovery across the venturi was then determined using deionized water and by controlling the downstream pressure using a manual valve. The valve was gradually opened until cavitation occurred in the venturi. The pressure downstream of the venturi was found to be 35% of the upstream pressure upon cavitation. Such a pressure loss was much more than the standard 80% of the upstream pressure. The tests that used this venturi had around a downstream pressure between 40-70% of the upstream pressure, indicating that the venturi was not cavitating during these tests and not controlling the flow rate.

To determine the oxidizer flow rate for test #2, Eqn. 5.2 was used along with the measured p_c and p_{inj} from that test and a $C_{d,inj}$ of 1.1. This method did not work for test #3 and #7 because the p_c measurement was plugged for those tests. Thus, $\dot{m}_{ox}$ was calculated by dividing the amount of oxidizer loaded by t_b. As $\dot{m}_{ox}$ and t_b become interdependent using this method, both values are iterated until a solution is found. The corrected oxidizer flow rates and times exhibit more consistent values with t_b, see Table 5.2.

Table 5.2 Corrected oxidizer flow rates and times.

Test I.D.	Venturi Diameter, in	Injector	$\dot{m}_{ox}$, lb/s	m_{ox}, lb	Oxidizer Flow Time, s	t_b, s
1	0.025	GG-1	-	0.1403	-	-
2	0.019	GG-1	0.0274	0.1403	5.120	5.498
3	0.019	GG-1	0.0287	0.2708	9.427	9.427
4	-	GG-1	0.0447	0.1468	3.284	3.670
5	0.037	GG-3	0.1751	1.576	9.001	9.535
6	0.029	GG-2	0.1054	0.956	9.070	9.228
7	0.019	GG-1	0.0259	0.2708	10.46	10.46
8	0.015	GG-1	0.0397	0.2708	6.821	5.553
9	0.025	GG-2	0.1056	0.956	9.053	8.413

The uncertainty of the data obtained from the data reduction methods just described is found by using the formula provided by Coleman and Steele [87] given by,

$$\left(\frac{U_y}{y}\right)^2 = \sum_{i=1}^{N}(UMF_i)^2\left(\frac{U_{X_i}}{X_i}\right)^2 \tag{5.8}$$

where U is the uncertainty of a variable, y is the variable with an unknown uncertainty, i is the number a variables used to calculate y, and UMF is the uncertainty magnification factor given by,

$$UMF_i = \frac{X_i}{y}\frac{\partial y}{\partial X_i}. \tag{5.9}$$

The results of this analysis is provided in Table 5.4. All of these values are based on measured parameters except for $\dot{r}_{avg}$ and $G_{ox,avg}$. The calculations to determine these variables both use $\bar{A}_s$, a value provided by a computer and not measured. Thus, the uncertainties for these two variables are provided as a reference, under the inherent assumption that there is no uncertainty in $\bar{A}_s$ which is not the case.

5.2 General Observations

The data from the combustor tests is provided in Table 5.3. Little data is provided for test #1 as this test experienced varying oxidizer flow rates causing it to quench and providing inconsistent combustion characteristics. This behavior was a result of having excess volume between the cavitating venturi and the injector coupled with low $\dot{m}_{ox}$. As the test proceeded, the oxidizer passed the venturi causing nitrogen to become the flow rate controlling media, increasing $\dot{m}_{ox}$ notably and quenching the combustor. The data from this test was thus inconsistent and not used. For subsequent tests, the excess volume was removed between the venturi and injector resulting in consistent operation.

Table 5.3 Test parameters and reduced data from the rocket combustor tests.

Test I.D	1	2	3	4	5	6	7	8	9
Injector	GG-1	GG-1	GG-1	GG-1	GG-3	GG-2	GG-1	GG-1	GG-2
Fuel Grain Length, in	6.23	6.23	12.39	6.24	12.39	12.54	12.46	5.97	12.21
Fuel Port Initial Diameter, in	0.50	0.57	0.50	0.50	0.75	0.50	0.50	0.50	0.50
Number of Cut Slots	0	8	8	8	0	8	8	8	8
m_{ox}, lb	0.27	0.14	0.27	0.15	1.58	0.96	0.27	0.27	0.96
m_{fu}, lb	0.0084	0.0143	0.0769	0.0090	0.0542	0.0968	0.0983	0.0525	0.1479
ρ_{fu}, lb/in^3	0.0298	0.0298	0.0299	0.0297	0.0299	0.0296	0.0298	0.0309	0.0304
O/F	32.3	9.8	3.5	16.2	29.1	9.9	2.8	5.2	6.5
t_b, s	-	5.498	9.429	3.670	9.535	9.228	10.463	5.553	8.413
$\dot{m}_{ox}$, lb/s	-	0.027	0.029	0.045	0.175	0.105	0.026	0.040	0.106
$G_{ox,avg}$, lb/in^{2}s	-	0.075	0.079	0.153	0.344	0.276	0.067	0.101	0.238
$\dot{r}_{avg}$, in/s	-	0.00447	0.00735	0.00456	0.00605	0.00928	0.00840	0.01700	0.01622
$p_{c,avg}$, psi	-	172	294	228	53	304	289	469	407
η_{C^*}	-	0.83	0.81	0.89	-	0.84	0.80	0.73[a]	0.82[a]
t_{ign}, s	-	1.027	0.884	0.117	-	0.494	0.909	1.378	0.518
Post Test Swelling	No	No	Yes	No	No	No	Yes	Yes	Yes
Notes	Quenched	-	Plugged p_c/ Swelled Shut	No Venturi	No Ignition	-	Plugged p_c/ Swelled Shut	Nozzle Erosion/ Partially Plugged p_c/ Swelled Shut	Nozzle Erosion/ Swelled Shut

a. Values calculated using average of initial and final nozzle throat diameters.

Table 5.4 Uncertainty in test parameters.

Test I.D	1	2	3	4	5	6	7	8	9
Fuel Grain Length, in	±0.001	±0.001	±0.002	±0.001	±0.002	±0.002	±0.002	±0.001	±0.002
Fuel Port Initial Diameter, in	±0.001	±0.001	±0.001	±0.001	±0.001	±0.001	±0.001	±0.001	±0.001
m_{ox}, lb	±0.01	±0.01	±0.01	±0.01	±0.08	±0.05	±0.01	±0.01	±0.05
m_{fu}, lb	±0.0001	±0.0001	±0.0001	±0.0001	±0.0001	±0.0001	±0.0001	±0.0001	±0.0001
ρ_{fu}, lb/in^3	±0.0004	±0.0004	±0.0004	±0.0004	±0.0004	±0.0004	±0.0004	±0.0004	±0.0004
O/F	±1.6	±0.5	±0.2	±0.8	±1.5	±0.5	±0.1	±0.3	±0.3
t_b, s	-	±0.001	±0.001	±0.001	±0.001	±0.001	±0.001	±0.001	±0.001
$\dot{m}_{ox}$, lb/s	-	±0.006	±0.002	±0.008	±0.010	±0.007	±0.001	±0.005	±0.008
$G_{ox,avg}$, lb/in^{2}s	-	±0.017	±0.004	±0.026	±0.018	±0.018	±0.003	±0.014	±0.019
$\dot{r}_{avg}$, in/s	-	±0.00001	±0.00001	±0.00001	±0.00001	±0.00001	±0.00001	±0.00002	±0.00002
$p_{c,avg}$, psi	-	±2	±2	±2	±2	±2	±2	±2	±2
η_{C^*}	-	±0.05	±0.04	±0.05	-	±0.05	±0.04	±0.05	±0.05
t_{ign}, s	-	±0.001	±0.001	±0.001	-	±0.001	±0.001	±0.001	±0.001

A typical test consisted of a sharp rise in p_c as the injector pressurized and hypergolic ignition occurred, see Figure 5.8. After reaching steady state combustion, both p_c and p_{inj} would maintain a consistent pressure difference as both tended to decrease during the duration of the test. A spike in both p_c and p_{inj} would occur at the end of the test as the oxidizer passed the cavitating venturi making nitrogen the controlling flow rate media for a brief moment. Subsequently, both p_c and p_{inj} would decrease quickly reaching their purge pressures.

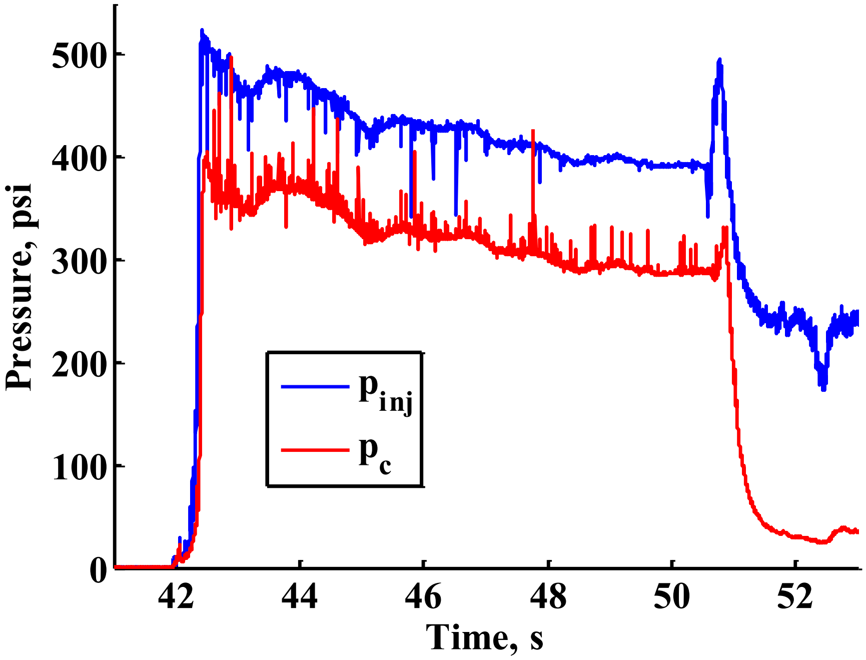

Figure 5.8 Typical p_c and p_{inj} pressure traces during combustor operation from test #6.

The combustor generally exhibited smooth combustion with most pressure oscillations under ±1 psi, see Figure 5.9. There are a several “popping” type events with amplitudes between 2-40 psi. These events may be attributed to rapid reaction of liquid oxidizer within fuel surface irregularities formed in the regressing fuel grain. They may also be the result of some condensed phase products passing through the nozzle causing a momentary decrease in throat area and an increase in pressure. Observations of condensed phase exiting products the nozzle were made using a high speed camera, supporting this theory, see Figure 5.10. The images show a large amount of condensed phase products passing through the nozzle; however, such visible quantities of condensed phase products only occurred a few times during the test. The majority of the pressure oscillations that deviated more than ±2 psi did not have visibly notable condensed phase products pass through the nozzle.

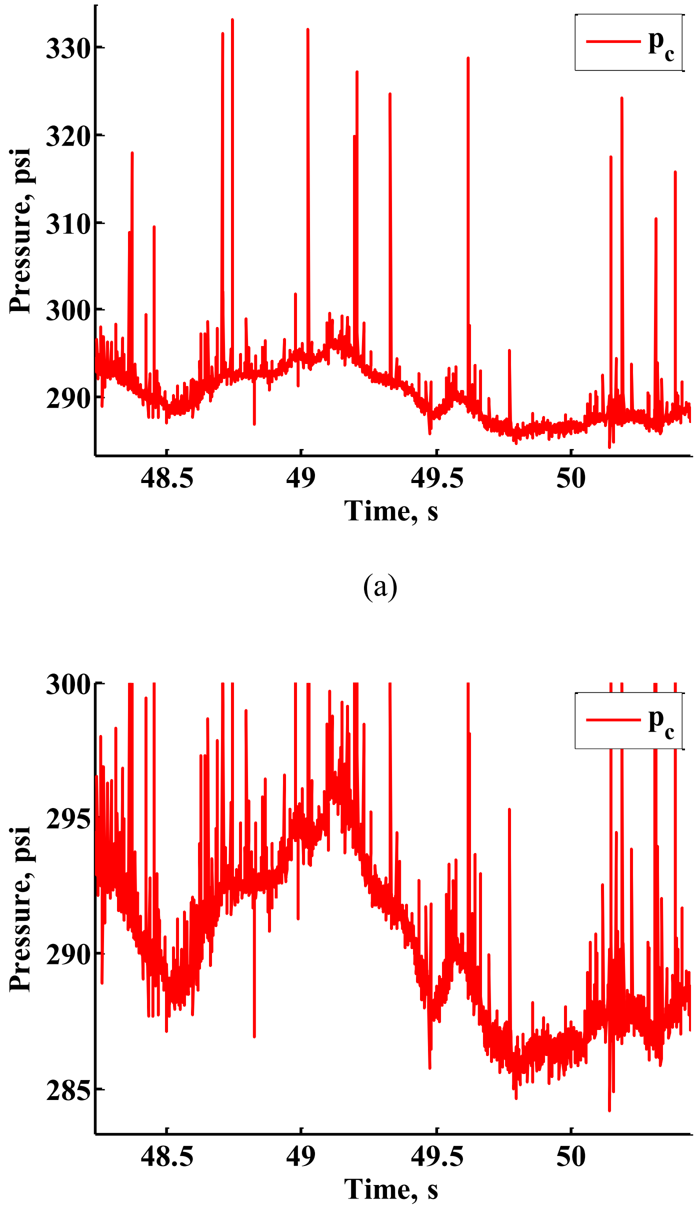

(a)

(b)

Figure 5.9 Typical pressure oscillations for p_c from test #6. Part (b) has a small y-scale than (a) allowing for better observation of the smaller pressure oscillations.

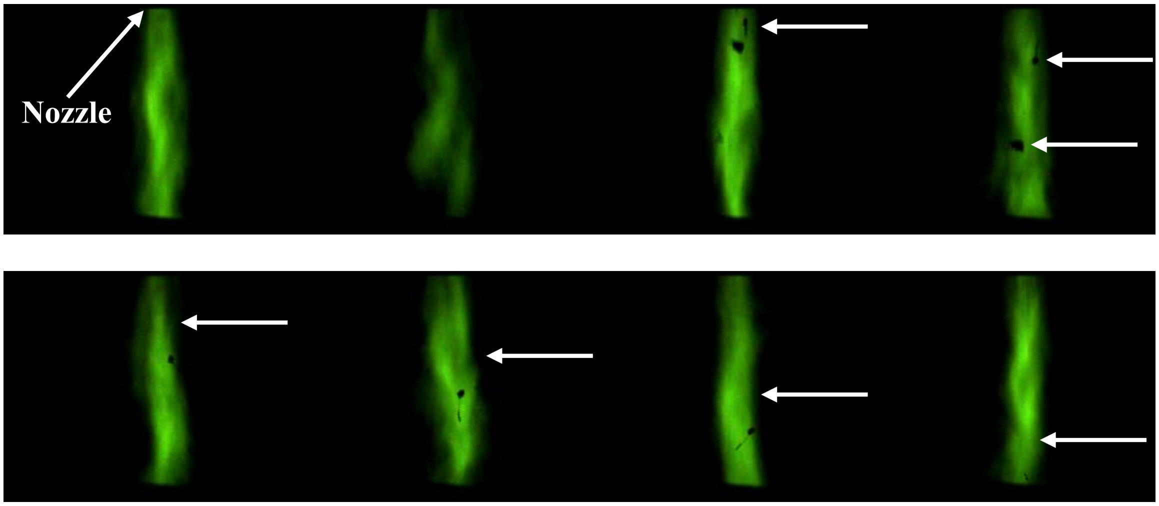

Figure 5.10 Condensed phase material (noted by white arrows) exiting out of combustor through nozzle. Images are in succession with a time difference of 1 ms between each image.

The exhaust plume exhibited a color range from clear to bright green. The bright green flame occurred when the O/F ratio was close to stoichiometric (O/F ≈ 3.9) conditions whereas the clear flame occurred in oxidizer rich combustion. This behavior is depicted in Figure 5.11 with representative images of both stoichiometric and oxidizer rich conditions, taken from test #9. The bright green flame occurs early in the test when p_c and fuel regression rate are both high, producing near stoichiometric combustion Figure 5.11 (a). After the nozzle erodes, p_c decreases causing $\dot{m}_{fu}$ to decrease, which results in oxidizer rich combustion and generates a clear flame, Figure 5.11 (b).

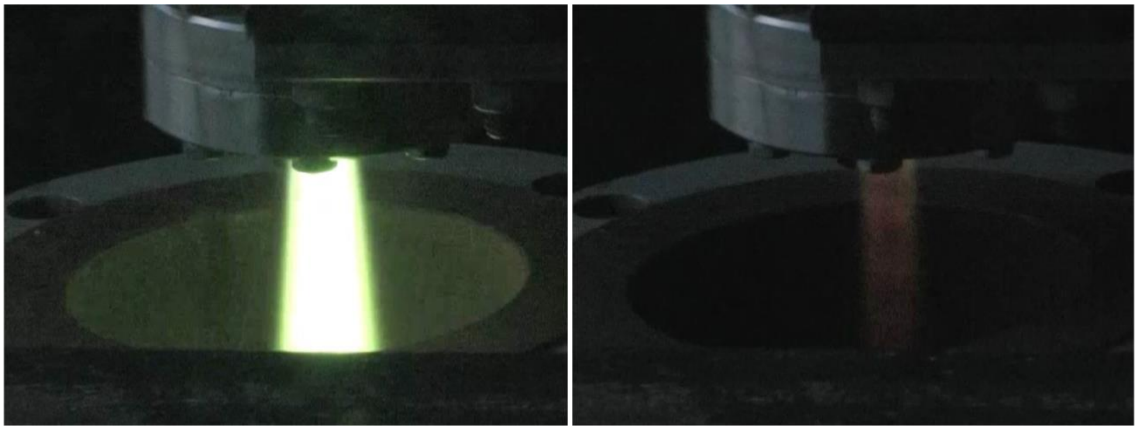

(a) (b)

Figure 5.11 Exhaust plume from test #9 during near stoichiometric (a) and oxidizer rich (b) combustion.

Once passing through the exhaust tube, the exhaust is clear under both stoichiometric and oxidizer rich conditions. Further downstream of the exhaust tube, it appears that condensed phase products were produced, as a faint smoke was occasionally observed. Chemical equilibrium calculations performed in Cheetah 6.0 predict boron containing combinations of B_2O_3, BHO_2, $B(OH)_3$, BN, and others, all of which would condense to solids at room temperature, resulting in smoke. A borosilicate disk was placed in the exhaust of several tests to collect products that were later analyzed with a Bruker D8 X-ray diffraction (XRD) machine. Both condensed phase crystalline $B(OH)_3$ and BN were observed, see Figure 5.12, suggesting that the chemical equilibrium calculations are correct and the smoke is boron based condensed phase products. Condensed phase B_2O_3 and BHO_2 were also likely present on the borosilicate disk but in amorphous form; however, this was not verified.

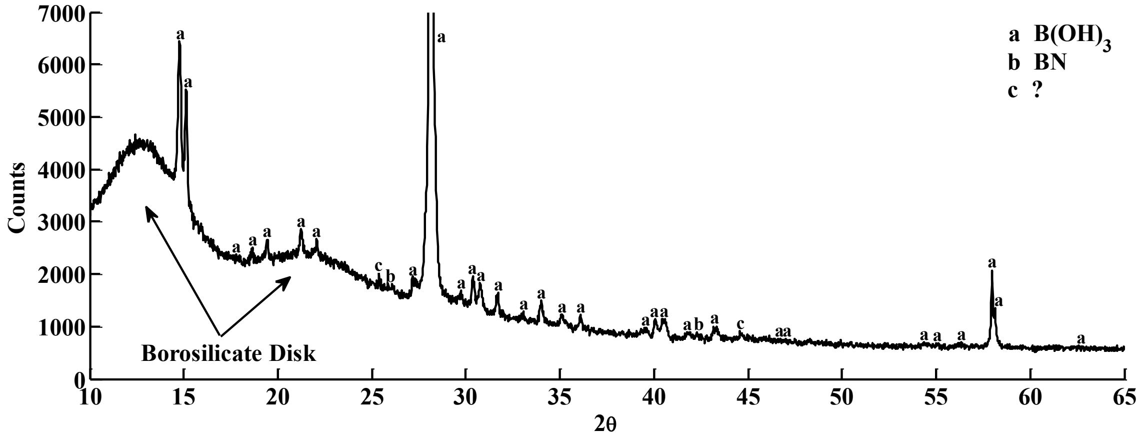

Figure 5.12 Results of XRD analysis of combustion products that have exited the combustor.

Radial swelling of the fuel grain caused by gas generation near the phenolic liner is sometimes observed after the test is complete resulting in the fuel constricting, see Figure 5.13. This behavior was observed when the O/F of the test was nearer stoichiometric ratios and typically occurred towards the aft end of the fuel grain. It is likely the swelling was caused by the higher combustion temperatures associated with near stoichiometric combustion and the higher core flow temperatures more prevalent at the aft end of the motor. Some of the charred surfaces become pinched in the swelled section of the motor indicating it is likely that the swelling occurred after combustion was complete.

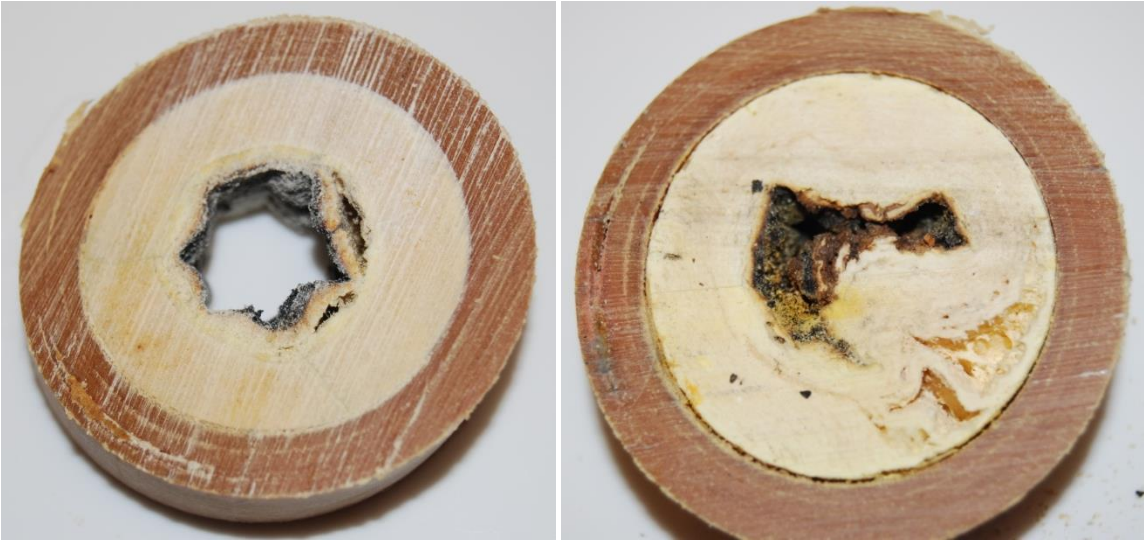

(a) (b)

Figure 5.13 Sections of the fuel grain from test #9 where swelling did not occur at the head end (a) and did occur at the aft end (b).

The nozzle typically becomes clogged after the test for the tests in which the grain swells post combustion, see Figure 5.14. This causes p_c to rise during purge phase resulting in some condensed phase products to be expelled until the products cool. The combination of swelling of the fuel grain and expulsion of condensed phase products post-test means that the measured m_{fu} for these tests may be a little high; however, it is likely the amount expelled post-test is minimal as the results are similar to those tests that did not exhibit swelling.

(a) (b)

Figure 5.14 Plugged nozzles from test #7 (a) and test #9 (b).

5.3 Characteristic Velocity Efficiency

Nozzle erosion occurred for both test #8 and #9 making η_{C^*} measurements inaccurate based on initial throat diameter. The values presented in Table 5.3 for these tests are based on using the average of initial and final throat diameter in Eqn. 5.3.

The η_{C^*} for the tests is generally between 80-90%, values that suggest incomplete combustion or error in measuring m_{fu} expelled during combustion. The excess fuel that could have been expelled post test, for the grains that swelled, could cause the actual m_{fu} consumed during motor operation to be less than reported. Charring/combustion of the phenolic and high temperature RTV between the nozzle and phenolic could also have lead to higher values for m_{fu}. Thus, the actual η_{C^*} values are probably a little higher than those reported in Table 5.3.

The η_{C^*} of test #8 appears to deviate from the other tests. This particular test also exhibited abnormally strong axial swelling post test compared to what was observed in all other tests, see Figure 5.15. It is possible that this particular fuel grain had partially reacted prior to the test producing a lower η_{C^*} and resulting in excessive axial swelling.

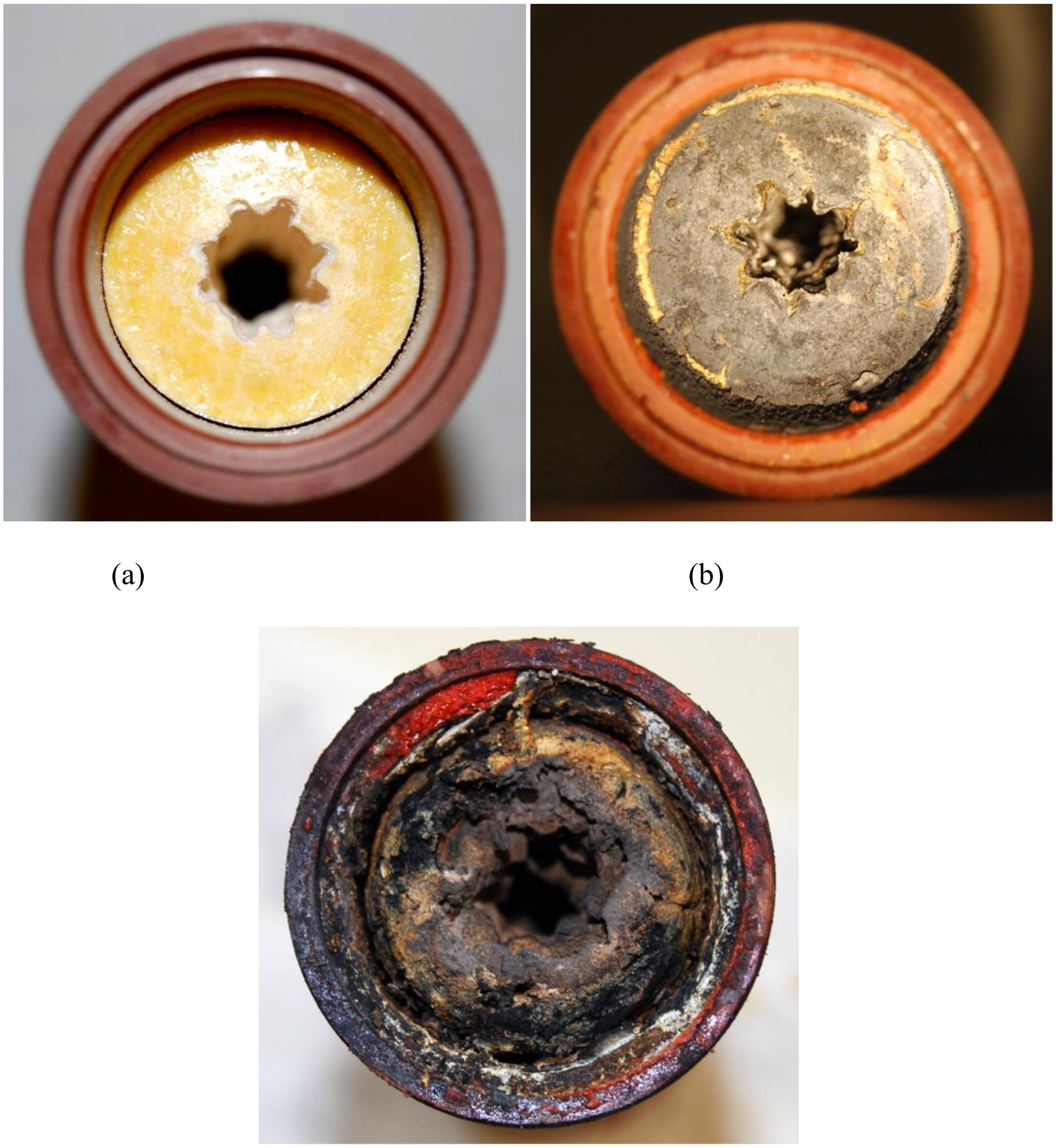

(a) (b)

(c)

Figure 5.15 Aft end of the fuel grain showing fuel grain axial expansion for test #4 before combustion (a) and tests #4 (b) and #8 (c) after combustion.

5.4 Hypergolic Ignition Behavior

Eight of the nine tests demonstrated successful hypergolic ignition. The t_{ign} varied from 0.529-1.450 s for tests that used a cavitating venturi. The range of t_{ign} appears to correlate to $\dot{m}_{ox}$ with shorter t_{ign} for higher $\dot{m}_{ox}$. The higher $\dot{m}_{ox}$ values caused the plumbing between the venturi and injector to fill and reach steady state operation faster, reducing the overall t_{ign}. Test #4, that did not have a cavitating venturi allowing the oxidizer to reach the injector quickly, produced the shortest t_{ign} with a value of 0.135 s, see Figure 5.4. The t_{ign} for test #4 is on par with or faster than other hypergolic hybrid combustors for which ignition data was available [12, 88, 89, 90, 91].

Test #5 did not achieve ignition. The fuel grain was used in a previous test and had been bored to remove most of the char and partially reacted layer exposing some pristine fuel surfaces. The injector used in this test had a higher spray angle, and the oxidizer flow rate was almost twice that of previous tests. Thus, impingement flux of liquid oxidizer at the head end of the grain was almost double that of all the other tests. The combination of a re-used fuel grain with not all pristine surface and the high impingement oxidizer rate are likely the reasons why test #5 did not ignite.

5.5 Regression Rate

The main method to determine regression rates was through the bulk mass method that was then validated using the geometrical method. Both methods produced similar results, see Table 5.5, with the geometrical method producing slightly higher values for $\bar{\dot{r}}$ and $\bar{G}_{ox}$. The geometrical method includes a single section of the fuel grain where $\bar{\dot{r}}$ and $\bar{G}_{ox}$ are the highest; the fuel regression rate varies down the length of the grain. All other sections in the fuel grain would provide similar or lower values, meaning that the geometrical method for the entire fuel grain and the bulk mass method provide values even closer than what is reported suggesting that both methods are valid for analyzing the data. The remaining analysis is for $\bar{r}$ values determined using the bulk mass method.

Table 5.5 Regression rate and oxidizer flux values determined by bulk mass and geometrical methods for a couple of tests.

Test I.D.	Bulk Mass Method $\bar{r}$, in/s	Geometrical Method $\bar{r}$, in/s	Bulk Mass Method $\bar{G}_{ox}$, lb/in^{2}s	Geometrical Method $\bar{G}_{ox}$, lb/in^{2}s
4	0.00456 ±0.00001	0.0055	0.153 ±0.026	0.1639
6	0.00928 ±0.00001	0.0102	0.276 ±0.018	0.2830

The regression rate of the fuel did not exhibit a strong oxidizer flux dependence typical of hybrid rockets, see Figure 5.16, but instead exhibited a strong pressure dependence, see Figure 5.17. Conducting a least squares analysis of the data provides the equation,

$$\bar{r} = 1.16x10^{-6} G_{ox}^{0.13} p_c^{1.61} \tag{5.10}$$

with an R^2 of 0.97, G_{ox} in lb/in^{2}s, and p_c in psi. The strong pressure and weak flux dependence is uncommon even for hypergolic hybrid rockets. Those experiments that have exhibited pressure dependence typically have a pressure exponent of 0.6 or less and a flux exponent of 0.5 or less with the regression rate becoming strictly flux dependent at pressures above 300-400 psi [10, 18, 92]. One experiment produced a regression rate pressure dependence exponent of 0.78 [8]; however, this is still notably lower than the value produced by the present experiments. The near non-existent regression rate dependence on flux along with the strong pressure dependence suggests that the mechanisms dominating the combustion behavior differ dramatically from what has been historically observed. These results would suggest that the partially reacted layer and hypergolic reactions are significantly influencing the combustion behavior as these two factors are not typically present in hybrid rocket combustors. If the observed trends are consistent at high pressures, then fuel regression rates higher than what has been achieved in the past are possible.

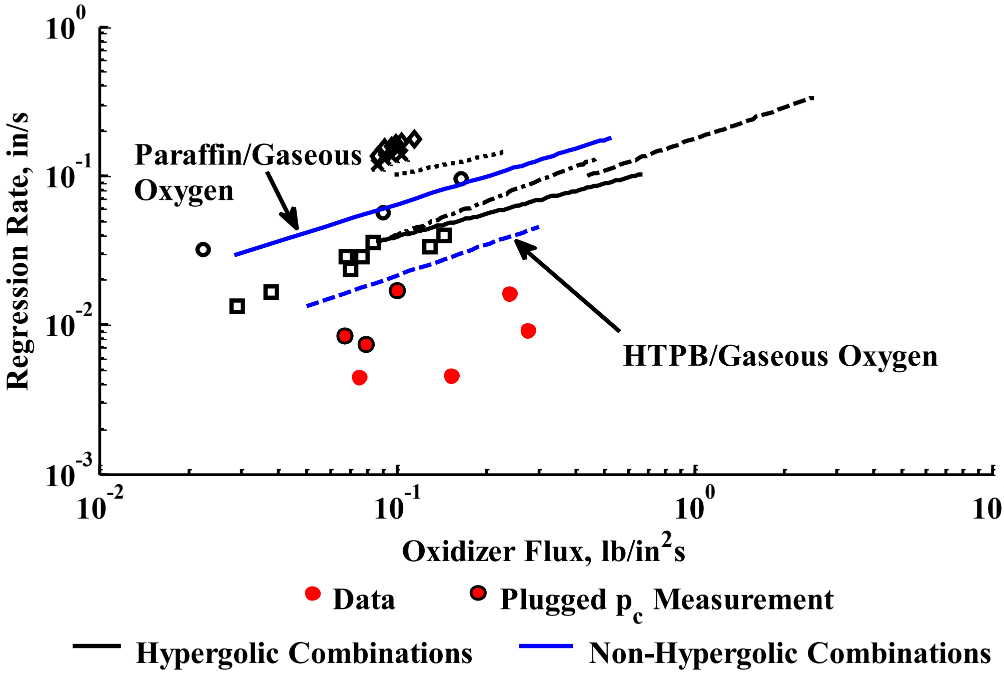

Figure 5.16 Regression rate of experimental fuel and other fuels as a function of $G_{ox,avg}$.

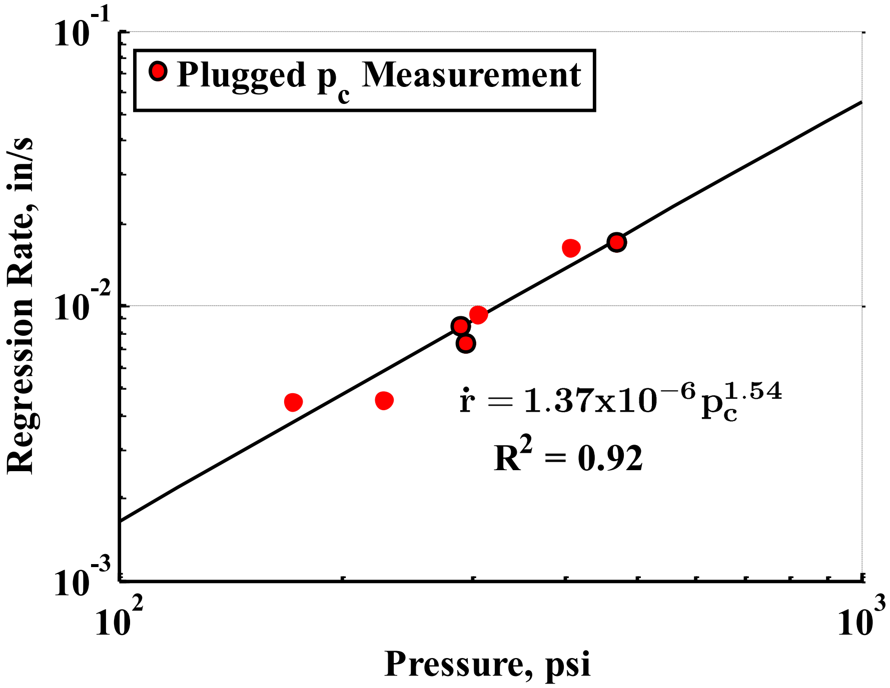

Figure 5.17 Regression rate of experimental fuel as a function of $p_{c,avg}$.

The regression rate varied down the length of the fuel grain and varied with grain length, see Figure 5.18 (6.24 in long grain) and Figure 5.19 (12.54 in long grain). The regression rate at the head end, immediately adjacent to the injector, is initially high and tapers down to a lower rate further downstream, a behavior consistent for both the long and short grains and common for hybrid rocket combustors in general. The regression rate for the short grain appears to remain constant for the rest of the grain length, whereas the long grain exhibits higher regression rates towards the aft end of the motor.

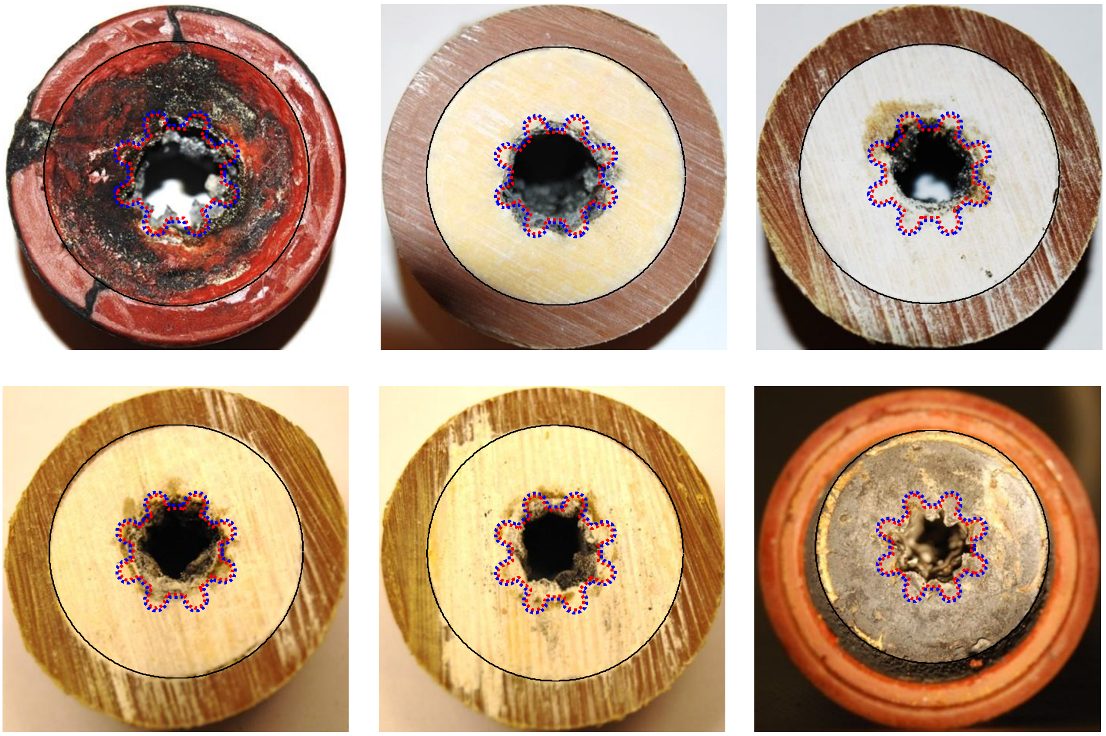

Figure 5.18 Sectioned fuel grain from test #4. The red dashed line indicates the initial fuel surface, whereas the blue indicates the final fuel surface based on a surface normal fuel regression. The distances of the section face from the head end of the fuel grain, starting in the upper left corner and going left to right, are -0.25, 1.44, 2.94, 4.44, 5.75, and 6.24 in.

Figure 5.19 Sectioned fuel grain from test #6. The red dashed line indicates the initial fuel surface, whereas the blue indicates the final fuel surface based on a surface normal fuel regression. The distances of the section face from the head end of the fuel grain, starting in the upper left corner and going left to right, are -0.25, 1.50, 3.50, 5.63, 7.88, 10.06, 12.69, and in.

The regression rate data also suggests that the combustion behavior is slightly different for the two grain lengths, see Figure 5.20. The flux dependence of the short grains is nearly non-existent with a slightly negative exponent while the longer grains exhibit a little higher flux dependence with an exponent of 0.31. Likewise, the pressure dependence exponent increases from 1.42 for the short grain to 2.04 for the long grain. The combination of these observations suggests that the combustion process towards the head end of the long grains has negligible flux dependence and notably high pressure dependence while the aft end of the grain exhibits increased flux and pressure dependence. At this point, it is difficult to identify what mechanisms are becoming more dominant towards the aft end of the motor. It is possible that the higher velocities and flux levels experienced at the aft end of the motor are stripping off the partially reacted layer (if present) allowing for more hypergolic reactions (if occurring). It is also possible that less liquid oxidizer is able to reach the aft end of the motor, reducing the influence of the hypergolic reaction on the combustion behavior. These mechanisms will be investigated further in the following chapter.

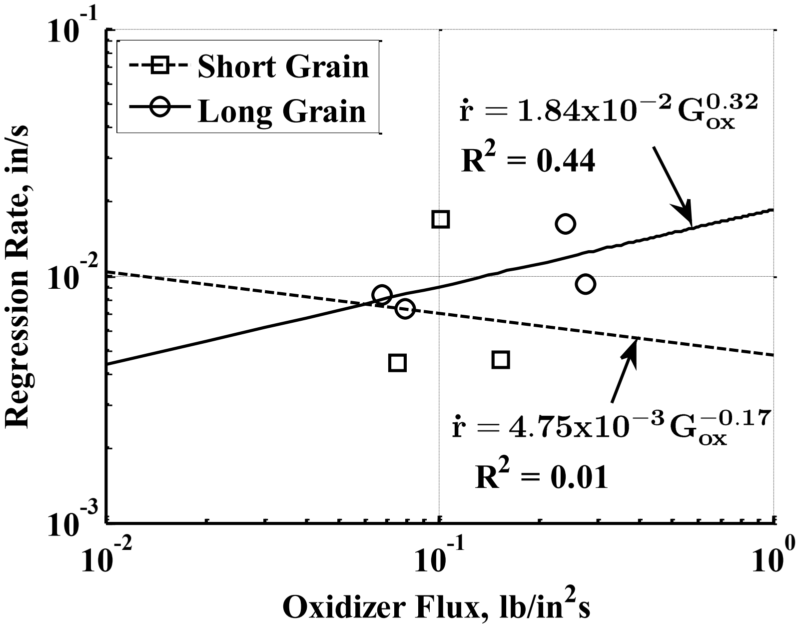

(a)

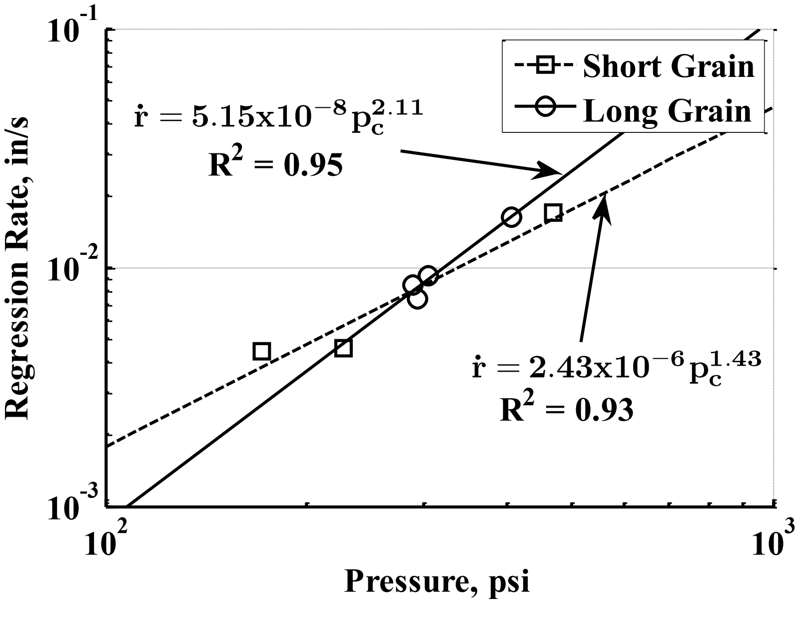

(b)

Figure 5.20 Regression rate of experimental fuel divided into short (~6 in) and long (~12 in) fuel grains as a function of (a) $G_{ox,avg}$ and (b) p_c.

It is apparent, from the images in Figure 5.18 and Figure 5.19, that a layer of char and thermally modified/partially reacted material is present on the surface of the fuel grain: a behavior similar to what was observed in the opposed burner experiments, see Section 4.4. Comparison of the location of the combusted fuel surface with the original fuel surface (the red dashed lines) emphasizes the formation of a partially reacted layer that swells, as the combusted fuel surface is smaller than the original, see Figure 5.18. Removal of the swelled layer, through polishing with water, shows that the unreacted fuel surface can be deep under the partially reacted layer, see Figure 5.21. The thickness of the layer is thin at the head end and increases down the length of the fuel grain; probably the result of the head end experiencing cooler average combustion chamber temperatures and quicker cooling as cool nitrogen purge gases encounter the head end first. Purge gases become heated before reaching the aft end of the fuel grain length where hot combustion temperatures prevailed allowing for more heat transfer into the fuel grain and increased swelling. This swelling probably also occurs post combustion, whereas the actual thickness of this partially reacted layer, during combustion, is similar to what is observed near the head end of the fuel grain.

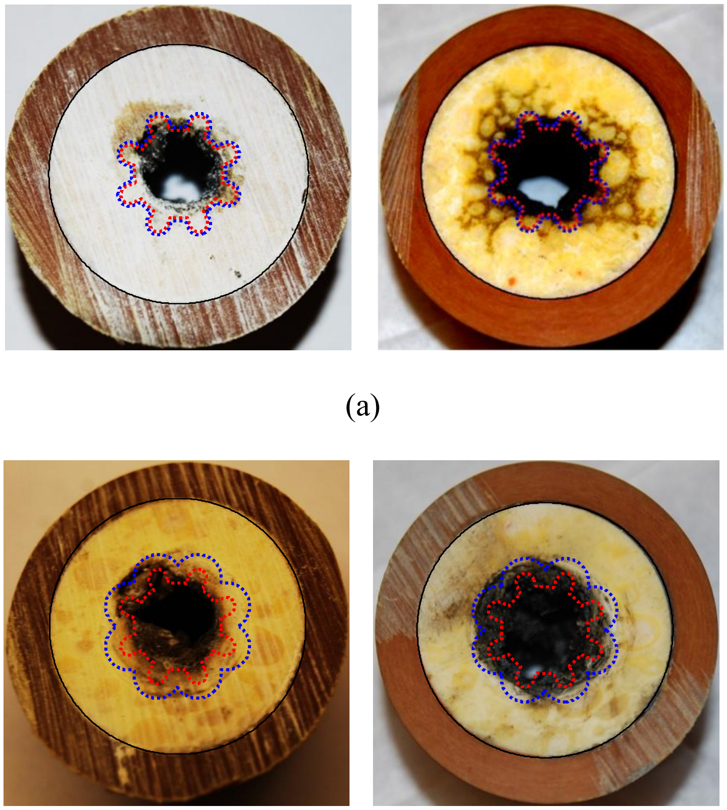

(a)

(b)

Figure 5.21 Sample fuel grain sections from test #4 (a) and test #6 (b). The images on the left are as cut and the images on the right are the same samples after polishing. The distances of the section face from the head end of the fuel grain are 2.94 in for (a) and 5.63 in for (b).

Due to the difficulty in determining the fuel port perimeter after combustion, the fuel flow rate,

$$\dot{m}_{fu} = \frac{m_{fu}}{t_b} \tag{5.11}$$

behavior was investigated to determine the controlling mechanisms. The $\dot{m}_{fu}$ was normalized by the fuel grain length, as the combustion mechanisms should be relatively constant down the length of the grain, and then plotted as a function of oxidizer flux and chamber pressure, see Figure 5.22. The trends of these results and those found using the regression rate method are almost identical, exhibiting similar exponents and R^2 values. This suggests that the previous observations made are correct and that pressure is the most influential component of the combustion behavior.

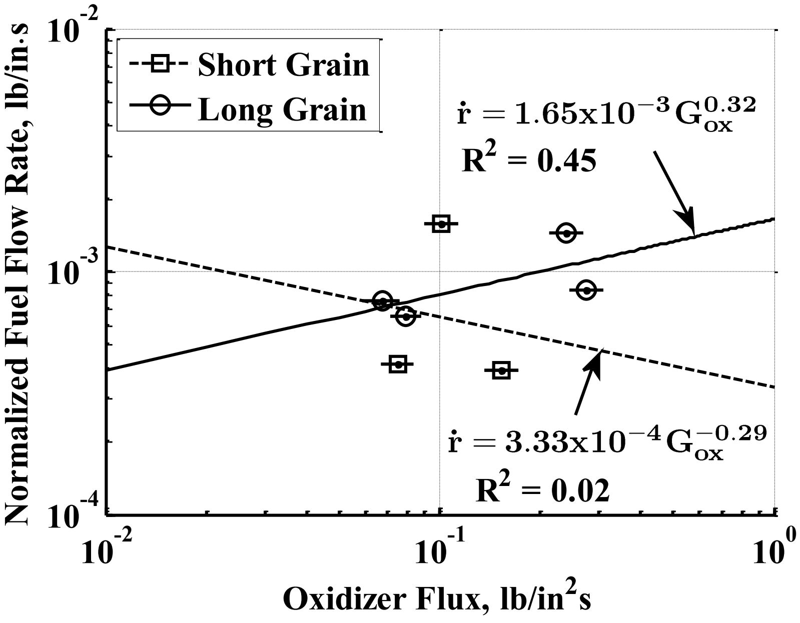

(a)

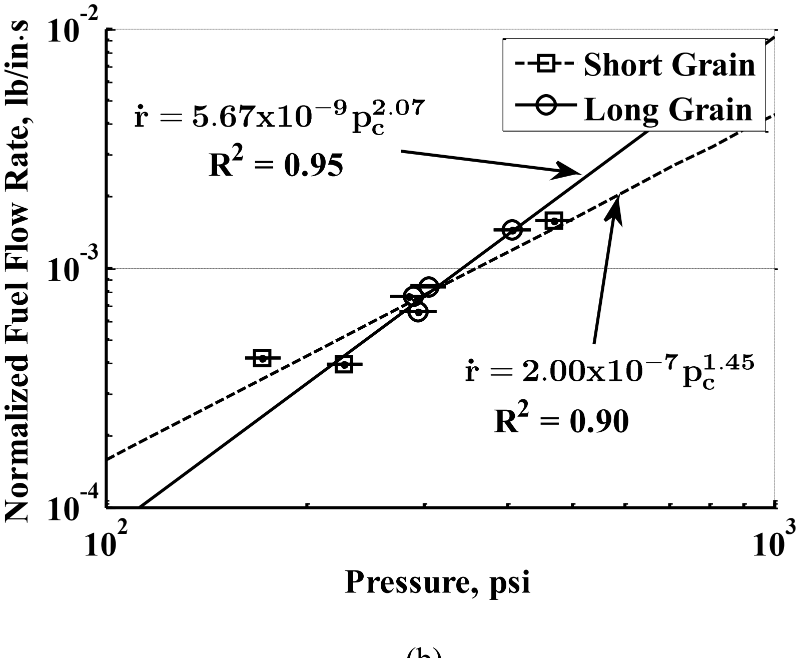

(b)

Figure 5.22 Fuel flow rate normalized by fuel grain length as a function of (a) $G_{ox,avg}$ and (b) p_c. The horizontal bars at every data point is the range of uncertainty of the measurement.

CHAPTER 6. MODELING COMBUSTION BEHAVIOR

Combustion within a rocket can be a complex and varied process, making it challenging to identify which mechanisms dominate. In the current hypergolic hybrid combustor, several reactions that influence combustion behavior can occur simultaneously, such as a turbulent diffusion flame, radiative and convective heat transfer, liquid oxidizer evaporation and transport, hypergolic reactions, and the development of a partially reacted layer and char on the fuel surface. In this chapter, the classical model for general hybrid rocket combustion will be reviewed. However, as this theory fails to fully characterize the observed combustion behavior, we will evaluate in further detail the effects of flame kinetics, radiation, hypergolic reactions, and the partially reacted foam layer on the combustion behavior and resulting regression rate of the hypergolic hybrid rocket tests discussed in CHAPTER 5.

6.1 General Hybrid Rocket Combustion Theory

General hybrid rocket combustion theory suggests that fuel regression rate is highly dependent primarily on the convective heat transport from the flame to the fuel surface in the following manner,

$$\dot{r}\rho_{fu}h_v = (0.03)\left(\frac{\mu}{x}\right)^{0.2} G_{ox}^{0.8}\left(\left(\frac{v_e}{v_b}\right)\left(\frac{\Delta h}{h_v}\right)\right)^{0.32} h_v \qquad (6.1)$$

which can be further simplified to,

$$\dot{r} = C_0 G_{ox}^{0.8} \tag{6.2}$$

where ρ_{fu} is the fuel density, h_v is the energy required to raise the initial fuel temperature, T_0, up to the fuel surface temperature, T_s, and convert the condensed phase fuel into gas, μ is the viscosity of the combustion gases, x is the distance down the fuel port, v_e is gas velocity at edge of boundary layer, v_b is gas velocity at the flame, Δh is the difference in enthalpy between the flame and gas phase species at the condensed phase interface, and C_0 is a constant. This form was originally derived by Marxman and Gilbert [93] and further expounded on by Altman [94]. Pressure exhibits little to no influence on the regression rate according to this traditional derivation.

However, it is important to note that this classical model fails to fully describe the observed combustion behavior of the current experiments which clearly demonstrated a high dependence on pressure. This suggests that the potential mechanisms associated with our combustor environment, mentioned above, combine to produce unique and unprecedented combustion behavior using our novel fuel. The remainder of this chapter will be devoted to evaluating theory on each likely process and evaluate its influence on overall combustion behavior to elucidate on which process is most likely the dominate mechanism.

6.2 Flame Kinetics

Classically, two regimes have been identified in hybrid rockets where pressure dependence is possible; one is at high flux levels and low pressures, where flame kinetics become important, and the other is at low flux levels, where radiation becomes important, see

Figure 6.1. We will first investigate the potential of flame kinetics producing the observed combustion behavior in the current experiments.

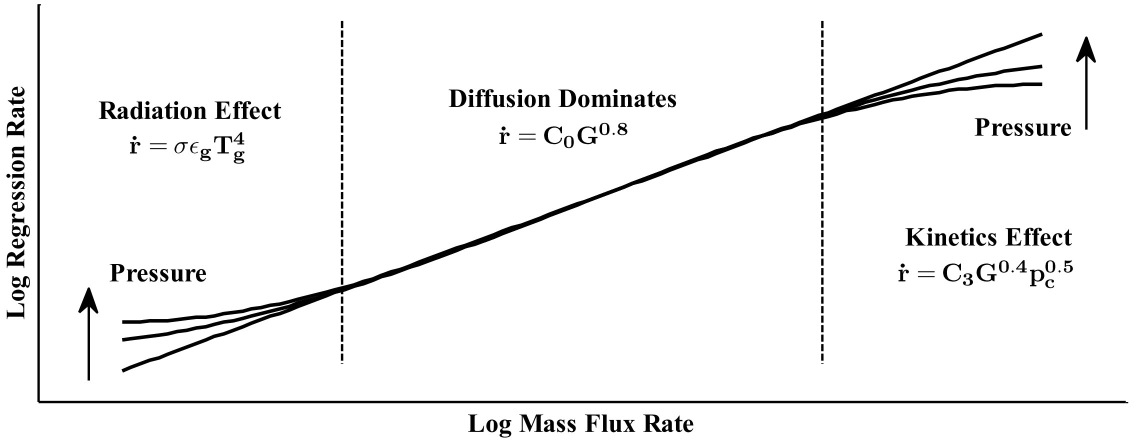

Figure 6.1 Classical hybrid rocket regression rate behavior as a function of material flux level down the fuel port. Figure has been modified from original [94].

At high flux levels and low pressures, the rate of species transport increases and can become faster than flame reaction kinetics, causing the diffusion flame reaction zone to broaden. The broadening flame zone results in less heat transfer to the fuel surface and thus lower regression rates compared to when flame kinetics are faster than the rate of species transport. Thus, the kinetics of the flame zone, and therefore pressure, begin to exert influence on the regression rate of the fuel. As pressure increases, the kinetics of the reaction will increase, once again resulting in the transport of species becoming the limiting factor and the classical flux dependence regression rate, see Eqn. 6.1.

Wooldridge and Marxman [95] developed an analytical model for this regime of competition between diffusion and reaction kinetics by comparing the time scales related to turbulent species transport and chemical kinetics. They arrived at the following form,

$$\theta_t = C_1 \frac{l_1(\mu/x)^{0.2} G^{0.8} B^{0.32}}{l_2 p_c^{n/2} T_f^{1+n/2} e^{-E/RT_f}} \tag{6.3}$$

and,

$$\dot{r} = \dot{r}_0 \left(\frac{2}{\theta_t}\right)^{0.5} \left[1 - \frac{1}{\theta_t}\left(1 - e^{-\theta_t}\right)\right]^{0.5} \tag{6.4}$$

where θ_t is a ratio of diffusion over kinetic time scales, C_1 is a constant, l_1 is the characteristic flame length, l_2 is the characteristic mixing length, T_f is the flame temperature, n is the global chemical reaction order, E is the activation energy of the kinetic reaction, R is the gas constant, and $\dot{r}_0$ is the original regression rate from classical flux dependence, see Eqn. 6.1. As pointed out by Altman and Humble [94], for high fluxes and low pressures (θ_t is large) and assuming a gas phase reaction order of 2, the equations reduce to,

$$\dot{r} = C_2(0.03)\left(\frac{\mu}{x}\right)^{0.2} G_{ox}^{0.4} B^{0.32} p_c^{0.5} \tag{6.5}$$

which can reduce to the form,

$$\dot{r} = C_3 G_{ox}^{0.4} p_c^{0.5} \tag{6.6}$$

where C_2 and C_3 are constants.

Such a regression rate behavior has been observed experimentally [10, 18, 92] and is a likely explanation for the similar flux and pressure dependence exponents measured in those experiments. It is possible to match the pressure exponent of Eqn. (5.10 if a 6th Tf (6.3. However, such a gas phase reaction order is highly unlikely. The lack of flux dependence of Eqn. (5.10 is another discrepancy with gas phase kinetic theory. Furthermore, the observed gas phase kinetic effects of previous experiments tend to diminish at pressures above 400 psi, whereas the current experiments appears to continue to demonstrate a strong pressure dependence above 400 psi. These trends suggest that gas phase kinetics is not the dominant mechanism controlling combustion behavior in the current experiments.

6.3 Radiation Effects

Radiative heat transfer could be a plausible explanation why a strong pressure dependence is observed in the present experiments ($\dot{r} = 1.16x10^{-6} G_{ox}^{0.13} p_c^{1.61}$), especially since there is little apparent convective heat transfer to the fuel surface. It has been noted that this situation can arise in hybrid rocket combustion when flux down the fuel port is low, resulting in weak convective heat transport and therefore heat transfer being dominated by radiation [92, 94]. Such flux levels are typically notably lower than values in the current experiments, suggesting it is unlikely that this phenomena is producing the observed pressure dependence. The presence of a partially reacted layer on the fuel surface, see Section 5.5, could potentially inhibit the convective heat transfer, making radiative heat transfer dominance possible. Under this assumption, a radiative analysis follows to provide a sense of the amount of radiative heat transfer would be possible if it was the sole means of heat transfer.

According to Incropera et al., gas phase radiative heat transfer, $\dot{q}_r$, can be modeled as,

$$\dot{q}_r = \sigma \varepsilon_g T_g^4 \qquad (6.7)$$

where $\dot{q}_r$ is the radiative heat transfer, σ is the Stefan-Boltzmann constant, T_g is the gas temperature, and ε_g is the gas emissivity given by the form,

$$\varepsilon_g = \int_0^{\infty} 1 - e^{-\kappa_\lambda L} d\lambda \tag{6.8}$$

where κ_λ is the absorption coefficient of the gas, λ is the wavelength, and L is mean beam path through the gas [96]. Son and Brewster [97] used this form in calculating gas phase emission heat transfer in a solid rocket motor and computationally determined the amount of radiation produced by the gas based on the emission spectra of the species present in the gas and produced the correlation provided in Figure 6.2.

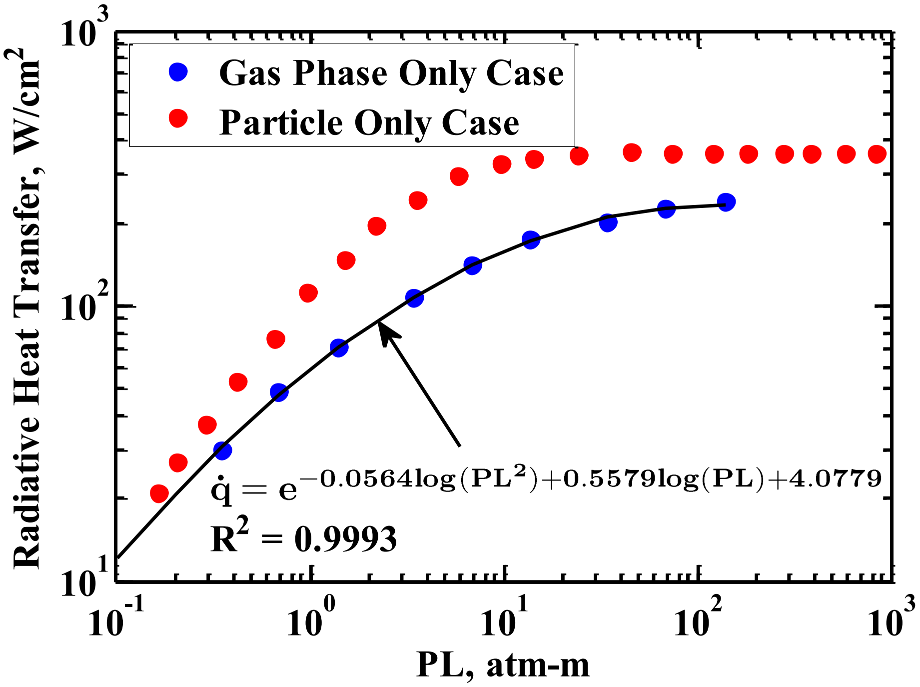

Figure 6.2 Radiation from gas phase and solid particulate as a function of pressure and L and an equation fitting the data. Adapted from provided by Son and Brewster [97].

Assuming the current propellant combination has similar gas phase species and temperatures in the flame zone, the same correlation can be used to determine the amount of radiative heat transfer occurring as a function of the product of p_c and L. This is a reasonable assumption as the most dominant emitting product species in the 88% AP/12% HTPB combination used by Son et al. and the nitric acid and EDBB/ferrocene/epoxy combination are very similar with the major differences being the lack of HCl and the presence of boron products in low concentrations for the latter combination. According to the calculations of Son et al., the HCl contributes little to the radiation. The flame temperature used by Son et al. was 2800 K, whereas stoichiometric flame temperatures of the nitric acid and EDBB/ferrocene/epoxy combination is 3000-3100 K; however, it is likely that the actual diffusion flame temperature is lower due to dilution by cooler fuel, oxidizer, and product species. Comparison of spectral intensity as a function of wavelength of the two main fuel components from each propellant combination, HTPB end EDBB, reacting with oxygen have similar profiles with HTPB having a slightly higher intensity, see Figure 4.15. These observations suggest that the radiative heat model produced by Son et al. can produce reasonable values for the current experiment.

Son and Brewster assumed an isothermal core when determining their value for L, making L equivalent to the diameter of the motor [97]. This is not a valid assumption in a hybrid rocket motor as a comparatively cool core of oxidizer mixed with products occupies most of the combustor with the location of high temperatures located near the fuel surface in the diffusion flame region where the dominant radiative heat transfer is produced. Assuming the flame is 1 mm thick and 1 mm from the surface of the fuel, L can be calculated based on the following equation,

$$L = 4V/A \tag{6.9}$$

where V is the volume of the emitting gas and A is the surface area of the fuel. This produces a value of L = 0.0038 m. However, this method of calculating L assumes no interfering media between the gas volume and the fuel surface, a condition that is not met in the hybrid combustor due to the relatively cool core flow down the center of the fuel port, resulting in an overly high estimate for L. Another method of calculating L is assuming the flame and fuel surface behave as two infinite parallel plates resulting in $L = 1.8z$, according to Incropera et al. [96], where z is the flame distance from the fuel surface. Assuming again a distance of 1 mm for the flame distance from the fuel, a value of L = 0.0018 m is produced, which is roughly half of that obtained by using the volume of the emitting gas to determine L. In reality, the actual value for L is probably between 0.0018 and 0.0038 m; therefore, the values of L from the two methods is averaged producing L = 0.0028 m.

To implement the radiation model, it is assumed that all of the fuel regression is caused by $\dot{q}_r$ according to,

$$\dot{r}\rho_{fu}h_v = \dot{q}_r. \tag{6.10}$$

The remaining unknown in this model is a value for h_v. As epoxy is similar to HTPB, the h_v for the epoxy part of the fuel uses the value found by Lengelle for HTPB burning in a hybrid motor with a flux of 16 g/cm^2, h_v = 745 cal/g [86]. The h_v for EDBB was estimated to be 400 cal/g, see Section 4.5. Thus a mass average value of h_v = 470 cal/g is used in the current model.

The radiative model produces the results provided in Figure 6.3. The resulting regression rate is roughly 4-10 times less than what was measured in the combustor, and while the model does produce a regression rate that is notably pressure dependent, the pressure exponent is half of what was observed in experiments. It is also unlikely that the calculated amount of radiation used in this model is actually reaching the pristine fuel surface and contributing to fuel regression. As stated earlier, for radiative to dominate over convective heat transfer, it is likely that the layer of partially reacted material on the fuel surface is producing a thermal insulator that inhibits convective heat transfer. The char on the surface of that layer will also act like a black body and absorb almost all of the radiation from the flame. It is true that the char layer will then radiate heat towards the pristine fuel, but char temperatures are probably around 1000 K meaning the radiative heat transfer will be several orders of magnitude less than what the flame zone is transmitting. As discussed below, it is also likely that liquid oxidizer is present between the hot flame zone and the fuel surface providing further, albeit small, radiative impedance. It is thus unlikely that radiation has a notable influence on the regression rate of the fuel.

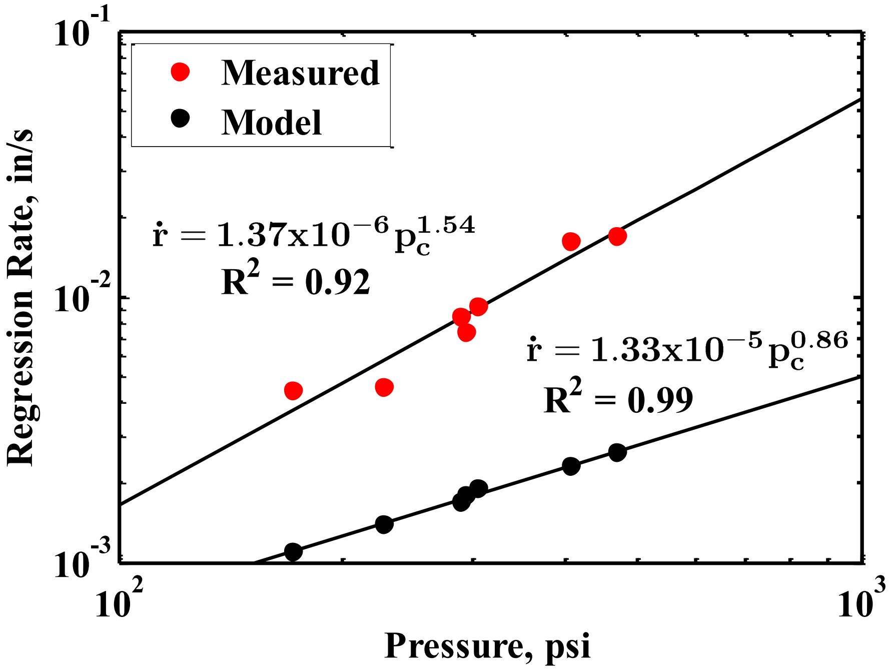

Figure 6.3 Radiation model results.

6.4 Pressure Dependent Hypergolic Reactions

Hypergolic reactions between the oxidizer and fuel are a possible explanation as to why a strong pressure dependence is observed in the regression rate data. Hypergolic reactions can involve various steps in the reaction including condensed/condensed, condensed/gas, and gas/gas phase reactions. Each of these reaction types and their application to the present experiments will be addressed.

In order for liquid phase hypergolic reactions to occur, liquid oxidizer needs to be present at the fuel surface. This could occur through convective transport or by direct impingement of injector spray onto the fuel surface. To determine if the latter is possible, a simplified

1-D droplet evaporation model was derived to determine the life time of a liquid oxidizer droplet, t_{evap}, and the time it would take for such a droplet to reach the end of the longer fuel grains, t_x. The details of the model are provided in Appendix D, whereas the results are provided in Table 6.1, where T_∞ is the average combustor temperature that the droplet will experience and $D_{0,drop}$ is a droplet's initial diameter. The time given for t_x is for the slowest injection velocities. The times would suggest that the larger droplets will reach the aft end of the fuel grain, indicating that it is likely that liquid oxidizer droplets are reaching the fuel surface along the entire length of the fuel grain.

Table 6.1 Evaporation times for several sizes of nitric acid droplets and average combustor temperatures along with the time for a droplet to reach the end of the combustor.

T_∞, K	$D_{0,drop}$, μm	t_{evap}, ms	t_x, ms
500	30	18.7	30.4
1000	30	3.9	30.4
500	100	207.3	30.4
1000	100	43.5	30.4

Liquid oxidizer/solid fuel reactions are possible in the present system, especially since there is a high probability that liquid oxidizer is impinging on the fuel surface. The hypergolic reaction kinetics of such an interaction are not likely to exhibit a strong pressure dependence due to the condensed phase state of both propellants. Pressure dependence in chemical kinetics typically arises in gas phase reactions as the concentration of a gas can vary linearly with pressure, assuming ideal gas law. It is possible that adsorption of the liquid oxidizer onto the solid fuel surface could influence the overall reaction kinetics; however, condensed phase adsorption onto condensed phase again does not exhibit strong pressure dependence. It is thus unlikely that purely condensed phase reactions will contribute to the pressure dependence observed in the combustion behavior of the present experiment.

Heterogeneous reactions between gaseous oxidizer and the surface of the solid fuel are a possible source for pressured dependent regression rates. These particular reactions have been investigated analytically by several researchers with emphasis on heterogeneous reaction kinetics [43] or adsorption of the oxidizer onto the fuel surface [51] as the rate limiting processes. Smoot et al. showed through a 1-D analysis, using energy and species conservation, that an analytical solution could be found for an nth order heterogeneous reaction combined with a convective environment [43]. For most of their calculations they assumed a 1st order heterogeneous reaction, common for combustion processes. They also used the Chilton-Colburn analogy of heat and mass transfer to simply the equations. The solution provided a complex relation for the regression rate as a function of various parameters including pressure and total flux. This complex relationship was further simplified by Smoot et al. by assuming that the temperatures at the fuel surface and turbulent diffusion flame are similar; a possible situation if the amount of fuel and oxidizer that react heterogeneously is high enough such that the products from this reaction dilute the temperature of the turbulent diffusion flame. Making this assumption, the following form was obtained,

$$\dot{r} = \frac{C_4 C_5 G_{ox}^{0.8} p_{ox,\infty}}{C_4 G_{ox}^{0.8} + C_5 p_c} \tag{6.11}$$

where $p_{ox,\infty}$ is the free stream oxidizer partial pressure and C_4 and C_5 are constants. Assuming that the free stream flow is mostly oxidizer, it can be seen that for high G_{ox}, the regression rate becomes linearly dependent with p_c, whereas for low G_{ox}, the regression rate becomes independent of p_c. The adsorption analyses, of gaseous oxidizer being adsorbed onto the fuel grain, presented by Rastogi and Deepak [51] produces a similar result of the form,

$$\dot{r} = \frac{C_6 p_c^m}{1+C_7 p_c^m} \tag{6.12}$$

where C_6 and C_7 are constants and m is an index between 0 and 1, the main difference being the lack of G_{ox} dependence.

Both of these analyses inherently assume that if a turbulent diffusion flame exists, the fuel first reacts with the oxidizer present at the fuel surface. Any remaining fuel or products from the heterogeneous reaction are then fully reacted to combustion products in the turbulent diffusion flame. While such a situation is conceivably possible, it is a concept that contradicts that traditional assumption that indicates that oxidizer will first react in the turbulent diffusion flame leaving little oxidizer if any to reach the fuel surface. Despite the uncommon assumption needed for Eqns. 6.11 and 6.12 to be valid, there are experimental values for hybrid rockets that would support such a theory. Several researchers have found hypergolic combinations with regression rates having pressure dependent exponents of 0.4-0.6 [10, 17, 18, 98]. Such pressure exponents are also consistent with the kinetic flame theory mentioned in Section 6.2, suggesting that typical flame kinetics could also be the limiting factor in these systems and not condensed/gas phase reactions.

If the more traditional assumption is correct, it is still possible, with the current experiments, that oxidizer is reaching the fuel surface due to the evaporation rate of liquid nitric acid. As a result, Eqns. 6.11 and 6.12 still have some applicability to the current experiments, assuming heterogeneous hypergolic reactions are responsible for the observed pressure dependence. However, Eqns. 6.11 and 6.12 predict a regression rate that is linearly or less pressure dependent, indicating that heterogeneous condensed fuel/gaseous oxidizer hypergolic reactions are probably not responsible for the observed combustion behavior in the current experiments.

The other possibility associated with hypergolic reactions is a gas/gas phase reaction located between the fuel surface and the turbulent diffusion flame. In this particular case, if most of the fuel reacts with the turbulent diffusion flame, leaving little oxidizer to react hypergolically in the gas phase, the traditional hybrid combustion theory will prevail with the regression rate being primarily flux dependent. On the other hand, if the fuel primarily reacts with the oxidizer in a hypergolic reaction, located between the fuel surface and turbulent diffusion flame, then turbulent transport of oxidizer and turbulent mixing along with the hypergolic gas phase kinetics influence the regression rate. The dynamics of turbulent transport versus gas phase kinetics result in the same arguments that were used for the kinetic flame theory discussed in Section 6.2. Thus, the governing principles for when gas phase kinetics dominates is once again provided by Eqn. 6.6. As this relationship again only exhibits regression rate with a $G_{ox}^{0.4}p_c^{0.5}$ dependence, it is unlikely that gas phase hypergolic reactions are responsible for the observed combustion behavior in the present experiments that has the form $\dot{r} = 1.16x10^{-6}G_{ox}^{0.13}p_c^{1.61}$.

6.5 Partially Reacted Foam Layer

The remaining aspect to investigate is the influence of the partially reacted layer on the combustion process. During combustion at atmospheric conditions, the partially reacted layer exhibits characteristics of foam in that gas is generated that causes an apparent liquid melt layer to expand, forming pockets of gas. Eventually, the layer solidifies producing a porous, foam like media, see Section 4.5 for further details on this behavior. Assuming that the decomposition behavior of the fuel is similar in the combustor experiments, the partially reacted layer can be modeled as a foam. Foam is used for a variety of reasons throughout industry; one main reason is its excellent properties as a thermal insulator. Thus a foam layer on the fuel surface could produce a low conductivity thermal insulating layer between the turbulent diffusion flame and the fuel surface, see Figure 6.4. The presence of the foam layer could notably influence the heat transfer to the fuel surface causing the regression rate to decrease.

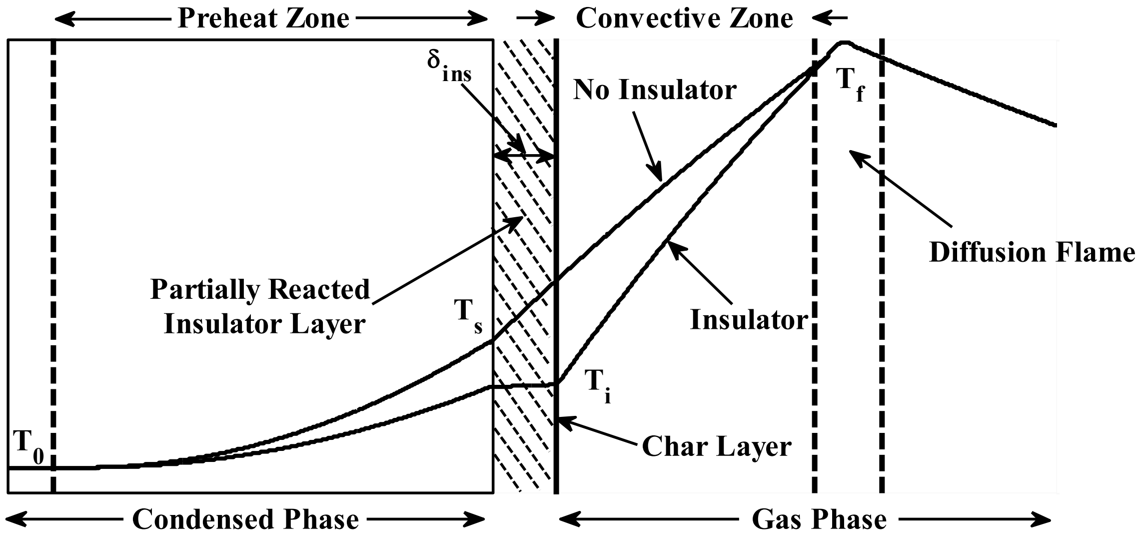

Figure 6.4 A schematic depicting the relative temperature profiles of a solid hybrid fuel burning with and without a partially reacted foam layer that behaves as an insulator. The distance between the fuel surface and the turbulent diffusion flame may not be the same for a fuel with and without a foam layer, but for simplification, they are portrayed to have the same distance.

The fuel regression rate behavior can be approximated, for the scenario proposed in Figure 6.4, by performing an energy balance between the fuel preheat zone and the combination of the partially reacted layer and the convective zone. The heat transfer through the partially reacted layer and the convection zone can be modeled using a thermal circuit analysis, as it is assumed that no heat generation occurs in these regions. Such an analysis produces,

$$\dot{m}_{fu} c_{p,fu} (T_s - T_0) = \left(T_f - T_s\right) A_s \left[\frac{1}{h_{conv}} + \frac{\delta_{ins}}{k_{ins}}\right]^{-1} \tag{6.13}$$

where δ_{ins} and k_{ins} are the thickness and apparent thermal conductivity, respectively, of the partially reacted insulating layer.

The apparent thermal conductivity of a foam layer is a combination of thermal conductivity through the solid structure, convective heat transfer through the gas pockets throughout the solid structure (this can become solely conduction through gas assuming the gas within the pockets does not move and ignoring buoyancy effects), and radiation between the many surfaces throughout the porous structure. According to Glicksman, the influence of radiation is most pronounced in very low density foams but becomes negligible as foam density increases [99], see Figure 6.5. The influence of radiative heat transfer also diminishes as the gas cell diameters, within the foam, decrease, see Figure 6.6. The cell size in a 100% EDBB pressed pellet is on the order of magnitude of 100 μm or less at atmospheric conditions, see Figure 6.7, and can be even smaller when EDBB burns with a binder, see Section 4.5. These cell sizes will decrease in size as pressure increases, reducing the influence of radiation. Assuming the fuel in the current experiments exhibits similar trends as the foams presented in Figure 6.6, it is likely that radiative heat transfer does not significantly influence the total thermal conductivity of the partially reacted layer and only solid and gas conduction are important.

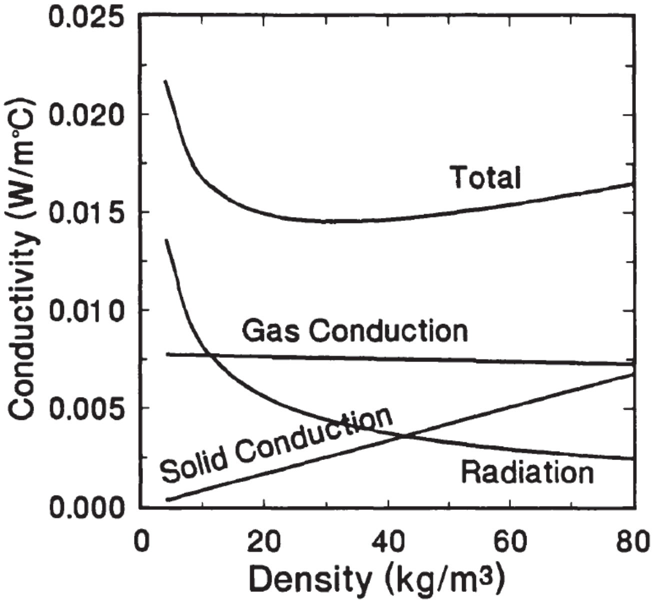

Figure 6.5 Total apparent thermal conductivity (including solid conduction, gas conduction, and radiative heat transfer mechanisms) of a foam as a function of foam density. Taken from Glicksman [99].

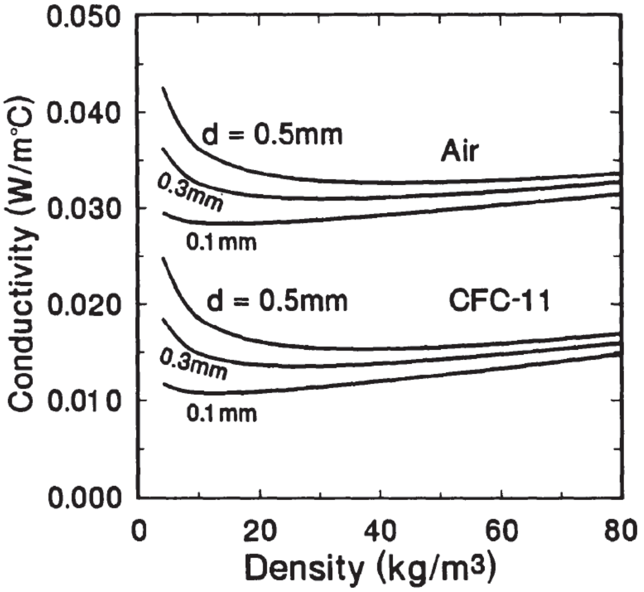

Figure 6.6 Total apparent thermal conductivity of some foam as a function of gas cell diameter and the gas used to produce the foam (air or CFC-11). Taken from Glicksman [99].

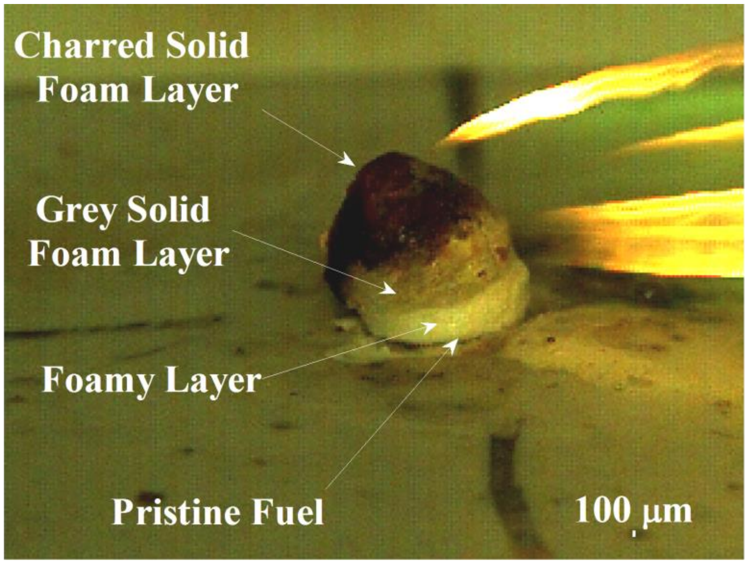

Figure 6.7 The foaming behavior of a 100% EDBB pressed pellet burning with atmospheric air. The flame protruding off to the right is caused by convective air flow present in the fume hood.

According to Glicksman [99], the total thermal conductivity of a foam layer, k_{foam}, neglecting radiative heat transfer, will have the form of,

$$k_{foam} = k_{ins} = \gamma k_{gas} + \frac{1-\gamma}{3} k_c \left[f_s \left(\frac{a}{b}\right)^{0.5} + 2(1-f_s)\left(\frac{a}{b}\right)^{0.25} \right] \quad (6.14)$$

where k_{gas} is thermal conductivity through the gas phase, k_c is thermal conductivity through condensed phase, γ is volume fraction of gas to total foam volume, f_s is the fraction of condensed phase in struts (the physical region where cell walls intersect), a is the gas cell major axis, and b is the gas cell minor axis. It can be assumed that $k_p \gg k_{gas}$ given that the thermal conductivity of ammonia borane (a chemical similar to ethylenediamine bisborane) has a thermal conductivity of 15-35 W/mK for temperatures between 320-420 K [100], whereas the thermal conductivity of hydrogen gas is 2 orders of magnitude lower and all other gases are typically 3 orders of magnitude lower. This assumption combined with the assumption that the ratio of cell dimensions, $\frac{a}{b}$, does not vary with foam volume such that $\left[f_s\left(\frac{a}{b}\right)^{0.5} + 2(1-f_s)\left(\frac{a}{b}\right)^{0.25}\right] = C_8$, where C_8 is a $-fsab0.25$ (6.14 to,

$$k_{ins} = C_8 \frac{1-\gamma}{3} k_c. \qquad (6.15)$$

The thickness of the foam, $\delta_{foam} = \delta_{ins}$, will depend on the volume of the foam as follows,

$$\delta_{ins} = \frac{V_{gas}+V_c}{A_s} \qquad (6.16)$$

where V_{gas} and V_c are the gas and condensed phase volumes, respectively, in the partially reacted foam layer. Combining Eqns. (6.13, (6.15, and 6.16 and simplifying produces the equation,

$$\dot{r} = \frac{(T_f - T_s)}{\rho_{fu} c_{p,fu} (T_s - T_0)} \left[\frac{1}{h_{conv}} + \frac{3}{C_8 A_s k_c}\left(\frac{V_{gas}^2}{V_c} + 2V_{gas} + V_c\right)\right]^{-1}. \qquad (6.17)$$

For this equation to remain valid as the regression rate changes, the total amount of mass within the partially reacted layer needs to remain relatively the same, i.e. the change in foam rate production, due to a regression rate change, must equal the rate of foam consumption. There are two limiting cases for Eqn. (6.17 and the regression rates subsequent pressure dependence. The first limiting case comes about when $V_{gas} \gg V_c$, which will occur at lower chamber pressures. This will cause the thermal impedance of the partially reacted foam layer to vary inversely with chamber pressure to the 2nd power, assuming the gas in the foam follows the ideal gas law ($V \sim 1/p$), producing the simplified form,

$$\dot{r} = \left[\frac{1}{C_9 G_{ox}^{0.8}} + \frac{1}{C_{10} p_c^2}\right]^{-1} \qquad (6.18)$$

where C_9 and C_{10} are constants. This form provides a pressure dependency similar to that found in the experimental data, giving credence to a foam layer on the fuel surface. Fitting the experimental data to the general form of Eqn. (6.18 provides,

$$\dot{r} = \left[\frac{1}{0.62G_{ox}^{0.98}} + \frac{1}{2.0x10^{-7}p_c^{1.9}}\right]^{-1} \tag{6.19}$$

with an $R^2 = 0.98$, G_{ox} in lb/in^{2}s, p_c in psi. This fit is very similar to that provided in Eqn. (6.18 further indicating that the presence of the partially reacted foam layer is responsible for the non-traditional combustion behavior observed in the present -1 (6.19 instead of the 0.8 predicted is probably the result of higher flux values removing some of the foam layer. The higher flux values will cause the velocity in the chamber to increase resulting in a proportional increase in the friction force on the partially reacted foam layer. Thus, erosion of the foam layer can occur, resulting in the thickness of the foam layer to be partially flux dependent. This behavior is also probably why flux dependence is more apparent in the longer fuel grains, see Section 5.5, as higher velocities will be observed as the fuel grain length increases due to more mass entering the flow.

As combustor chamber pressure rises causing V_{gas} to decrease such that $V_{gas} \ll V_c$, another limit for Eqn. (6.17 can be determined. The thermal impedance of the of the partially reacted foam layer in this situation will vary linearly with pressure producing,

$$\dot{r} = \left[\frac{1}{C_9G_{ox}^{0.8}} + \frac{1}{C_{11}p_c} + C_{12}V_c\right]^{-1} \tag{6.20}$$

where C_{11} and C_{12} are constants. It is thus suspected that if the experiments were continued at higher chamber pressures, eventually the regression rate would depend linearly with pressure until the partially reacted foam layer becomes almost non-existent, resulting in the traditional hybrid rocket combustion model. In the transition region between the two extremes, it is expected that regression rate pressure dependence will vary between 1st and 2nd order. It is possible that the discrepancy of the pressure dependent (6.18 and -1 (6.19 is a result of the combustion behavior entering the transition region between low and high pressures, or it is possible that the assumptions made do not account for all the small nuances which cause pressure to influence the combustion behavior.

At some elevated pressure, the foam layer will eventually disappear leading to,

$$\dot{r} = 0.62 G_{ox}^{0.98} \tag{6.21}$$

or something fairly similar. Comparison of this trend with the previously tested hypergolic hybrid rockets is provided in Figure 6.8. It is thus suspected that, at high pressures, the current experimental fuel is capable of obtaining notably high regression rates.

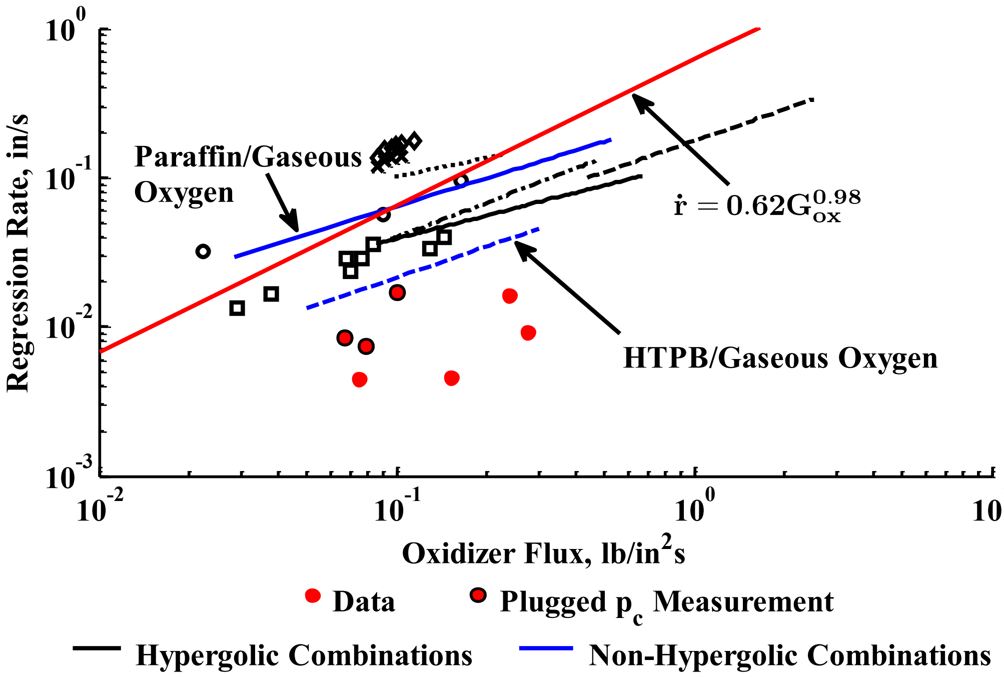

Figure 6.8 Regression rate of experimental fuel and other fuels as a function of $G_{ox,avg}$ with the theoretical regression rate of experimental fuel with no partially reacted foam layer.

6.6 Summary

We have reviewed multiple mechanisms that could be occurring in our hybrid combustor and evaluated their relevance to the observed data. It is evident from the experimental data ($\bar{\dot{r}} = 1.16x10^{-6}G_{ox}^{0.13}p_c^{1.61}$) that pressure greatly influences the regression rate of the fuel, whereas the flux down the fuel port has little to no bearing. Such a regression rate behavior has not been observed in previous experiments. As such, it is no surprise that classical hybrid rocket combustion theory does not adequately model the experimental data. Neither do the common deviations from classical theory, flame kinetics and radiation, provide an adequate explanation. Hypergolic reactions, uncommon for most hybrid motors, can exhibit combustion behavior that exhibits regression rates with higher pressure dependence;

however, these hypergolic reactions themselves are still inadequate to explain the current combustion behavior. The only mechanism that provides adequate explanation of the observed behavior is the inclusion of a foam layer on the fuel surface. Such a layer provides thermal insulation, that varies as $\sim 1/p^2$, from the convective heat transfer.

CHAPTER 7. CONCLUSIONS AND FUTURE WORK

7.1 Amine-boranes

This work has been conducted under two main objectives: (1) identify a material (or class of materials) and binder combinations that would produce viable and high performing hypergolic hybrid fuels with short ignition delays, and (2) study the combustion behavior of the identified fuel to understand what are the dominating combustion mechanisms.

The first objective was accomplished through the analysis of a class of materials known as amine-boranes. These materials consist of an amine (a traditional hypergolic fuel) and a borane (highly reactive) component that tend lose their toxic classification, becoming irritants, when combined together. Various amines and their corresponding amine-boranes were evaluated for hypergolicity, and it was found that the addition of the borane to an amine reduced the ignition delay, for all materials tested except one, making significant improvements. The reduction in ignition delay varied by 3.5-60 times less than the base amine. Some amine-boranes had very short ignition delays of 2-4 ms, the fastest ever recorded for amine based fuels reacting with nitric acid based oxidizers. These times are some of the shortest for any material ever used in hypergolic ignition.

The theoretical performance of the amine-boranes was also evaluated. Interestingly, the addition of a borane to an amine increased the theoretical specific impulse of the amine in all instances. The theoretical performance of several of the amine-boranes exhibited ranges of O/F ratios where high performance was maintained, an advantage for both hybrid rockets and rockets in general.

Multiple fuel binders were investigated to find a suitable amine-borane/binder system that would provide short ignition delays and high performance. The most promising binders were high temperature RTV silicone and Envirotex-Lite epoxy with several amine-borane/binder combinations producing hypergolic ignition delays with nitric acid between 3.3-10 ms. Such times are the shortest ever recorded for an amine based fuel/binder system and are on par with the fastest hypergolic hybrid oxidizer/fuel combinations.

When compared with other hypergolic hybrids, the amine-borane/epoxy based fuels exhibit lower toxicity, shorter ignition delays, and higher theoretical performance. Thus, the first objective was achieved with a series of hypergolic hybrid fuels that had relatively low toxicity, short ignition delays, and high performance.

These amine-borane/fuel binder combinations also provide several advantages over liquid hypergolic fuels and rocket fuels in general. The theoretical performance of several of the amine-borane/epoxy based fuels is on par or higher than the conventional liquid hypergolic fuels while providing similar ignition delays. However, compared to their liquid counterparts, the amine-borane/epoxy combination is relatively benign making them easier and cheaper to handle and operate. When compared to conventional rocket fuels, other than liquid hydrogen, several amine-borane/epoxy combinations also provides higher theoretical performance, suggesting that these fuels could benefit the rocket community more than just in the hypergolic area.

7.2 Combustion Behavior

The second objective of this work was accomplished by studying the combustion behavior of the amine-borane/fuel binder systems in the air, in an opposed flow oxygen burner, and in a hyerpgolic hybrid rocket combustor.

Both the combustion experiments in air and the opposed burner exhibited a multilayer combustion behavior for the fuel. High speed videos indicate the formation of a viscous foam like layer that eventually hardens and chars. This behavior appears to impede the heat transfer to the fuel surface of an amine-borane/binder system causing the fuel to regress slowly.

The hypergolic hybrid combustors experiments were all ignited hypergolically by spraying pure nitric acid across an EDBB/ferrocene/epoxy fuel grain. Ignition was consistent and smooth reaching 90% chamber pressure in under 100 ms when no cavitating venturi was present in the system. The ignition behavior was just as fast as or faster than other hypergolic hybrids previously reported.

The regression rate behavior of the fuel was unusual, producing the form $\bar{\dot{r}} = 1.16x10^{-6}G_{ox}^{0.13}p_c^{1.61}$. A regression rate with such a high pressure dependence has not been previously observed in any hybrid rocket system. It was also noted that the fuel surface expanded notably after combustion occurred; however, it was difficult to determine through observation if the fuel surface partially expanded during combustion.

Various theories were evaluated with the intent to provide an explanation of the observed combustion behavior. Neither the classical model nor the traditional deviations provide an adequate explanation for the observed behavior. Hypergolic reactions themselves also did not appear to provide an explanation. It was only upon including a foam insulation layer (a layer similar to what was observed in the opposed burner tests) that an adequate mathematical model was produced to match the combustion behavior. This result suggests that the partially reacted foam layer is present to some extent during combustor operation and greatly influences the combustion behavior producing the strong pressure dependence.

Using the foam theory, the combustion behavior of the EDBB/ferrocene/epoxy fuel could be extrapolated to high pressures, where no foam would be present. Such an exercise produces regression rates higher than most hybrid fuels tested. This suggests that the other amine-boranes, that do not tend to exhibit such a foaming behavior in hypergolic ignition tests, will probably produce very high regression rates, as many other aspects of the amine-boranes are similar.

Overall, amine-boranes have been found to exhibit promise for future implementation. The combination of low toxicity, high performance, low ignition delays, and high regression rates indicates that amine-boranes are a good hybrid and hypergolic hybrid fuels.

7.3 Future Work

Future efforts are identified in several areas to further elucidate the combustion behavior of the EDBB/ferrocene/epoxy fuel and to understand the combustion behavior of amine-borane based fuels in general.

The EDBB/ferrocene/epoxy fuel regression rate exhibited a strong pressure dependence that was attributed to a foam like layer on the fuel surface. Experiments in an optical combustor, that allows direct observations of the fuel surface during combustion, would be ideal to confirm the existence of and better understand this foam layer. Such an experiment would allow for direct observation of foam generation and consumption during steady state operations and provide a better sense of scale of the thickness of this layer. With this foam layer, it was noted in the present research that higher pressures will change the 2nd order pressure dependence to a linear dependence if the foam theory persists. Observations of such a transition could be mad by operating the combustor at higher pressures and would validate the present model. It was also noted in the present experiments that the regression rate will most likely eventually become purely flux dependent at notably high pressures, as the foam layer becomes non-existent. In such a regime, high fuel regression rates are predicted – confirmation of this would again further validate the present theory.

There are several other amine-boranes that exhibit potential for similar or higher performance at similar ignition delays as the EDBB/ferrocene/epoxy fuel including ammonia borane and dimethylpiperazine-bisborane. Future rocket combustor tests using these amine-boranes as the main fuel component will further validate the value of amine-boranes as a rocket fuel. Testing these materials over various flux and pressure ranges should provide high regression rates if the concepts discussed in the present work hold true.

As these fuel/oxidizer combinations are favorable for tactical military applications, it would also be important to investigate the combustion behavior of amine-borane based fuels will a gelled oxidizer; a gelled oxidizer is an important variant for tactical military applications designed to increase the safety of such a system.

Finally, the Envirotex Lite epoxy based binder was found to be the preferred binder out of the compatible binders; however, this binder is not commonly used in the rocket community. Therefore, other binders more accepted to the rocket community should be investigated. A common rocket binder is polybutadiene acrylonitrile (PBAN) that is similar to Envirotex Lite, suggesting it may be compatible with the amine-boranes. The individual components of PBAN exhibit lower viscosity, and thus better mixing, at elevated temperatures of around 333 K. Some amine-boranes have been noted to decompose at temperatures near 353 K, a high enough temperature that the use of PBAN as a binder for amine-boranes should be feasible. Other binders could also be investigated such as natural rubber or asphalt.

LIST OF REFERENCES

LIST OF REFERENCES

[1] Clark, J. D., *Ignition! An Informal History of Liquid Rocket Propellants*, Rutgers University Press, New Brunswick, New Jersey, 1972.

[2] Magnusson, U., "A Fuel for Hybrid Rockets," World Aerospace Systems, Vol. 2, 1996, pp. 50-52.

[3] Schmucker, R. H., and Schauer, W. M., "Die Experimentalhybridrakete Barbarella," *Technischen Universität Müchen*, Abschlußbericht LRT-TUM-TB-21-WARR, June, 1974.

[4] Schmucker, R., *Hybridraketenantriebe: eine Einführung in theoretische und technische Probleme*, Goldmann, München, 1972.

[5] Ankarsward, B., "The SR-1 Propulsion System," Symposium on Sounding Rockets and Experimental Results, Apr., 1970, Cardiff.

[6] Chiaverini, M. J., and Kuo, K. K., *Fundamentals of Hybrid Rocket Combustion and Propulsion*, Progress in Astronautics and Aeronautics, AIAA, Reston, VA, 2007.

[7] Afeefy, H. Y., Liebman, J. F., and Stein, S. E., "Neutral Thermochemical Data," *NIST Chemistry WebBook, NIST Standard Reference Database Number 69*, edited by W. G. Mallard and P. J. Linstrom, National Institute of Standards and Technology, Gaithersburg, MD, 2011, http://webbook.nist.gov.

[8] Pugibet, M., and Moutet, H., "Utilisation dans les Systèmes Hybrids de l'eau Oxygénée comme Comburant," *La Recherche Aerospatiale*, No. 132, 1969, pp. 15-31.

[9] Nadaud, L. and Baisini, J., "The Ablation of Solid Fuels Used in Hybrid Engines," *La Recherche Aerospatiale*, No. 115, 1966, pp. 45-55.

[10] Osmon, R. V., "An Experimental Investigation of a Lithium Aluminum Hydride - Hydrogen Peroxide Hybrid Rocket," *Aerospace Chemical Engineering*, Vol. 62, No. 61, 1966, pp.92–102.

[11] Cruise, D. R., "Theoretical Computations of Equilibrium Compositions, Thermodynamic Properties, and Performance Characteristics of Propellant Systems," Naval Weapons Center, NWC-TP-6037, China Lake, CA, April 1979.

[12] Austin, B. L., Heister, S. D., Dambach E. M., Meyer, S. E., and Wernimont, E. J., "Variable Thrust, Multiple Start Hybrid Motor Solutions for Missile and Space Applications," *46th AIAA/ASME/SAE/ASEE Joint Propulsion Conference and Exhibit*, Nashville, TN, July 2010, AIAA 2010-7121.

[13] Wernimont, E. J., Meyer, S. E., and Ventura, M. C., "Hybrid Motor System with Consumable Catalytic Bed a Composition of the Catalytic Bed and a Method of Using," U. S. Patent and Trademark Office, Patent #5,727,368, March, 1998.

[14] Paul, P. J., Mukunda, H. S., Narahari, H. K., Venkataraman, R., and Jain, V. K., "Regression Rate Studies in Hypergolic System," Combustion Science and Technology, Vol. 26, 1981, pp. 17-24.

[15] Kulkarni, S. G., and Panda, S. P., "Role of Thermal Degradation of Hybrid Rocket Fuels in Hypergolic Ignition and Burning with RFNA as Oxidizer," Combustion and Flame, Vol. 39, 1980, pp. 123-132.

[16] Panda, S. P. and Kulkarni, S. G., "Furfurylidene Ketones–A New Class of Hypergolic Rocket Fuels with Red Fuming Nitric Acid (RFNA) as Oxidizer," Combustion and Flame, Vol. 28, 1977, pp. 25-31.

[17] Munjal, N. L. and Parvatiyar, M. G., "Regression Rate Studies of Metalized Aniline Formaldehyde Hybrid Fuel," *Journal of Spacecraft*, Sept., Vol. 13, No. 9, 1976, pp. 572-573.

[18] Durgapal, U. C., and Chakrabarti, A. K., "Regression Rate Studies of Aniline Formaldehyde-Red Fuming Nitric Acid Hybrid System," *Journal of Spacecraft*, June, Vol. 11, No. 6, 1974, pp. 447-448.

[19] Munjal, N. L., and Parvatiyar, M. G., "Ignition of Hybrid Rocket Fuels with Fuming Nitric Acid as Oxidant," Journal of Spacecraft, June, Vol. 11, No. 6, 1974, pp. 428-430.

[20] Panda, S. P., Kulkarni, S. G., Kakade, S. D., and Rahalkar, A. B., "Synergistic Hypergolic Ignition of Amino End Group in Monomers and Polymers," Defense Science Journal, Vol. 36, 1986, pp. 429-437.

[21] Mukunda, H. S., Jain, V. K., Paul, P. J., "A Review of Hybrid Rockets: Present Status and Future Potential," Proceedings of the Indian Academy of Science Section C: Engineering Sciences, Vol. 2, 1979, pp. 215-242.

[22] Sippel, T. R., Shark, S. C., Hinkelman, M. C., Pourpoint, T. L., Son, S. F., and Heister, S. D., "Hypergolic Ignition of Metal Hydride-based Fuels with Hydrogen Peroxide," 7th US National Combustion Meeting, Mar., 2011, Atlanta, GA.

[23] Gune, S. G., Kulkarni, S. G., and Panda, S. P., "Synergistic Hypergolic Ignition of Solid Substituted Anilines Mixed with Magnesium Powder and Red Fuming Nitric Acid," Combustion and Flame, Vol. 61, 1985, pp. 189-193.

[24] Jain, S. R., Vittal, J. J., and Mimani, T., "Some Mechanistic Aspects of Hypergolic Igntion - Reaction of Dinitrogen Tetroxide with Solid Amines and Their Mixtures with Magnesium," Defense Science Journal, Jan, Vol. 42, No. 1, 1992, pp. 5-12.

[25] Bernard, M. L., Cointot, A., Auzanneau, M., and Sztal, B., "The Role of Surface Reactions in Hypergolic Ignition of Liquid-Solid Systems," Combustion and Flame, Vol. 22, 1974, pp. 1-7.

[26] Jain, S. R., Murthy, K. N., and Thanoo, B. C., "Ignition Delay Studies on Hypergolic Fuel Grains," Defense Science Journal, July, Vol. 38, No. 3, 1988, pp. 273-286.

[27] Gao, H. and Shreeve, J. M., "Ionic Liquid Solubilized Boranes as Hypergolic Fluids," Journal of Materials Chemistry, Vol. 22, 2012, pp. 11022-11024.

[28] Jain, S. R., Mimani, T., and Vittal, J. J., "Chemical Aspects of the Synergistic Hypergolic Ignition in Hybrid Systems with N2O4 as Oxidizer," Combustion, Science, and Technology, Vol. 64, 1989, pp. 29-41.

[29] Bernard, M. L., Cointot, A., Auzanneau, M., and Sztal, B., "The Role of Surface Reactions in Hypergolic Igntion of Liquid-Solid Systems," Combustion and Flame, Vol. 22, 1974, pp. 1-7.

[30] Rajendran, G., and Jain, S. R., "Novel Solid Hypergolic Fuels for Hybrid Propellants," Fuel, Vol. 63, 1984, pp. 709-712.

[31] Kulkarni, S. G., and Panda, S. P., "Synthesis, Characterization and Hypergolicity of Aliphatic Furfurylidene Ketones with Red Fuming Nitric as Oxidizer," Combustion and Flame, Vol. 40, 1981, pp. 29-36.

[32] Jain, S. R., "Spontaneously Igniting Hybrid Fuel-Oxidiser Systems," Defence Science Journal, Vol. 45, No. 1, 1995, pp. 5-16.

[33] Jain, S. R., Krishna, P. M. M., Pai Verneker, V. R., "Effect of Variables on Ignition Delays of Hydrazone/Nitric Acid Systems," Propellants and Explosives, Vol. 5, 1980, pp. 135-138.

[34] Panda, S. P., Kulkarni, S. G., Kakade, S. D., and Rahalkar, A. B., "Synergistic Hypergolic Ignition of Aimo End Group in Monomer and Polymers," Defense Science Journal, Vol. 36, No. 4, 1986, pp. 429-437.

[35] DeSain, J. D., Curtiss, T. J., Metzler, K. M., and Brady, B. B., "Testing Hypergolic Ignition of Paraffin Wax / LiAlH4 Mixtures," 46th AIAA/ASME/SAE/ASEE Joint Propulsion Conference & Exhibit, July, 2010, Nashville, TN, AIAA 2010-6636.

[36] Schauer, W. M., and Schmucker, R. H., "Recent Results of Hypergolic Ignition with Hybrid Propellants," AIAA 15th Aerospace Science Meeting, Jan., 1977, Los Angeles, CA, AIAA-P-77-16.

[37] Barrere, M., Jaumotte, A., Fraeijs de Veubeke, B., and Vandenkerckhove, J., "Liquid Propellants," *Rocket Propulsion*, English ed., Elsevier, New York, 1960, pp. 587-645.

[38] Jain, S. R., "Self-Igniting Fuel-Oxidizer Systems and Hybrid Rockets," Journal of Scientific & Industrial Research, April, Vol. 62, 2003, pp. 293-310.

[39] Corpening, J. H., Palmer, R. K., Heister, S. D., and Rusek, J. J., "Combustion of Advanced Non-Toxic Hybrid Propellants," *International Journal of Alternative Propulsion*, Vol. 1, No. 2/3, 2007, pp. 154-173.

[40] Wang, S. Q., and Thynell, S. T., "An Experimental Study on the Hypergolic Interaction Between Monomethylhydrazine and Nitric Acid," *Combustion and Flame*, Vol. 159, 2012, pp. 438-447.

[41] Lo, R, "Empirical Laws for Hybrid Combustion of Lithium Hydride with Flourine in Small Rocket Engines," Deutsche Luft- and Raumfahrt, Research Report 67-57, Sept. 1067, NASA Technical Translation F-12,336, 1969.

[42] Smoot, L. D., and Price, C. F., "Pressure Dependence of Hybrid Fuel Regression Rates," *AIAA Journal*, Vol. 5, No. 1, 1967, pp. 102-106.

[43] Smoot, L. D., Price, C. F., and Mihlfeith, C. M., "The Pressure Dependence of Hybrid Fuel Regression Rates," *3rd Aerospace Sciences Meeting*, New York, NY, Jan. 1966, AIAA 66-113.

[44] Sutton, G. P., *Rocket Propulsion Elements*, 7th ed., Wiley, New York, 2001, pp. 591.

[45] Karabeyoglu, M. A., Altman, D., and Cantwell, B. J., "Combustion of Liquefying Hybrid Propellants: Part 1, General Theory," *Journal of Propulsion and Power*, Vol. 18, No. 3, 2002, pp. 610-620.

[46] Bernard, MM. M. L., and Joulain, P., "Pressure Dependence of Liquid-Solid Ablation Rate," *Combustion Science and Technology*, Vol. 1, 1970, pp. 471-480.

[47] Bernard, M. L., Auzanneau, M., Baronnet, F., and Joulain, P., "Study of Solid-Fuel Ablation by Liquid and Physically Homogeneous Nitric Acid," *AIAA Journal*, Sept., Vol. 7, No. 9, 1969, pp. 1676-1681.

[48] Kumar, R. N., and Stickler, D. B., "Polymer-Degradation Theory of Pressure-Sensitive Hybrid Combustion," *13th Symposium (International) on Combustion*, Combustion Inst., Pittsburgh, PA, 1971, pp. 1059-1072.

[49] Smoot, L. D., and Price, C. F., “Regression Rates of Nonmetalized Hybrid Fuel Systems,” *AIAA Journal*, Vol. 3, No. 8, 1965, pp. 1408-1413.

[50] Smoot, L. D., and Price, C. F., “Regression Rates of Metalized Hybrid Fuel Systems,” *AIAA Journal*, Vol. 4, No. 5, 1966, pp. 910-915.

[51] Rastogi, R. P., and Deepak, D., “Pressure Dependence of Hybrid Fuel Burning Rate,” *AIAA Journal*, Vol. 14, No. 7, 1976, pp. 988-990.

[52] Houser, T. J. and Peck, M. V., “Research in Hybrid Combustion,” *AIAA Heterogeneous Combustion Conference*, Palm Beach, FL, Dec. 1963, AIAA 63-510.

[53] Kosdon, F. J., and Williams, F. A., “Pressure Dependence of Nonmetalized Hybrid Fuel Regression Rates,” *AIAA Journal*, Vol. 5, No. 4, 1967, pp. 774-778.

[54] Miller, E., “Hybrid Rocket Combustion Regression Rate Model,” *AIAA Journal*, Vol. 4, No. 4, 1966, pp. 752-753.

[55] Wooldridge, C. E., Marxman, G. A., and Kier, R. J., *Investigation of Combustion Instability in Hybrid Rockets*, NASA CR-66812, 1969.

[56] Marxman, G. A., “Boundary-Layer Combustion in Propulsion,” *11th Symposium (International) on Combustion*, Combustion Inst., Pittsburgh, PA, 1966, pp. 269-289.

[57] Weismiller, M. R., Connell, T. L., Risha, G. A., and Yetter, R. A., “Characterization of Ammonia Borane (NH_3BH_3) Enhancement to a Paraffin Fueled Hybrid Rocket System,” 46th AIAA/ASME/SAE/ASEE Joint Propulsion Conference & Exhibit, July, 2010, Nashville, TN, AIAA 2010-6639.

[58] Risha, G. A., Connell, T. L., Weismiller, M., Yetter, R. A., Sundaram, D. S., Yang, V., Wood, T. D., Pfeil, M. A., Pourpoint, T. L., Tsohas, J., and Son, S. F., “Novel Energetic Materials for Space Propulsion,” Air Force Office of Scientific Research, A818645, Arlington, VA, Apr. 2011.

[59] Pfeil, M. A., Groven, L. J., Lucht, R. P., and Son, S. F., “Effects of Ammonia Borane on the Combustion of an Ethanol Droplet at Atmospheric Pressure,” Combustion and Flame, Vol. 160, 2013, pp. 2194-2203.

[60] Pfeil, M. A., Son, S. F., and Anderson, W. E., “The Influence of the Addition of Ammonia Borane on the Combustion Stability of a Liquid Rocket Combustor,” accepted to Journal of Propulsion and Power, 2013.

[61] Lee, J. G., Weismiller, M. R., Connell, T. L., Risha, G. A., Yetter, R. A., Gilbert, P. D., and Son, S. F., “Ammonia Borane Based Propellants,” 44th AIAA/ASME/SAE/ASEE Joint Propulsion Conference & Exhibit, July, 2008, Hartford, CT, AIAA 2008-5037.

[62] Kilpatrick, M., and Baker, L. L., Jr., "A Study of Fast Reactions in Fuel-Oxidant Systems: Anhydrous Hydrazine with 100 Per Cent Nitric Acid," Symposium (International) on Combustion, Vol. 5, 1955, pp. 196-205.

[63] Ramachandran, P. V., Gagare, P. D., Mistry, H., and Biswas, B., "Procedures for the Synthesis of Ethylenediamine Bisborane and Ammonia Borane," WIPO Patent WO/2012/006347, 2012.

[64] Ramachandran, P. V., and Gagare, P. D., "Preparation of Ammonia Borane in High Yield and Purity, Methanolysis, and Regeneration," Inorganic Chemistry, Vol. 46, 2007, pp. 7810-7817.

[65] Ramachandran, P. V., Raju, B. C., and Gagare, P. D., "One-Pot Synthesis of Ammonia-Borane and Trialkylamine-Boranes from Trimethyl Borate," Organic Letters, Vol. 14, 2012, 6119-6121.

[66] Ramachandran, P. V., Kulkarni, A. S., "Nucleophilic Displacement of Ammonia from Ammonia Borane for the Preparation of Alkylamine-, Pyridine- and Phosphine-Boranes," Royal Society of Chemistry Advances, Vol. 4, 2014, 26207-26210.

[67] Sigma-Aldrich, www.sigmaaldrich.com [cited Feb. 2014].

[68] Saveyn, H., Mermuys, D., Thas, O., and Meeren, P., "Determination of the Refractive Index of Water-dispersible Granules for Use in Laser Diffraction Experiments," Particle & Particle Systems Characterization, Vol. 19, 2002, pp. 426-432.

[69] "Rapid Refractive Index Determination for Pharmaceutical Actives," Malvern Instruments Ltd., MRK529-03, 2003.

[70] USAF, "Military Standard Safety and Performance Tests for Qualification of Explosives," Department of Defense, MIL-STD-1751, Washington D.C., Aug., 1982.

[71] ASTM Standard B923-10, 2010, "Standard Test Method for Metal Powder Skeletal Density by Helium of Nitrogen Pycnometry," ASTM International, West Conshohocken, PA, 2010, DOI: 10.1520/B0923-10.

[72] Bastea, S., Fried, L. E., Glaesemann, K. R., Howard, W. M., Kuo, I. W., Souers, P. C., Vitello, P. A., Cheetah 6.0, Lawrence Livermore National Laboratory, Livermore, CA, 2010.

[73] NASA CEA, Chemical Equilibrium with Applications, Ver. 2, Lewis Research Center, Cleveland, OH, 2002.

[74] Young, G., Risha, G. A., Miller, A. G., Glass, R. A., Connell, J. . T. L., and Yetter, R. a., "Combustion of Alane-Based Solid Fuels," *International Journal of Energetic Materials and Chemical Propulsion*, Vol. 9, No. 3, 2010, pp. 249–266.

[75] Zaseck, C. R., Shark, S. C., Son., S. F., and Pourpoint, T. L., "Paraffin Fuel and Additive Combustion in an Opposed Flow Burner Configuration," *48th AIAA/ASME/SAE/ASEE Joint Propulsion Conference & Exhibit*, July-Aug., 2012, Atlanta, GA, AIAA 2012-3963.

[76] Terry, B. C., Lin, Y., Manukyan, K. V., Mukasyan, A. S., Son, S. F., and Groven, L. J., "The Effect of Silicon Powder Characteristics on the Combustion of Silicon/Teflon/Viton Nanoenergetics," submitted to Propellants, Explosives, Pyrotechnics, 2013.

[77] Terry, B. C., "The Effect of Silicon Powder Characteristics on the Combustion of Silicon/Teflon/Viton Nanoenergetics," Masters Thesis, School of Aeronautical and Astronautical Engineering, Purdue University, West Lafayette, IN, 2013.

[78] Kulkarni, S. G., and Panda, S. P., "Role of Thermal Degradation of Hybrid Rocket Fuels in Hypergolic Ignition and Burning with RFNA as Oxidizer," *Combustion and Flame*, Vol. 39, 1980, pp. 123-132.

[79] Groshens, T. J., and Hollins, R. A., "New Chemical Hydrogen Storage Materials Exploiting the Self-Sustaining Thermal Decomposition of Guanidinium Borohydride," Chemistry Communications, 2009, pp. 3089-3091.

[80] Klooster, W. T., Koetzle, T. F., Siegbahn, P. E. M., Richardson, T. B., and Crabtree, R. H., "Study of the N-H•••H-B Dihydrogen Bond Including the Crystal Structure of BH3NH3 by Neutron Diffraction," Journal of the American Chemical Society, 1999, Vol. 121, pp. 6337–6343.

[81] McQuaid, M. and Chen, C., "BH3-Amine and B(CH3)3-Amine Adducts as Additives for Liquid/Gel Hypergols and Solid Hybrid Rocket Motor Fuels: Property and Performance Predictions," ARL-TR-6749, Army Research Laboratory, Aberdeen Proving Ground, MD, Dec. 2013.

[82] Matus, M. H., Grant, D. J., Nguyen, M. T., and Dixon, D. A., "Fundamental Thermochemical Properties of Ammonia Borane and Dehydrogenated Derivatives (BNHn, n = 0–6)," Journal of Physical Chemistry C, Vol. 113, 2009, pp. 16553-16560.

[83] Sana, M., Leroy, G., and Wilante, C., "Enthalpies of Formation and Bond Energies in Lithium, Beryllium, and Boron Derivatives. 2. Dative, Single, and Triple Bonds," Organometallics, Vol. 11, 1992, pp. 781-787.

[84] Wright, A. C., "USAF Propellants Handbook Nitric Acid/Nitrogen Tetroxide Oxidizers," Martin Marietta Corporation, *AFRPL-TR-76-76*, Vol. 2, Denver, CO, Feb., 1977.

[85] Kroenlein, K., Muzny, C. D., Kazakov, A. F., Diky, V., Chirico, R. D., Magee, J. W., Abdulagatov, I., and Frenkel, M., NIST/TRC Web Thermo Tables (WTT), Version 2-2012-1-Pro, National Institute of Standards and Technology, Boulder, CO, 2012, http:// wtt-pro.nist.gov.

[86] Lengelle, G., "Solid-Fuel Pyrolysis Phenomena and Regression Rate, Part 1: Mechanisms," *Fundamentals of Hybrid Rocket Combustion and Propulsion*, Progress in Astronautics and Aeronautics, AIAA, Reston, VA, 2007, pp. 127-165.

[87] Coleman, H. W., and Steele, W. G., *Experimentation and Uncertainty Analysis for Engineers*, 2nd Edition, John and Wiley Sons, Inc., 1999.

[88] Connaughton, J. W., Wilson, B. F., and Wharton, W. W., "An Experimental Study of Hypergolic Ignition and Restart in a Unique Hybrid Window Motor," *3rd Aerospace Sciences Meeting*, Jan. 24-26, 1966, New York, NY, AIAA 66-69.

[89] Barrere, M. and Moutet, A., "Résultats Récents Obtenus sur les Systèmes Hybrides ou a Lithergols," *17th International Astronautical Congress*, Oct. 9-15, 1966, Madrid, Spain.

[90] Verdier, C., "Hypergols Phosphores Solides," *La Recherche Aėrospatiale*, Vol. 4, 1970, pp. 181-189.

[91] Wernimont, E. J., and Heister, S. D., "Combustion Experiments in Hydrogen Peroxide/Polyethylene Hybrid Rocket with Catalytic Ignition," *Journal of Propulsion and Power*, Vol. 16, 2000, pp. 318-326.

[92] Muzzy, R. J., "Applied Hybrid Combustion Theory," *AIAA/SAE 8th Joint Propulsion Specialist Conference*, New Orleans, LA, Nov. 29 – Dec. 1, 1972.

[93] Marxman, G., and Gilbert, M., "Turbulent Boundary Layer Combustion in the Hybrid Rocket," *9th Symposium (International) on Combustion*, Combustion Inst., Ithaca, NY, 1962, pp. 371-383.

[94] Altman, D., and Humble, R. W., "Hybrid Rocket Propulsion Systems," *Space Propulsion Analysis and Design*, The McGraw-Hill Companies, Inc., 1995, pp. 374-395.

[95] Wooldridge, C. E., Marxman, G. A., and Kier, R. J., "Investigation of Combustion Instability in Hybrid Rockets," Final Report NASA CR-66812, Contract NAS 1-7310, 1969.

[96] Incropera, F. P., Dewitt, D. P., Bergman, T. L., and Lavine, A. S., *Fundamentals of Heat and Mass Transfer*, 6th Edition, John and Wiley Sons, Inc., 2007.

[97] Son, S. F., and Brewster, M. Q., "Radiation-Augmented Combustion of Homogeneous Solids," Combustion, Science, and Technology, vol. 107, 1995, pp. 127-154.

[98] Lieberherr, J. F., "Les Lois Expérimentales de Vitesse D'Ablation et Leur Application aux Moteurs a Lithergol," *La Recherche Aerospatiale*, No. 110, 1966, pp. 7-14.

[99] Glicksman, L. R., "Heat Transfer in Foams," *Low Density Cellular Plastics: Physical Basis of Behavior*, Springer-Science + Business Media, Dordrecht, Netherlands, 1994, pp. 104-152.

[100] Mohajeri, N., T-Raissi, A., and Ramasamy, K. K., "Thermal Conductivity of Ammonia Borane Complex and its Composites with Aluminum Powder," *Thermochimica Acta*, Vol. 452, No. 1, 2007, pp. 28-30.

[101] Lefebvre, A. H., *Atomization and Sprays*, Taylor and Francis Group, 1989.

[102] Robertson, G. D., Mason, D. M., and Corcoran, W. H., "The Kinetics of the Thermal Decomposition of Nitric Acid in the Liquid Phase," *Journal of Physical Chemistry*, Vol. 59, 1955, pp. 683-690.

[103] Design Institute for Physical Research, *Evaluated Standard Thermophysical Property Values*, DIPPR Project 801 – Full Version, 2013, http://app.knovel.com/hotlink/toc/id:kpDIPPRPF7/dippr-project-801-full/dippr-project-801-full.

[104] Sankaran, V., "Computational Fluid Dynamics Modeling of Hybrid Rocket Flowfields," *Fundamentals of Hybrid Rocket Combustion and Propulsion*, Progress in Astronautics and Aeronautics, AIAA, Reston, VA, 2007, pp. 323-349.

APPENDICES

Appendix A Mixing Procedures Documents

PURDUE
UNIVERSITY

ZL-4
Procedures

Originator: Mark Pfeil
Authorized user: Mark Pfeil
Authorized by: Steve Son (01/2013)

Resodyn Mixing Procedures for Hybrid Fuels

29-Jan-13

Test Requirements: Mixing will occur when another student is in building and aware of mixing activities or when permission is provided by supervisor. All safety equipment must be present before mixing begins.				
Potential Hazards: 1. Exposure to organic vapors. 2. Reaction of material during mixing				
Mitigations: 1. Proper PPE including appropriate gloves, safety glasses, face shield, splash goggles, lab coat, static wrist band (if necessary), organic vapor respirator (if necessary) 2. Proper fire extinguish equipment. 3. See MSDS for specific materials PPE and fire extinguishment media				
SECTION 0: EMERGENCY				
IN CASE OF FIRE OR OTHER INCIDENT				
0.000	Test conductors will use their best judgment to determine the severity of the situation			
0.001	Regardless of the incident severity, the appropriate personnel from the predetermined list will be notified by phone of the incident and will provide guidance for further action. Steven Son: 765-337-8204 Scott Meyer: 765-426-8095			
0.002	Quench reaction if safe and possible. If not, clear area			
0.003	Extinguish fire if safe with compatable material (see MSDS). If not, evacuate building and call 911.			
1. Preparation				
1.000	Obtain handycam and attach to t.v. in control room			
1.001	Turn on Resodyn, connect to computer, and verify it is working properly			
1.002	Verify warning sign is available to place on t-cell door			
2. Mixing				
2.000	Clear t-cell of extraneous personell			
2.001	Don appropriate PPE			
2.002	Make sure additives are completely wetted by binder			
2.003	If binder concentration is low enough that powder cannot be completely wetted by binder and powder is ESD sensitive, put mixture under argon or another inert gas before mixing			
2.004	Attach mixing container to Resodyn and put on Resodyn lid			

2.005	Return to control room while placing warning sign on t-cell door and close door			
2.006	Begin mixing at a reduced power to make sure propellant is behaving correctly			
2.007	Increase power of Resodyn until desired intensity is reached (make sure that no solid "balls" of material are bouncing around vigorously in the mixing container if using glass containers)			
2.008	Remove material and mix by hand as necessary to ensure complete mixing of material if necessary. Continue mixing on Resodyn repeating steps 2.002-2.007 until completely mixed			
2.009	If done mixing for the day, turn of Resodyn			
2.010	Remove warning sign from door and remove PPE			

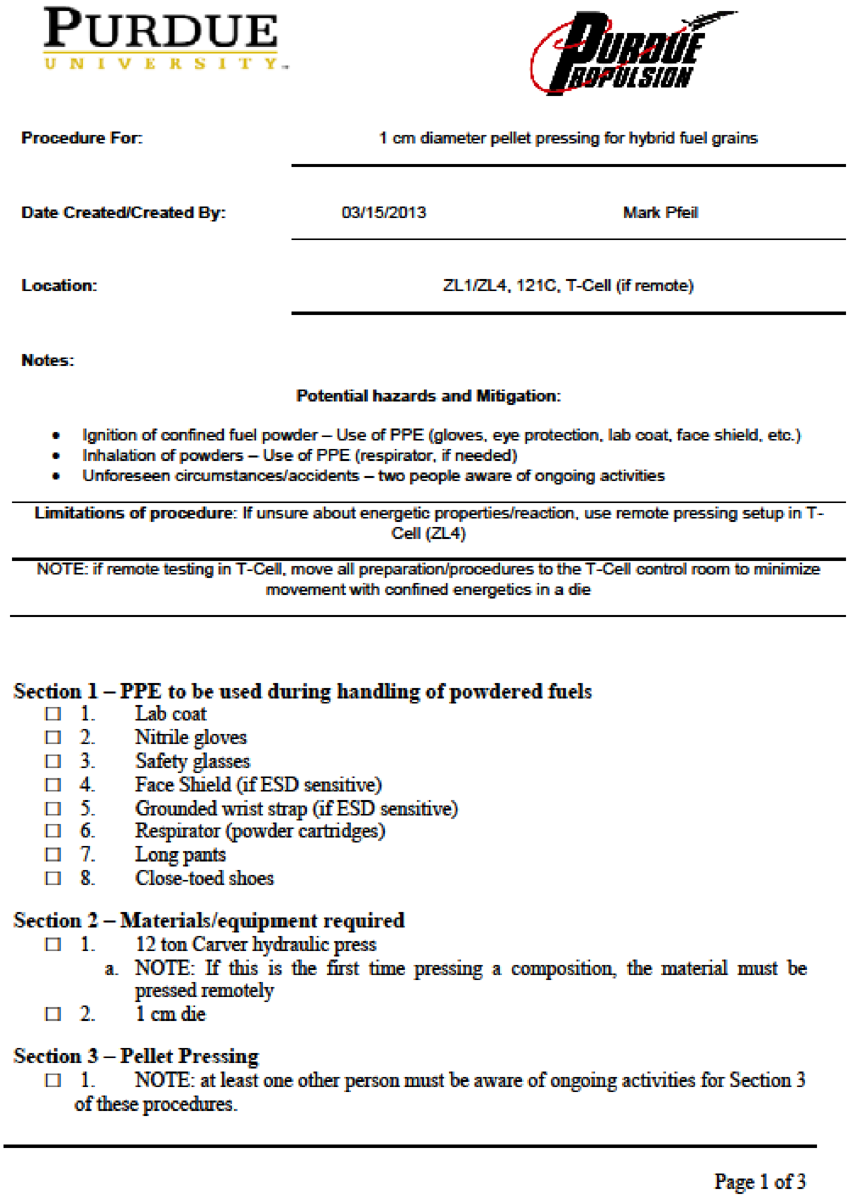

PURDUE UNIVERSITY

PURDUE PROPULSION

Procedure For: 1 cm diameter pellet pressing for hybrid fuel grains

Date Created/Created By: 03/15/2013 Mark Pfeil

Location: ZL1/ZL4, 121C, T-Cell (if remote)

Notes:

Potential hazards and Mitigation:

- Ignition of confined fuel powder – Use of PPE (gloves, eye protection, lab coat, face shield, etc.)
- Inhalation of powders – Use of PPE (respirator, if needed)
- Unforeseen circumstances/accidents – two people aware of ongoing activities

Limitations of procedure: If unsure about energetic properties/reaction, use remote pressing setup in T-Cell (ZL4)

NOTE: if remote testing in T-Cell, move all preparation/procedures to the T-Cell control room to minimize movement with confined energetics in a die

Section 1 – PPE to be used during handling of powdered fuels

☐ 1. Lab coat
☐ 2. Nitrile gloves
☐ 3. Safety glasses
☐ 4. Face Shield (if ESD sensitive)
☐ 5. Grounded wrist strap (if ESD sensitive)
☐ 6. Respirator (powder cartridges)
☐ 7. Long pants
☐ 8. Close-toed shoes

Section 2 – Materials/equipment required

☐ 1. 12 ton Carver hydraulic press
  a. NOTE: If this is the first time pressing a composition, the material must be pressed remotely
☐ 2. 1 cm die

Section 3 – Pellet Pressing

☐ 1. NOTE: at least one other person must be aware of ongoing activities for Section 3 of these procedures.

Page 1 of 3

☐ 2. Put on PPE: safety glasses, nitrile gloves, lab coat
☐ 3. Assemble the 1 cm die
☐ 4. Put on PPE: Respirator (if fine powders or known to be hazardous), ESD ppe (if ESD sensitive)
☐ 5. Weigh out __________ g of material and place into the 1 cm die.
☐ 6. Place the plunger into the die and any other appropriate pieces (e.g., end cap)
☐ 7. Take off respirator (if used) and remove ESD ppe
☐ 8. Place the die assembly onto the carver press, aligning the base to be centered
☐ 9. Place shims on top of the die (if required)
☐ 10. Leave to a remote location (if required)
☐ 11. Increase the pressure on the press to ______ psi
☐ 12. Keep the pressure for ______ minutes. If the pressure drops, set it back to ______ psi
☐ 13. After ______ minutes, release the pressure and remove the die from the press
☐ 14. Put on additional PPE: Respirator (if residual fine powders are still found after pressing)
☐ 15. Use the hydraulic press to take the pellet out by: placing the cylinder under the die; using the press to press the plungers out of the die, until the top plunger is flush with the top surface of the die, then lower the press; place the press pole concentrically on top of the plungers; continue pressing until the pellet falls out into the cylinder.
☐ 16. Record the weight, diameter, and length of the pellet and use that information to calculate the percent theoretical maximum density (%TMD)
☐ 17. Thoroughly clean the pressing die
☐ 18. Take off respirator

Section 4 – Storage, Handling, and Disposal of Materials

☐ 1. Storage: All materials produced in this process need to be stored in either an appropriate vacuum desiccator box or in Cabinet 10 of Room 110 (ZL4). If stored in Cabinet 10, the inventory list must be updated with the new materials and quantity.
☐ 2. Handling: When handling this material, the following PPE must be used: safety glasses, appropriate gloves and clothing.
☐ 3. Disposal: Use approved REM procedures or contact supervisor

Section 5 – Emergency Procedures

☐ 1. Unintentional ignition of material resulting in bodily injury: If minor injury is sustained from the incident (e.g., minor burns), treat with appropriate first aid and contact a supervisor. If major injury is sustained, immediately call 911 and then contact a supervisor.
☐ 2. Unintentional ignition of material resulting in uncontrolled fire: Ensure that fire is extinguished using appropriate fire extinguisher and then contact a supervisor. If fire is sufficiently uncontrolled, immediately pull a fire alarm, evacuate the building, call 911, and then contact a supervisor. If a fire is sufficiently controlled (e.g., unintentional

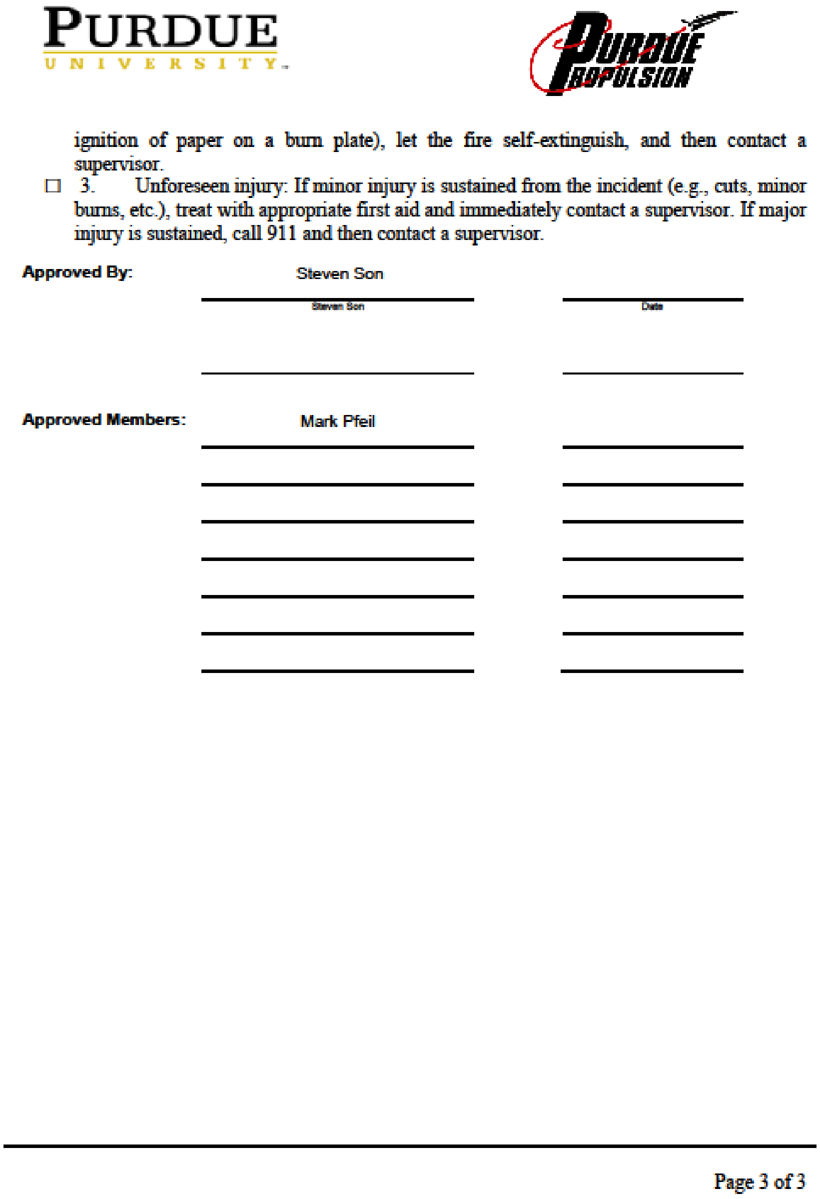

ignition of paper on a burn plate), let the fire self-extinguish, and then contact a supervisor.

☐ 3. Unforeseen injury: If minor injury is sustained from the incident (e.g., cuts, minor burns, etc.), treat with appropriate first aid and immediately contact a supervisor. If major injury is sustained, call 911 and then contact a supervisor.

Approved By:	Steven Son	
	Steven Son	Date
Approved Members:	Mark Pfeil	

Appendix B Combustor and Plumbing and Instrumentation Diagram

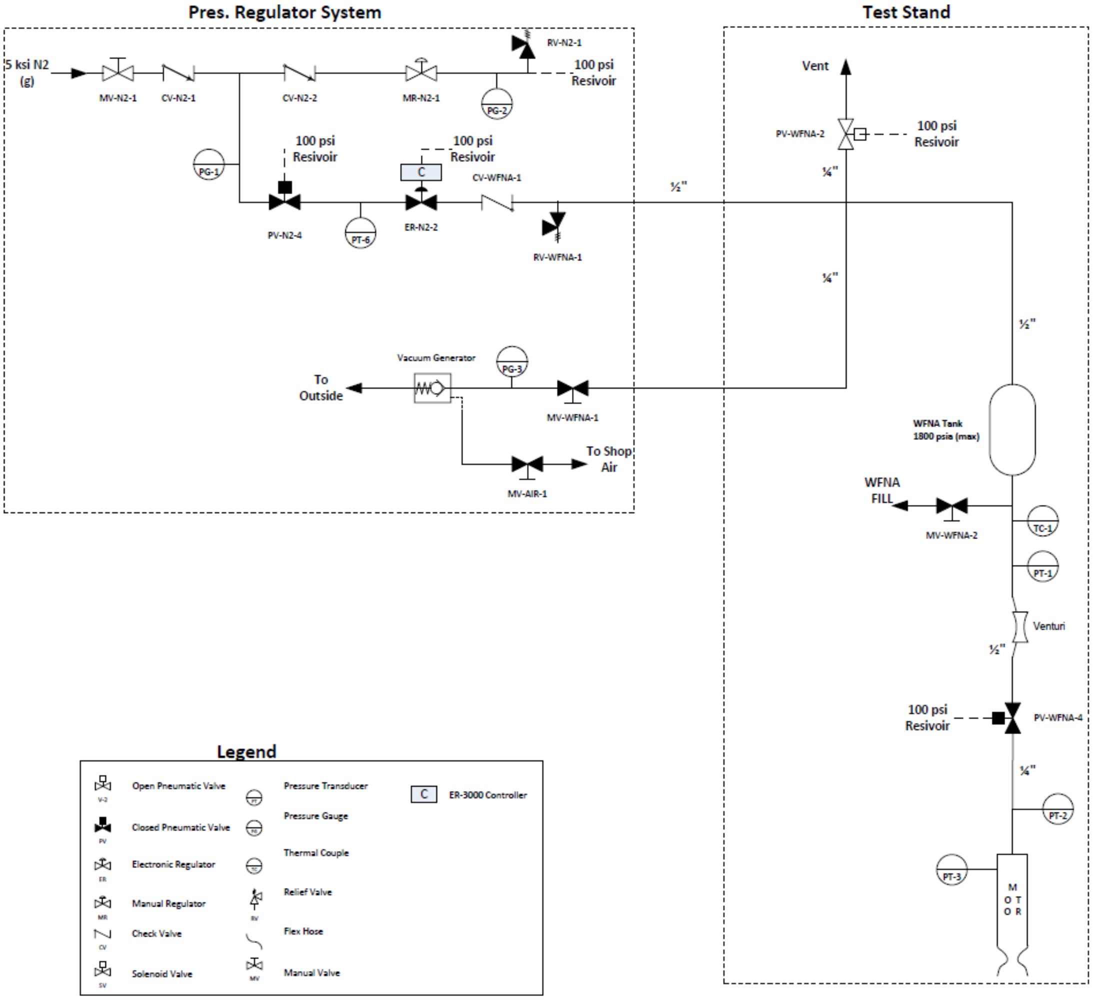

Figure B.1 A schematic of the pressurization, oxidizer fill, vent, and oxidizer feed system.

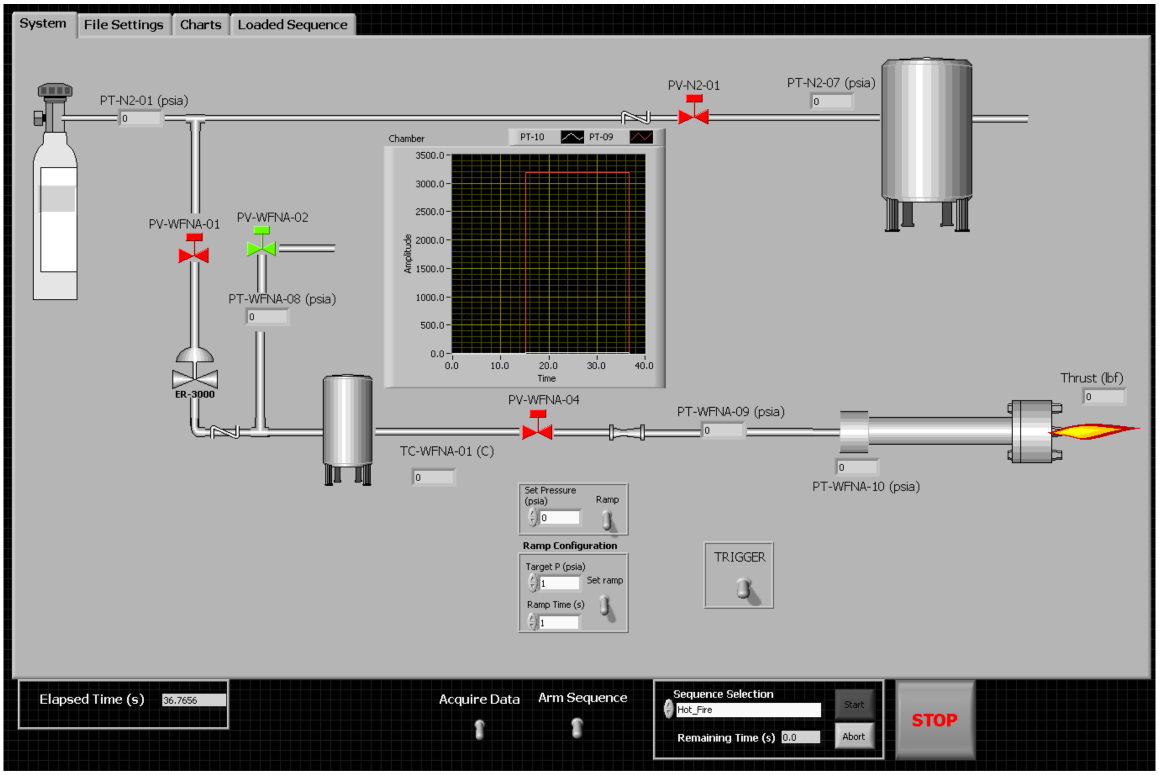

PT-N2-01 (psia) 0

PT-N2-07 (psia) 0

PT-WFNA-08 (psia) 0

TC-WFNA-01 (C) 0

PT-WFNA-09 (psia) 0

PT-WFNA-10 (psia) 0

Thrust (lbf) 0

Set Pressure (psia) 0

Target P (psia) 1

Ramp Time (s) 1

Elapsed Time (s) 36.7656

Sequence Selection Hot_Fire

Remaining Time (s) 0.0

Figure B.2 Labview VI used to control rocket combustor test and record data.

Appendix C Combustor Operation Procedures

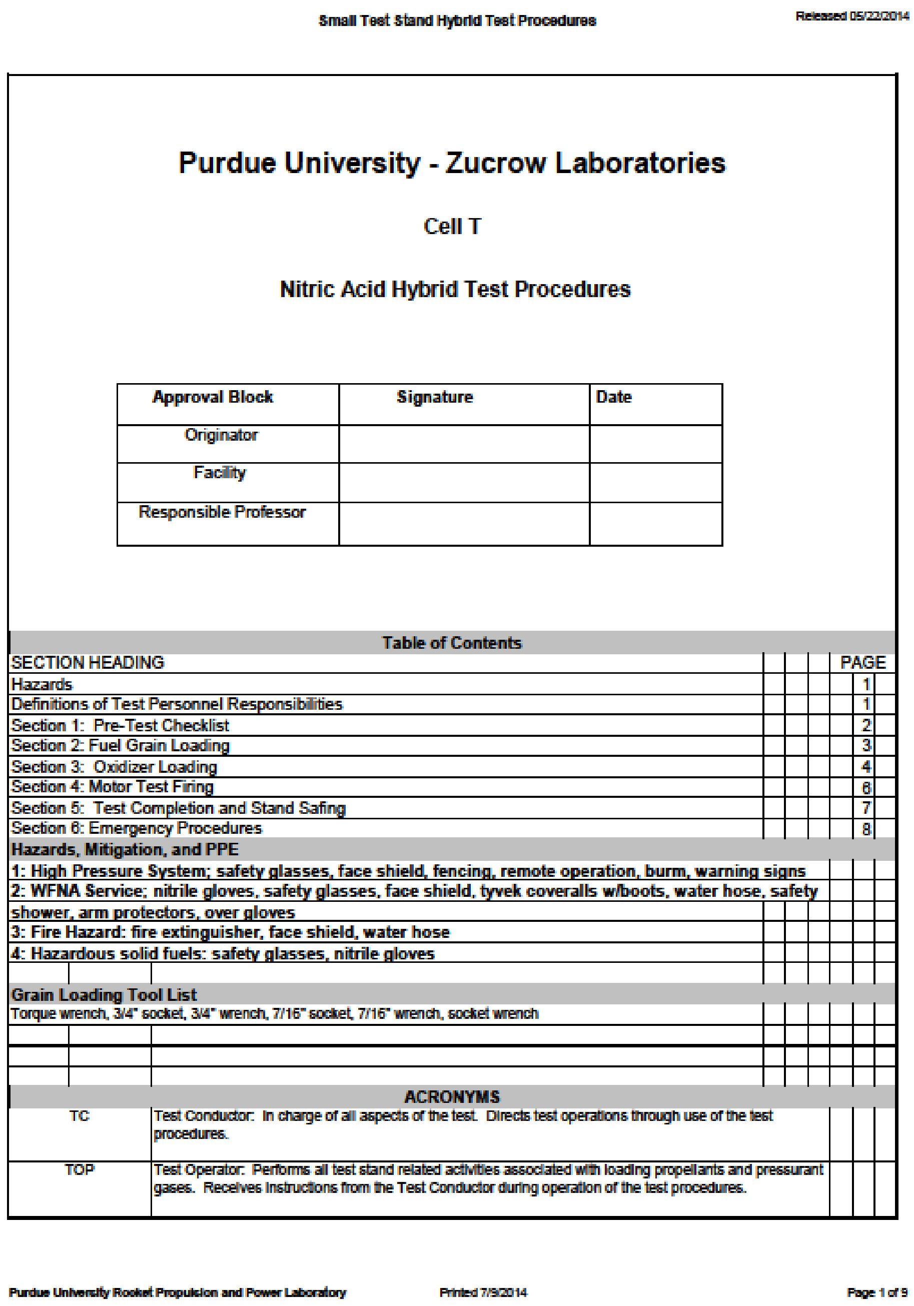

Small Test Stand Hybrid Test Procedures Released 05/22/2014

Purdue University - Zucrow Laboratories

Cell T

Nitric Acid Hybrid Test Procedures

Approval Block	Signature	Date
Originator		
Facility		
Responsible Professor		

Table of Contents

Hazards, Mitigation, and PPE

1: High Pressure System; safety glasses, face shield, fencing, remote operation, burm, warning signs

2: WFNA Service; nitrile gloves, safety glasses, face shield, tyvek coveralls w/boots, water hose, safety shower, arm protectors, over gloves

3: Fire Hazard: fire extinguisher, face shield, water hose

4: Hazardous solid fuels: safety glasses, nitrile gloves

Grain Loading Tool List

Torque wrench, 3/4" socket, 3/4" wrench, 7/16" socket, 7/16" wrench, socket wrench

ACRONYMS

TC	Test Conductor: In charge of all aspects of the test. Directs test operations through use of the test procedures.
TOP	Test Operator: Performs all test stand related activities associated with loading propellants and pressurant gases. Receives instructions from the Test Conductor during operation of the test procedures.

Purdue University Rocket Propulsion and Power Laboratory Printed 7/9/2014 Page 1 of 9

DSO	Data System Operator: Responsible for the installation and operability of all instrumentation and controls consistent with the requirements for each test. Operates the computer control and data acquisition system during tests.
SAF	Site Safety: Responsible for insuring all test site safety equipment is in place and functioning properly. Is responsible for keeping the site clear of unauthorized personnel during test operations.

Motor Operations

At least two people need to be present to conduct motor operation. If only two are present, one person may act as both the TC and DSO while the other person may act as both TOP and SAF.

Coordinate with those performing experiments in ZL6 to ensure people are not using that building during motor operation.

Step No.	Action By	Operation	Test Run					
			A	B	C	D	E	F
		SECTION 1: PRE-TEST CHECKLIST						
1.000	SAF	Verify access to the safety shower and flush until clean water flows from shower						
1.001	SAF	Verify CO_2 fire extinguisher is in place in test cell hall way						
1.002	SAF	Verify garden hose w/spray nozzle is in place in t-cell and pressurized with water						
1.003	TC	Verify all test plans are present and complete						
1.004	TC	Verify the test article is installed per the test plan and the appropriate drawings						
1.005	DSO	Verify instrumentation and controls are patched per test plan						
1.006	DSO	Start control room computer						
1.007	DSO	Turn on SCXI chassis						
1.008	DSO	Open Labview VI control panel						
1.009	DSO	Start control panel						
1.010	DSO	Verify data file location and file name is set correctly						
1.011	DSO	Verify test sequence is set correctly						
1.012	DSO	Set file to begin data reading						
1.013	DSO	Turn on instrumentation power and valve power						
1.014	DSO	Verify correct test sequence is loaded						
1.015	DSO	Verify all data channels are reading properly						
1.016	DSO	Verify ER3000 set pressure is set to 0 psia						
1.017	DSO	Take zero data						
1.018	DSO	Turn off instrumentation power and valve power						
1.019	DSO	Restart VI and Load Test File Name						
1.020	DSO	Turn on instrumentation power and valve power						
1.021	TOP	Verify cameras and visual instrumentation are in position and functioning properly						
		Place all manually controlled valves and regulators in the proper pre-test positions						
1.022	TOP	UNLOAD Water tank ullage pressure regulator MR-N2-03						
1.023	TOP	UNLOAD Motor purge pressure regulator MR-N2-02						
1.024	TOP	UNLOAD Pneumatic valve actuation supply pressure regulator MR-N2-03						

1.025	TOP	OPEN System nitrogen supply pressure manual valve MV-N2-01 to pressurize the system to 500 psi and then close valve						
1.026	TOP	LOAD water tank supply pressure regulator MR-N2-03 to 100 psig						
1.027	TOP	LOAD Pneumatic valve actuation supply pressure regulator MR-N2-01 to 100 psig						
1.028	DSO	OPEN pressurization valve PV-WFNA-01						
1.029	TOP	OPEN System nitrogen supply pressure manual valve MV-N2-01						
1.030	TOP	Verify the nitrogen supply pressure is at least 2500 psi						
1.031	TOP	Ensure pneumatic valve actuation supply pressure regulator MR-N2-01 is set to 100 psig						
1.032	TOP	Verify oxidizer vacuum isolation valve MV-WFNA-01 is CLOSED						
1.033	TOP	Verify oxidizer fill valve MV-WFNA-02 is CLOSED						
1.034	TOP	Verify nitrogen isolation valve MV-N2-02 is OPEN						
		Verify the remote controlled valves function properly						
1.035	TOP/DSO	CYCLE Water tank pressurization valve PV-N2-01						
1.036	TOP/DSO	CYCLE WFNA pressurisation valve PV-WFNA-01						
1.037	TOP/DSO	CYCLE WFNA main valve PV-WFNA-04						
1.038	TOP/DSO	CYCLE WFNA vent valve PV-WFNA-02						
		NOTE: Valve operability is checked by listening for the valve to cycle or by visually checking						
		Verify all remote controlled valves are in their power off position						
1.039	TOP/DSO	Verify Water tank pressurization valve (NC) PV-N2-01 **CLOSED**						
1.040	TOP/DSO	Verify WFNA pressurisation valve PV-WFNA-01 **OPEN**						
1.041	TOP/DSO	Verify WFNA main valve PV-WFNA-04 **CLOSED**						
1.042	TOP/DSO	Verify WFNA vent valve PV-WFNA-02 **OPENED**						
		Purge system with nitrogen to remove moisture from plumbing						
1.043	DSO	CLOSE vent valve PV-WFNA-02						
1.044	DSO	SET ER3000 pressure to 200 psig						
1.045	DSO	OPEN vent valve PV-WFNA-02						
1.046	DSO	Allow nitrogen to flow out exhaust vent for 1 minute to purge system						
1.047	DSO	SET ER3000 pressure to 0 psig						
		SECTION 2. Fuel Grain Loading						
		NOTE: Personnel entering test cell should wear PPE appropriate for handling fuel including safety glasses and nitirile gloves						
2.000	TOP	Open t-cell garge door						
2.001	TOP	Clear t-cell of all personell and close t-cell hallway door						
2.002	DSO	Turn on outside and inside warning lights						
2.003	DSO	Verify the auto-sequence is disarmed						

2.004	TOP	Verify the nozzle and venturi match the current test plan						
2.005	TOP	Ensure proper o-ring is installed on graphite nozzle						
2.006	TOP	Sand fuel grain port with 100 grit sand paper in fume hood						
2.007	TOP	Weigh fuel grain/phenolic and measure I.D. of fuel grain center port						
2.008	TOP	Add RTV silicone to aft end lip of phenolic and to forward end of graphite nozzle lip						
2.009	TOP	Insert nozzle lip into phenolic lip and clean excess RTV						
2.010	TOP	Verify nozzle retainer plate seal o-rings are in place and coated with vacuum grease						
2.011	TOP	Insert nozzle/fuel grain assembly into motor chamber						
2.012	TOP	Attach nozzle retainer plate to motor chamber using grade 5 bolts and grade 8 nuts, torque bolts to 96 in-lbf						
2.013	TOP	Move aft motor mount over the end of the nozzle retainer plate bolts and tighten motor mount bolts						
2.014	TOP	Position rocket motor exhaust guide pipe at exit of rocket motor						
2.015	TOP	Place water sheet generator (if in use) at exit of rocket motor exhaust guide pipe						
		SECTION 3: OXIDIZER LOADING						
		NOTE: Personnel entering test cell should wear appropriate PPE including safety glasses, nitrile gloves, and face shield						
3.000	TOP	Attach stainless steel oxidizer fill line downstream of the manual oxidizer fill valve (MV-WFNA-02) (if this is the first test of the day)						
3.001	TOP	Ensure a water hose with a spray nozzle is connected to a water spicket, pressurized, and ready to use in case of an oxidizer spill						
3.002	TOP	Place 5 gallon bucket with water next to test stand						
3.003	DSO	OPEN door in t-cell control to outside of building						
3.004	TOP	Place large industrial fan inside t-cell and turn on to induce flow from front of building out through test cell garage door						
		Pulling Vacuum on Oxidizer Line System						
3.005	DSO	Ensure the manual oxidizer fill valve (MV-WFNA-02) and manual oxidizer vacuum valve (MV-WFNA-01) are closed						
3.006	DSO	CLOSE WFNA vent valve PV-WFNA-02						
3.007	DSO	CLOSE nitrogen iso valve MV-N2-02						
3.008	DSO	OPEN right side of solid motor stand exhaust doors and prop open to allow vacuum exhaust to exit building. Place an object outside the left side door to ensure it stays closed.						
3.009	DSO	LOAD Motor purge pressure regulator MR-N2-02 to 300 psi						
3.010	DSO	Ensure pressure drops appropriately by monitoring vacuum pressure gauge (PG-04)						
3.011	DSO	OPEN vacuum valve MV-WFNA-02						
3.012	DSO	Monitor pressure on pressure gauges PG-04 and PT-WFNA-08 until pressure drops below 5 psia						
3.013	DSO	CLOSE vacuum valve MV-WFNA-02						
3.014	DSO	UNLOAD Motor purge pressure regulator MR-N2-02						
3.015	DSO	CLOSE right side of solid motor stand exhaust doors						

		Oxidizer Handling/Loading						
		NOTE: Personnel entering test cell should wear appropriate PPE including safety glasses, nitrile gloves, Tyvek coveralls, large overboots, face shield, over gloves, and arm protectors						
3.016	TOP	Prop open door from t-cell hallway to outside ZL4 at the rear of the building						
3.017	TOP	Exit the building and ensure no personnel are performing any work outside near the south side of ZL-4 or north east side of ZL-1						
3.018	TOP	Place warning signs outside behind burm and next to t-cell						
3.019	TOP	Don proper PPE for handling of nitric acid including Tyvek suit, appropriate large over boots, nitrile gloves, safety glasses, face shield, chemical resistant over gloves, and arm protectors						
		NOTE: Bottles being opened for the first time may be pressurized. If bottle is a new bottle, place barrier between operator and bottle and open in large fume hood in gel lab						
3.020	TOP	Go to the Gel Lab to obtain the oxidizer						
3.021	TOP	Place beaker appropriate for the amount of oxidizer needed, transfer bottle, and ziploc bag in appropriate fume hood						
3.022	DSO	Obtain oxidizer bottle from oxidizer fume hood and place in fume hood with other supplies						
3.023	DSO	If it is suspected that the oxidizer bottle is pressurized, place in/behind container/barrier to ensure oxidizer does not spray onto operator when opening						
3.024	TOP	Slowly open the oxidizer bottle lid and measure out the amount of oxidizer needed into beaker (If this is the first test of the day, add 17 ml extra of oxidizer to account for the oxidizer left in the fill line)						
3.025	TOP	Replace lid on oxidizer bottle						
3.026	TOP	Pour oxidizer from beaker into transfer bottle						
3.027	DSO	Clean up any spilled oxidizer with a kimwipe and put in apporpriate water source						
3.028	DSO	Return oxidizer bottle to oxidizer fume hood for storage						
3.029	TOP	Place transfer bottle in ziploc bag						
3.030	TOP	Take oxidizer to t-cell by exiting t-cell hallway to outside and entering t-cell through garge door						
3.031	DSO	Monitor system pressure from t-cell control						
3.032	DSO	Ensure vacuum pressure in system is remaining constant, otherwise DO NOT LOAD OXDIZER						
3.033	TOP	Open secondary transfer container and oxidizer bottle and insert fill line into oxidizer bottle to the bottom						
3.034	TOP	Open oxidizer fill valve (MV-WFNA-02) slowly allowing all oxidizer to be filled into system ensuring that the fill line does not pass the surface of the liquid oxidizer until all is loaded						
3.035	TOP	Allow the system to draw up some air into the oxidizer fill line slowly to ensure no oxidizer has been left in fill line while ensuring that the system retains some vacuum pressure						
3.036	TOP	Close oxidizer fill valve MV-WFNA-02						
3.037	TOP/DSO	Repeat steps 3.006 to 3.024 if more oxidizer needs to be loaded						

3.038	TOP	Wipe down outside of oxidizer fill line with kimwipe to remove any oxidizer and place kimwipe in 5 gallon bucket with water						
3.039	TOP	Place oxidizer transfer bottle in 5 gallon bucket with water						
3.040	DSO	OPEN oxidizer vent valve PV-WFNA-02						
3.041	TOP	Check for leaks and/or for smoke coming from the motor chamber. If either are occuring, make a note and continue with test procedures. Inform appropriate Professors and Scott Meyer after test is complete.						
3.042	TOP	Rinse gloves in 5 gallon bucket of water						
3.043	TOP	OPEN nitrogen iso valve MV-N2-02						
3.044	TOP	Attach shop air line to exhaust guide pipe injector connector and open shop air valve MV-AIR-01						
3.045	TOP	Close door from t-cell hallway to outside of rear of building						
3.046	TOP	Turn on water to water sheet generator (if in use)						
3.047	TOP	Start manual video cameras recording, exit t-cell, close t-cell door and place safety chain in t-cell hall way						
3.048	TOP	Oxidizer loading PPE may be removed						
		SECTION 4: ENGINE TEST FIRING						
4.000	DSO	Verify camera settings/operating properly (if in use)						
4.001	TOP	Ensure no one is in the blast room and place safety chain in front of blast room door						
4.002	TOP	Close the door that separates the t-cell and t-cell control area from the rest of ZL-4						
4.003	DSO	Verify correct auto sequence is loaded						
4.004	TOP	Ready the phantom cameras by pressing capture (if in use)						
4.005	DSO	CLOSE vent valve PV-WFNA-02						
4.006	TOP	Exit the building and make certain the test area is clear						
4.007	DSO	START acquiring data						
4.008	DSO	Sound warning siren						
4.009	DSO	SET ER3000 set pressure on control panel to desired test condition						
4.010	DSO	Verify venturi inlet pressure corresponds to desired test condition via PT-WFNA-08						
4.011	DSO	ARM the auto sequence						
4.012	DSO	START Auto sequence						
4.013	DSO	DISARM the auto sequence						
		Note: In the event of an EXPLOSION or FAILURE of the test article, IMMEDIATELY CLICK THE ABORT BUTTON on the VI control panel, this will place all valves in their "end of test" state, if VI does not respond, TURN OFF VALVE POWER SUPPLY this will place all valves in their "normal" states. Purge the test article for FIVE minutes and contact Scott Meyer or a Professor before continuing.						
4.014	DSO	Set ER3000 to purge pressure value						
4.015	DSO	TURN OFF Siren						

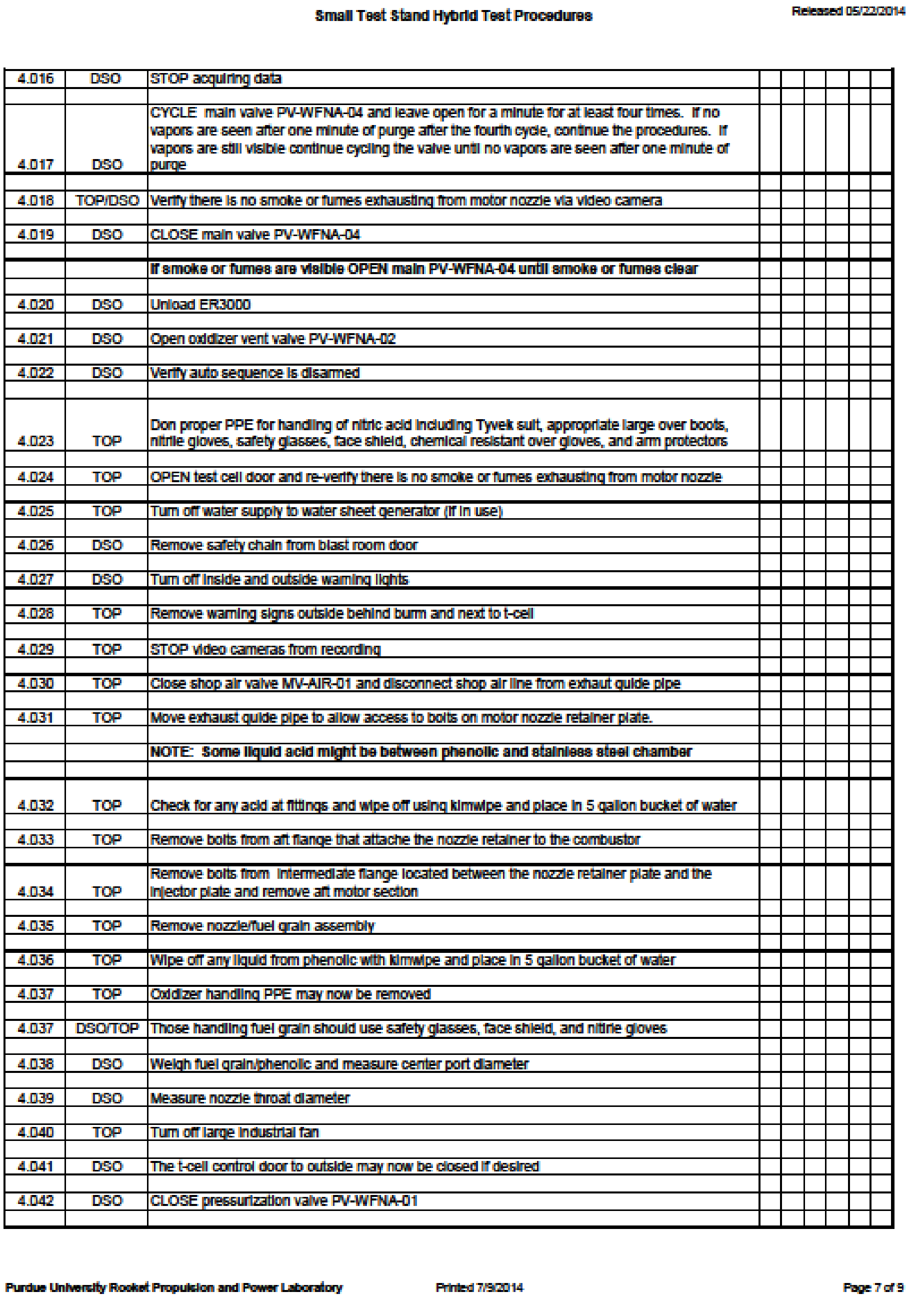

4.016	DSO	STOP acquiring data						
4.017	DSO	CYCLE main valve PV-WFNA-04 and leave open for a minute for at least four times. If no vapors are seen after one minute of purge after the fourth cycle, continue the procedures. If vapors are still visible continue cycling the valve until no vapors are seen after one minute of purge						
4.018	TOP/DSO	Verify there is no smoke or fumes exhausting from motor nozzle via video camera						
4.019	DSO	CLOSE main valve PV-WFNA-04						
		If smoke or fumes are visible OPEN main PV-WFNA-04 until smoke or fumes clear						
4.020	DSO	Unload ER3000						
4.021	DSO	Open oxidizer vent valve PV-WFNA-02						
4.022	DSO	Verify auto sequence is disarmed						
4.023	TOP	Don proper PPE for handling of nitric acid including Tyvek suit, appropriate large over boots, nitrile gloves, safety glasses, face shield, chemical resistant over gloves, and arm protectors						
4.024	TOP	OPEN test cell door and re-verify there is no smoke or fumes exhausting from motor nozzle						
4.025	TOP	Turn off water supply to water sheet generator (if in use)						
4.026	DSO	Remove safety chain from blast room door						
4.027	DSO	Turn off inside and outside warning lights						
4.028	TOP	Remove warning signs outside behind burm and next to t-cell						
4.029	TOP	STOP video cameras from recording						
4.030	TOP	Close shop air valve MV-AIR-01 and disconnect shop air line from exhaut guide pipe						
4.031	TOP	Move exhaust guide pipe to allow access to bolts on motor nozzle retainer plate.						
		NOTE: Some liquid acid might be between phenolic and stainless steel chamber						
4.032	TOP	Check for any acid at fittings and wipe off using kimwipe and place in 5 gallon bucket of water						
4.033	TOP	Remove bolts from aft flange that attache the nozzle retainer to the combustor						
4.034	TOP	Remove bolts from intermediate flange located between the nozzle retainer plate and the injector plate and remove aft motor section						
4.035	TOP	Remove nozzle/fuel grain assembly						
4.036	TOP	Wipe off any liquid from phenolic with kimwipe and place in 5 gallon bucket of water						
4.037	TOP	Oxidizer handling PPE may now be removed						
4.037	DSO/TOP	Those handling fuel grain should use safety glasses, face shield, and nitrile gloves						
4.038	DSO	Weigh fuel grain/phenolic and measure center port diameter						
4.039	DSO	Measure nozzle throat diameter						
4.040	TOP	Turn off large industrial fan						
4.041	DSO	The t-cell control door to outside may now be closed if desired						
4.042	DSO	CLOSE pressurization valve PV-WFNA-01						

4.043	DSO	Ensure valves are in de-energized state						
4.044	DSO	Turn off instrumentation power and valve power						
4.045	DSO	Stop the VI and restart for next test (or stand safing)						
4.046	DSO	Turn on instrumentation power and valve power						
4.047	DSO	OPEN pressurization valve PV-WFNA-01						
		If more tests are to be conducted return to SECTION: 2, if test series are completed proceed to SECTION: 5						
		SECTION 5: TEST COMPLETION AND STAND SAFING						
5.000	TOP	Don appropriate PPE to handle oxidizer including safety glasses, nitrile gloves, Tyvek coveralls, large overboots, face shield, over gloves, and arm protectors						
5.001	TOP	Turn on large industrial fan						
5.002	DSO	Ensure vent valve PV-WFNA-02 is open						
5.003	TOP	Remove short fill tube from oxidizer fill valve MV-WFNA-02 and place in 5 gallon bucket						
5.004	TOP	Add long 1/4" stainless steel dump tube to oxidizer fill valve MV-WFNA-02						
5.005	TOP	Place 5 gallon bucket with water at end of oxidizer fill line and OPEN oxidizer fill valve MV-WFNA-02 and let trapped oxidizer drain						
5.006	TOP	CLOSE oxidizer fill valve MV-WFNA-02						
5.007	DSO	CLOSE vent valve PV-WFNA-02						
5.008	DSO	Set ER3000 pressure to 30 psi						
5.009	TOP	Slowly OPEN oxidizer fill valve MV-WFNA-02 and let fill line purge until no oxidizer is draining from the system						
5.010	TOP	CLOSE oxidizer fill valve MV-WFNA-02						
5.011	DSO	Set ER3000 pressure to 0 psi						
5.012	TOP	Slowly OPEN oxidizer fill valve MV-WFNA-02 and let fill line purge until no gas is exiting from the system						
5.013	TOP	CLOSE oxidizer fill valve MV-WFNA-02						
5.014	DSO	Set ER3000 pressure to 30 psi and wait till pressure rises in system						
5.015	DSO	Set ER3000 pressure to 0 psi						
5.016	TOP	Slowly OPEN oxidizer fill valve MV-WFNA-02 and let fill line purge until no gas is exiting from the system						
5.017	TOP	CLOSE oxidizer fill valve MV-WFNA-02						
5.018	DSO	OPEN vent valve PV-WFNA-02						
5.019	TOP	Remove oxidizer fill line and place in 5 gallon bucket						
5.020	TOP	Wipe the end of the oxidizer fill valve MV-WFNA-02 with a kim wipe and place kim wipe in 5 gallon bucket						
5.021	TOP	Replace oxidizer fill line cap						
5.022	TOP	Remove oxidizer handling PPE						

5.023	TOP/TC	Replace nozzle retainer plate on motor and tighten bolts						
5.024	TOP/TC	Place clear blue tape over nozzle retainer plate exit						
5.025	TOP/TC	CLOSE nitrogen supply valve MV-N2-01						
5.026	DSO	OPEN water tank pressurization viave PV-N2-01 to vent supply nitrogen pressure						
5.027	DSO	Verify nitrogen supply pressure is atmospheric (PT-N2-01)						
5.028	DSO	CLOSE Water tank pressurization valve PV-N2-01						
5.029	DSO	CLOSE pressurization valve PV-WFNA-01						
5.030	TOP	UNLOAD Water tank pressurization manual regulator MR-N2-03						
5.031	TOP	UNLOAD Pneumatic valve actuation supply pressure regulator MR-N2-01						
5.032	TOP	UNLOAD Motor purge manual regulator MR-N2-02						
5.033	TC	Announce the test cell is safe and open to all personnel						
5.034	DSO	Turn off valve and instrumentation power						
5.035	DSO	Stop Labview control panel program						
5.036	DSO	Turn off SCXI chassis						
5.037	DSO	Turn off cameras and TV						
		SECTION 6: EMERGENCY PROCEDURES						
	IN CASE OF FIRE:							
6.001		CALL fire department at 9-1-1						
	IN CASE OF SEVERE INJURY:							
6.002		DIAL 9-1-1 if ambulance treatment is necessary,						
6.003		MOVE injured party if danger immanent						
6.004		SECURE test cell area, if possible.						
6.005		If test cell cannot be secured, monitor until appropriate safety personnel are present						
6.006		Contact Scott Meyer and any appropriate Professors						
		MEDICAL CARE INFORMATION						
		Purdue University Student Health Center						
		Phone: 765-494-1724						
		Location: Corner of University St. and Stadium Ave. (near ARMS/CIVIL/WTHR)						
		Hours: M-F 0800-2000 / Sa-Su 1000-1800 / Summer 0800-1700 M-F						
		Clarian Arnett Hospital						
		Phone: 765-448-8000						
		Location: 5164 McCarty Lane, Lafayette, IN 47905						

Appendix D Liquid Oxidizer Transport

Another potential pressure dependent heat source is the interaction of oxidizer reacting hypergolically with the solid fuel. In order for this to occur, liquid/gaseous oxidizer needs to be present at the surface after passing through a hot flame environment. As there was no method to visually verify if oxidizer was present at the surface, a simplified 1-D model was implemented to determine how long it would take a droplet to travel the length of the fuel grain, t_x, assuming a constant velocity according to,

$$t_x = \frac{x_{grain}}{U_{drop}} \tag{7.1}$$

where U_{drop} is the liquid oxidizer injection velocity and x_{grain} is the length of the fuel grain. Similarly, the time for a droplet of liquid oxidizer with an initial diameter of $D_{0,drop}$ to evaporate can be calculated according to,

$$t_{evap} = \frac{D_{0,drop}^2}{K} \tag{7.2}$$

where K is the evaporation constant. The K was calculated following the method outlined by Lefebvre [101] where the surface temperature of the droplet, $T_{s,drop}$, is modified until the mass transfer number, B_m, is equal to the heat transfer or Spalding number, B_T, resulting in,

$$K = \frac{8k_g ln(1+B)}{c_{p,g}\rho_{liq}} \tag{7.3}$$

where k_g and $c_{p,g}$ are the thermal conductivity and specific heat respectively of the gases immediately surrounding the droplet, $B = B_T = B_m$ when $B_T = B_m$, and ρ_{liq} is the density of the liquid droplet at $T_{s,drop}$. Both liquid oxidizer vapor pressure and latent heat of vaporization, needed to calculate B_T and B_m, were provided by Wright [84].

Both k_g and $c_{p,g}$ are composites of the thermal conductivities and specific heats of the combustion products and gaseous oxidizer at a reference temperature,

$$T_r = T_{s,drop} + \frac{T_\infty - T_{s,drop}}{3} \tag{7.4}$$

where T_∞ is the temperature of the environment in which the droplet is evaporating. According to thermal equilibrium calculations of the propellant combination, the main combustion products are H_2O, CO_2, and N_2 while nitric acid decomposes into mainly NO_2 with lesser amounts of H_2O and O_2 [102]. To determine k_g, the thermal conductivity of H_2O is used to represent that of the combustion products as H_2O has a higher thermal conductivity than the other combustion products providing a higher evaporation rate and thus an upper limit [103]. The same methodology is used for the decomposition products of nitric acid with the thermal conductivity of NO_2 representing the overall decomposition makeup [103]. The $c_{p,g}$ is determined using the specific heat of the products calculated via thermo equilibrium calculations in Cheetah 6.0 and the specific heat of NO_2 as reported by Afeefy et al. [7].

The result of the above calculations provides a value for K at ambient pressure, a condition not met in the present experiments. The various properties of the oxidizer and combustion products will vary with pressure and are not readily available in open literature making calculations of K at elevated pressure difficult. Calculations performed by Lefebvre, see

Figure D.1, indicate that K of various fuels, at pressures similar to those observed in the combustor tests, can increase by 50% above values found at ambient pressure for T_∞ up to 1500 K. Thus, a 50% increase to the value found at ambient pressure is added to determine the actual K used in the calculations.

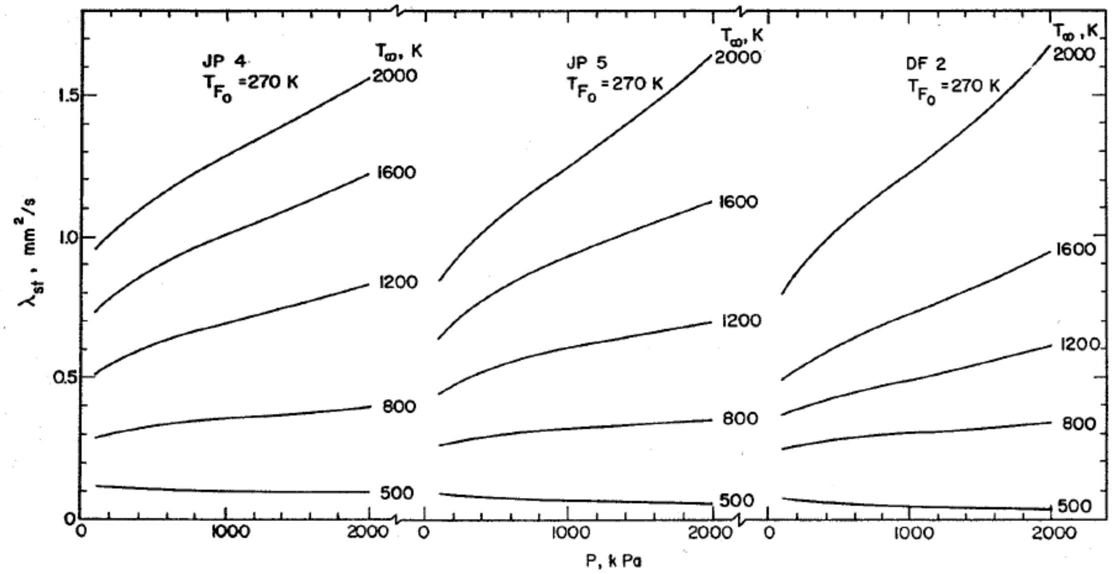

Figure D.1 The K (λ_{st}) for gasoline (JP 4), kerosene (JP 5), and diesel oil (DF 2), as a function of pressure and T_∞ [101].

Temperatures throughout the combustor vary widely from 300 k at the head end upon injection up to 3000 K in the thin flame zone. Sankaran computationally predicted thermal contours within a gaseous oxygen/HTPB motor that had a similar fuel port diameter (0.66 in) as the present experiments but had a higher oxidizer flux level (0.8 lb/in^{2}s), higher chamber pressure (900 psia) and longer fuel grain length (23 in) [104], see Figure D.2. The operating conditions of these computations result in an O/F of 1.48 that produces an equilibrium chamber temperature of 3071 K according to calculations performed in Cheetah 6.0 [72]. The operating conditions in the hypergolic hybrid tests vary from an O/F of 2.8-16.2 with equilibrium chamber temperatures of 1397-3124 K, temperatures equal to notably lower than that encountered in the computational efforts of Sankaran suggesting the temperature contours in the hypergolic motors could be similar or cooler than that predicted in Figure D.2. This information along with the hypergolic hybrid fuel grains having a length of ¼-½ of that used in Sankaran's computations indicates that the liquid oxidizer droplets will traverse most of the motor in a cool region under 500 K encountering high temperature regions for a comparatively short period of time before reaching the fuel surface. Thus, average T_∞ values of 500 and 1000 K will be used to represent the environment in which the liquid oxidizer drops are evaporating providing K values of 0.0724 and 0.3445 mm^2/s respectively. These values are similar to those found by Lefebvre for kerosene at similar temperatures and pressures, see Figure D.1, suggesting the calculations are reasonable.

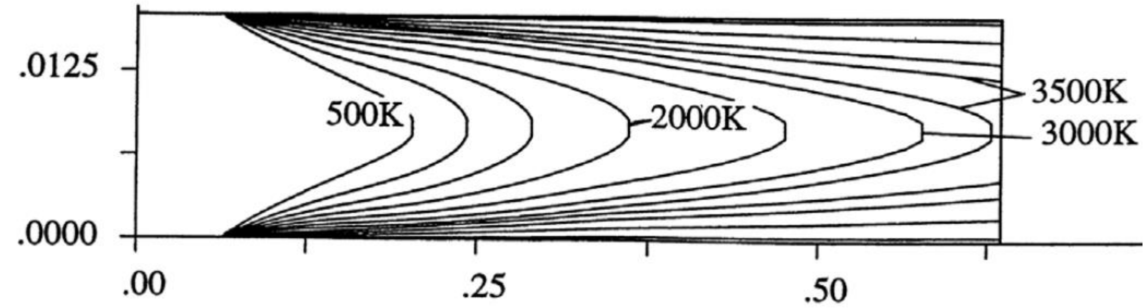

Figure D.2 Thermal contours down the fuel port of a cylindrical HTPB fuel grain combusting with gaseous oxygen [104].

The U_{drop} can be determined from the equation provided by Lefebvre,

$$U_{drop} = K_v\left(2\Delta p_{inj}/\rho_{liq}\right)^{0.5} \tag{7.5}$$

where K_v is the velocity coefficient and Δp_{inj} is the pressure drop across the injector. The initial oxidizer droplet size can be inferred by the geometry of the injector. According to

Lefebvre, K_v for a pressure fed swirl injector is a function of Δp_{inj} and d_0 (the injector final orifice diameter) [101], see Figure D.3. The lowest and highest values for U_{drop} associated with the operating conditions seen in the combustor along with the calculated time it will take an oxidizer droplet to travel the length of the fuel grain assuming a constant velocity are provided in Table D.1.

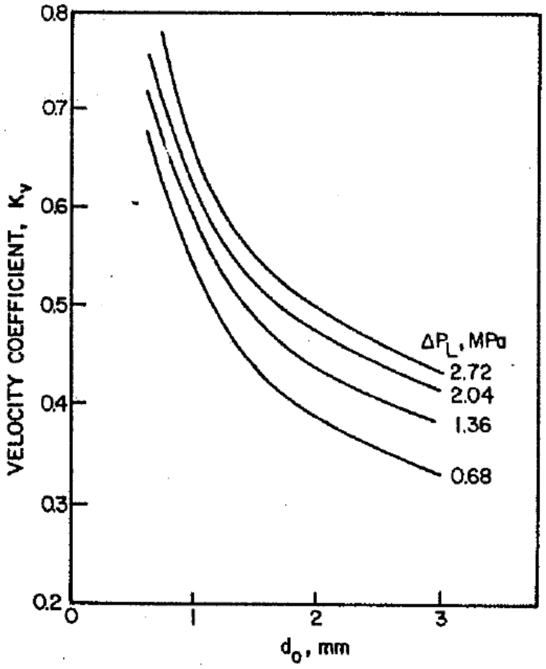

Figure D.3 Velocity coefficient as a function of Δp_{inj} and d_0 [101].

Table D.1 Droplet injection velocities for operating conditions and injectors used during combustor operation and the resulting time for a droplet to travel the length of the 0.30 m (12 in) long fuel grains.

Δp_{inj}, MPa	d_0, mm	K_v	U_{drop}, m/s	t_x, ms
0.2068	0.79	0.6	10.03	30.4
0.7584	1.22	0.5	16.01	19.0

The final parameter needed to complete the calculations is $D_{0,drop}$. According to Lefebvre, pressure fed swirl injectors that have similar dimensions to the injectors used in the current study can have a measurable amount of droplets with diameters of 0-140 μm [101], see Figure D.4. The majority of the volume of liquid droplets from these experiments have a diameter around 30 μm with a lesser volume for droplet diameters around 100 μm. Both of these droplet diameters will be used in the calculations to provide a representation of the entire spray.

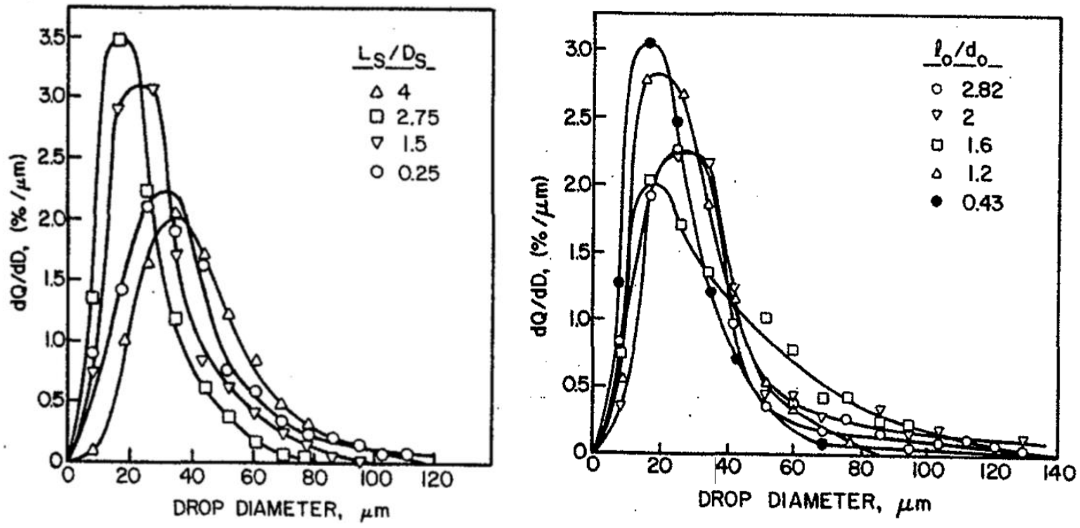

(a) (b)

Figure D.4 Droplet size distributions for pressure fed swirl injectors as a function of (a) swirl chamber length, L_s, /swirl chamber diameter, D_s, and (b) injector orifice length, l_0, /injector orifice diameter, d_0, [101].

Results of the calculations described in this section are provided in Table D.2. According to these results and those provided in Table D.1, the larger 100 μm droplets will reach the end of the short and long fuel grains for all operating conditions while the smaller 30 μm droplets will reach the end of the short grain for all U_{drop} and the end of the long grain for the injector that has a higher U_{drop} if T_∞ is 500 K. These calculations are based on steady state evaporation and ignore the transient effects of heating the droplet from its initial temperature to $T_{s,drop}$. Lefebvre indicated that the time needed for transient heating of the droplet can be almost just as long as the steady state portion causing t_{evap} in Table D.2 to double [101]. It is thus likely that liquid oxidizer is present on the fuel surface over the entire grain length making hypergolic exothermic reactions possible during combustion.

Table D.2 Evaporation rates and times for nitric acid droplets for several droplet sizes and average combustor temperatures.

T_∞, K	K, mm^2/s	$D_{0,drop}$, μm	t_{evap}, ms
500	0.0724	30	18.7
1000	0.3445	30	3.9
500	0.0724	100	207.3
1000	0.3445	100	43.5

VITA

VITA

Mark A. Pfeil

Education

Bachelor of Science in Aeronautical and Astronautical Engineering Dec 2008
GPA: 3.78/4.00, Purdue University
Master of Science in Aeronautical and Astronautical Engineering May 2012
GPA: 3.78/4.00, Purdue University
Doctor of Philosophy in Aeronautical and Astronautical Engineering Dec 2014
GPA: 3.81/4.00, Purdue University

Related Professional Experience

SMART Fellow: Zucrow Labs/Redstone Aresenal Aug 2011 – Dec 2014
Combustion Studies of **Hypergolic Hybrid Rockets** using **Amine-boranes** and Other Additives

Research Assistant: Zucrow Labs Jan 2009 – Jul 2011
Research Effect of **Fuel Additives** on **Combustion Instability/Behavior** in **Liquid Rocket Motor**
Liquid Rocket System Design, Assembly, and Testing
Fundamental **Droplet Combustion** Experiments
Mixing, Casting, Testing and Successful Flight of Experimental **Solid Rocket Propellant–ALICE**

Senior Design Project Aug - Dec 2008
Designed Integrated Propulsion Concept for Supersonic Jet

Pacific Northwest National Laboratory Richland, WA
Modeled Coal Gasification Reactions May – July 2008
Tested Radioactive Material Detection Systems

Air Force Research Lab Edwards AFB, CA
Shadowed Personnel in Solid Rocket Motor Branch May – July 2006

Experience Using: White Fuming Nitric Acid, Red Fuming Nitric Acid, High Concentration Hydrogen Peroxide, Amine-boranes, and Various Other Fuels

Experience With: Matlab, Simulink, Cosilab, Cheetah, NASA Thermochemistry Code - CEA, GASEQ, Air Force ISP, SolidWorks, Pro E, C, Microsoft Office, AutoCAD, Virtual Engineer, FEM Builder

Proposals

(submitted) Pfeil, M. A., Son, S. F., Heister, S. D., Lucht, R. P., and Ramachandran, P. V., "Surface Chemistry and Combustion Behavior of Hypergolic Solid Fuels," Army Research Laboratory BAA, 2014.

Other

Undergraduate Teaching Assistant — West Lafayette, IN
Recitation of General Physics — Jan – Apr 2006

Church Mission Trip to Ecuador — Nov 2002 - Nov 2004

Assistant Project Manager — Glendale Heights, IL
Voris Mechanical, Inc. — May – Sep 2002
Estimated Construction Costs
Purchased Equipment/Supplies for Projects

Eagle Scout — 2001

PUBLICATIONS

PUBLICATIONS

Journal Articles

(writing) Pfeil, M. A., Son, S. F., and Heister, S. D., “Hypergolic Hybrid Rocket Combustion Behavior of a Ethylenediamine Bisborane/Ferrocene/Epoxy Fuel,” 2015.

(submitted) Pfeil, M. A., Kulkarni, A. S., Ramachandran, P. V., Son, S. F., and Heister, S. D., “Solid Amine-boranes as High Performance and Hypergolic Hybrid Rocket Fuels,” *Journal of Propulsion and Power*, 2014.

(accepted) Ramachandran, P. V., Kulkarni, A. S., Pfeil, M. A., Dennis, J. D., Willits, J. D., Heister, S. D., Son, S. F., and Pourpoint, T. L., “Amine-Boranes: Green Hypergolic Fuels with Extremely Low Ignition Delays,” *Chemistry - A European Journal*, 2014.

(accepted) Pfeil, M. A., Dennis, J. D., Son, S. F., Heister, S. D., Pourpoint, T. L., and Ramachandran, P. V., “Characterization of Ethylenediamine Bisborane as a Hypergolic Hybrid Rocket Fuel Additive,” *Journal of Propulsion and Power*, 2014.

Pfeil, M. A., Son, S. F., and Anderson, W. E., “The Influence of the Addition of Ammonia Borane on the Combustion Stability of a Liquid Rocket Combustor,” *Journal of Propulsion and Power*, 2014.

Pfeil, M. A., Groven, L. J., Lucht, R. P., and Son, S. F., “Effects of Ammonia Borane on the Combustion of an Ethanol Droplet at Atmospheric Pressure,” *Combustion and Flame*, Vol. 160, 2013, pp. 2194-2203.

Pourpoint, T. L., Wood, T. D., Pfeil, M. A., Tsohas, J., and Son, S. F., “Feasibility Study and Demonstration of an Aluminum and Ice Solid Propellant,” *International Journal of Aerospace Engineering*, vol. 2012, 2012.

McCrary, P. D., Beasley, P. A., Kelley, S. P., Schneider, S., Boatz, J. A., Hawkins, T. W., Perez, J. P. L., McMahon, B. W., Pfeil, M., Son, S. F., Anderson, S. L., and Rogers, R. D., “Tuning Azolium Azolate Ionic Liquids to Promote Surface Interactions with Titanium Nanoparticles Leading to Increased Passivation and Colloidal Stability,” *Physical Chemistry Chemical Physics*, vol. 14, pp. 13194-13198, 2012.

McCrary, P. D., Beasley, P. A., Cojocaru, O. A., Schneider, S., Hawkins, T. W., Perez, J. P. L., McMahon, B. W., Pfeil, M., Boatz, J. A., Anderson, S. L., Son, S. F., and Rogers, R. D., "Hypergolic Ionic Liquids to Mill, Suspend, and Ignite Boron Nanoparticles," *Chemical Communications*, vol. 48, pp. 4311-4313, 2012.

Conference Proceedings

Pfeil, M. A., Kulkarni, A. S., Ramachandran, P. V., Son, S. F., and Heister, S. D., "Amine Boranes as High Performance Hypergolic Additives for Hybrid Rocket Fuels," *JANNAF*, Charleston, SC, May 19-22, 2014.

Hedman, T. D., Cho, K. Y., Pfeil, M. A., Satija, A., Mongia, H. C., Groven, L. J., Son, S. F., and Lucht, R. P., "High Speed PLIF Apllied to Multiphase Combustion," *Spring Technical Meeting of the Central States Section of the Combustion Institute*, Apr 22-24, 2012.

Pfeil, M. A., Groven, L. J., Lucht, R. P., and Son, S. F., "Effects of Ammonia Borane on the Combustion of an Ethanol Droplet at Atmospheric Pressure," AIAA Paper 2011-5626, *47th AIAA/ASME/SAE/ASEE Joint Propulsion Conference and Exhibit*, San Diego, CA, Jul 31-Aug 03, 2011.

Rosen, S., Pfeil, M., Yu, Y., and Anderson, W., "Effects of Hydrogen Addition on Combustion Instability of an Unstable Methane Rocket Combustor," AIAA Paper 2011-328, *49th AIAA Aerospace Sciences Meeting including the New Horizons Forum and Aerospace Exposition*, Orlando, FL, Jan 4-7, 2011.

Pfeil, M., Rosen, S., Yu, Y., Anderson, W., and Son, S., "Effects of NanoAluminum on Droplet Combustion and Combustion Instabilities in a Single Element Rocket Combustor," AIAA Paper 2010-7154, *46th Joint Propulsion Conference and Exhibit*, Nashville, TN, Jul 25-28, 2010.

Wood, T., Pfeil, M., Pourpoint, T., Tsohas, J., and Son, S., "Feasibility Study and Demonstration of an Aluminum and Ice Solid Propellant," AIAA Paper 2009-4890, *45th Joint Propulsion Conference and Exhibit*, Denver, CO, Aug 2-5, 2009.

Risha, G., Connell, T., Yetter, R., Yang, V., Wood, T., Pfeil, M., Pourpoint, T., and Son, S., "Aluminum-Ice (ALICE) Propellants for Hydrogen Generation and Propulsion," AIAA Paper 2009-4877, *45th Joint Propulsion Conference and Exhibit*, Denver, CO, Aug 2-5, 2009.

Technical Reports

Risha, G. A., Connell, T. L., Weismiller, M., Yetter, R. A., Sundaram, D. S., Yang, V., Wood, T. D., Pfeil, M. A., Pourpoint, T. L., Tsohas, J., and Son, S. F., "Novel Energetic Materials for Space Propulsion," Air Force Office of Scientific Research, A818645, Arlington, VA, Apr. 2011.